Technical Physics Letters, Vol. 31, No. 1, 2005, pp. 1–3. Translated from Pis'ma v Zhurnal Tekhnicheskoĭ Fiziki, Vol. 31, No. 1, 2005, pp. 3–8.

Cone-Shaped Beams in Selective Laser Cladding

Yu. A. Chivel

Institute of Molecular and Atomic Physics, National Academy of Sciences of Belarus, Minsk, Belarus
e-mail: yuri-chivel@mail.ru

Received June 28, 2004

Abstract—A new method of radiation energy introduction into a powder jet for selective laser cladding (SLC) technology is presented, which is based on the unique properties of cone-shaped laser beams. The parameters of the propagation of cone-shaped laser beams in high-density thin powder jets and the heating of material particles in such jets have been calculated. The SLC process using the proposed method is characterized by a tenfold increase in the process efficiency as compared to the known technologies, by increased precision of processing, and by a higher coefficient of powder utilization. © *2005 Pleiades Publishing, Inc.*

Introduction. According to the well-known method of selective laser cladding (SLC) [1], particles of a powdered material are introduced from the side into the region of a focused laser beam spot on the surface of a processed article. At a high concentration of particles, this leads to shadowing of the surface, mutual shadowing of particles in the jet, and a very short time of particle exposure in the zone of laser-induced heating. In order to ensure the melting of particles and the formation of an article, considerable power has to be spent, with low efficiency, for the maintenance of a bath of molten material in the region of laser beam focus on the article surface. However, the presence of this bath significantly reduces the precision of SLC technology, which typically does not exceed 100 μm.

Description of method. According to the proposed method of introducing radiation energy into a powder jet [2], laser radiation energy is uniformly supplied to a cylindrical powder jet over the entire surface of this cylinder. In such a regime, laser radiation energy is effectively transferred to material particles even under the conditions of virtually absent heat conduction. The required laser beam configuration is obtained with the aid of cone-shaped optical elements [3], which ensure the formation of nondiffracted laser beams.

Figure 1 shows one possible variant of implementation of the proposed method. Laser radiation in the form of an annular beam is deflected by mirror *5* toward cone-shaped (axicone) lens *6*. Interference taking place in the region of convergence of the cone-shaped beam leads to the formation of focal region *3* with a length of $\Delta Z = \Delta R \tan\gamma$, where γ is the angle of convergence of the cone-shaped beam. The transverse distribution of intensity in this focal region for laser radiation propagating in a transparent medium is described by a zeroth-order Bessel function with the width of the central maximum $2.4\lambda/\pi\sin\gamma$ (Fig. 1). The dense jet of powdered material is introduced into focal region *3* on the surface of substrate *4* with the aid of feeding unit *2* connected to container *1*.

In the presence of a strongly absorbing and scattering medium, the transverse structure of the radiation beam exhibits a significant change. The coefficient of coherent transmission for a disperse layer of particles (coarse optical inhomogeneities (such that $\pi d/\lambda > 1$, $\pi d/\lambda(n-1) \gg 1$) can be expressed as [4]

$$T = \exp(-Q_n\eta), \qquad (1)$$

where $Q_n = 1/1.5C_3\ln[1 + 1.5C_3Q\exp(1.5C_3Q)]$ is the effective attenuation factor for a single particle (at a given particle concentration). Here, Q is the particle attenuation factor, $C_3 = 0.74(d/l)^3$ is the space filling

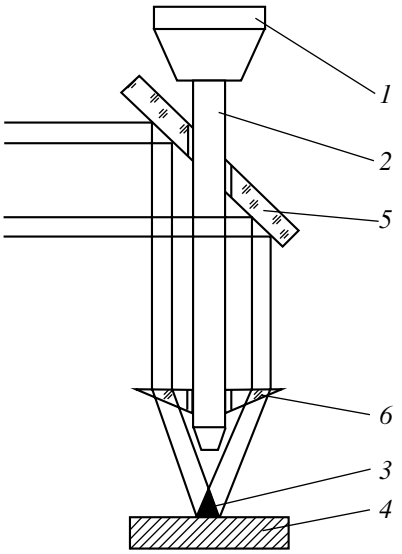

Fig. 1. Optical scheme of laser radiation energy introduction into a powder jet (see the text for explanations).

1063-7850/05/3101-0001$26.00 © 2005 Pleiades Publishing, Inc.

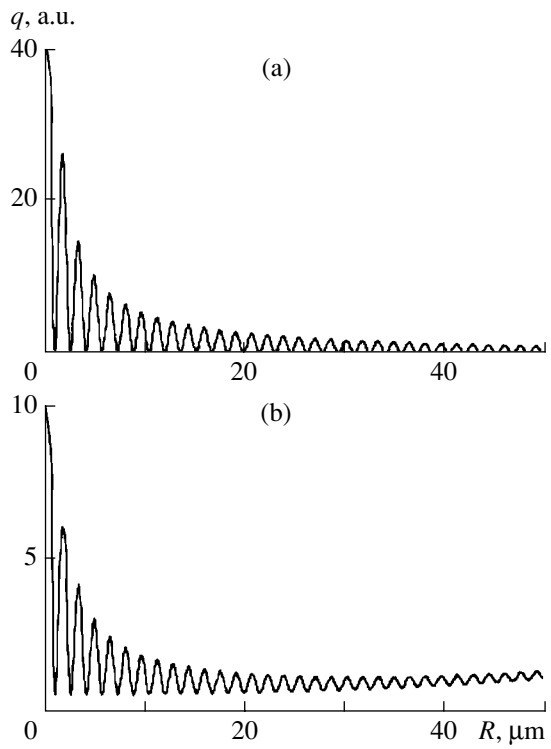

Fig. 2. Laser radiation intensity profiles in the cross section of a cone-shaped laser beam (a) in a transparent medium and (b) in a powder jet (consisting of 10-μm-diameter particles with a concentration of 10^8 cm^{-3}).

factor, and l is the average distance between particles. Relation (1) can be rewritten as

$$T = \exp[-\mu(R-r)], \quad (2)$$

where $R-r$ is the depth of radiation penetration into the powder jet and μ is the coefficient of light absorption in the powdered medium.

Being multiply scattered on the powder particles, radiation is effectively absorbed in this dense medium. The calculated attenuation coefficient is close to the value for a coherent component. The laser beam structure depends significantly on the particle concentration.

The results of numerical calculations showed that, in a jet with a diameter of 10–100 μm, consisting of spherical metal particles with a diameter of d = 1–10 μm and a particle concentration of $N = 10^{12}$–10^8 cm^{-3}, respectively, the interference structure will be suppressed everywhere except for the region of the central maximum (Fig. 2). Outside this central maximum, the laser radiation intensity is described by the expression

$$q = q_0 R/r(e^{-\mu(R-r)} + e^{-\mu(R+r)}), \quad (3)$$

where R is the powder jet radius, r is the current coordinate ($r > 0$), q_0 is the laser radiation intensity at the jet boundary, and $\mu = 0.03$ μm^{-1} (e.g., for particles with d = 10 μm and $N = 10^8$ cm^{-3}).

Model numerical calculations of the regime of laser heating in powder jets, consisting of particles with a diameter of 1 and 10 μm supplied at a velocity of 10 m/s, were performed for the above indicated range of concentrations assuming the particles to be made of titanium. The results of calculations showed that, in order to ensure heating of the particles in such microjets up to the melting temperature, it is necessary to supply laser radiation with $\lambda = 1.06$ μm at a power not exceeding 3 and 30 W for the variants of powders with a particle diameter of d = 1 and 10 μm, respectively. Heating of the substrate surface in the region of deposition is provided both by laser radiation (in the focal spot) and by the powder particles impinging on the substrate surface.

The proposed method of laser radiation energy introduction into a powder jet creates prerequisites for high-precision sintering of nanodimensional particles with the aid of a system capable of supplying the powdered material at a minimum perturbation of the particle motion. An example is offered by the heating of nanodimensional particles during their free fall in the caustic of a Bessel beam. Particles falling from a height of 10 mm impact on the article surface *4* at a velocity of 0.4 m/s and stay in the laser heating region for ~0.04 s. For this exposure time, a powder jet consisting of 10-μm-diameter titanium particles with a concentration of 10^{14} cm^{-3} will be heated to the melting temperature (~2 kK) if the radiation power at the jet boundary is on a level of $W \sim 0.64$ W.

The results of our model calculations also showed that the main negative factor hindering the heating of nanoparticles are large radiative losses related to their highly developed surface. However, the passage to nanopowders is also accompanied by the surface contribution to the free energy, so that the sintering temperature T_{NS} drops as described by the relation [5]

$$T_{NS}/T_M = \exp[-C(d_0 - d)/d], \quad (4)$$

where T_M is the sintering temperature for d_0 = 1 mm and C is a constant dependent on the material properties (for example, $C \sim 10^{-5}$ for titanium nitride). For nanoparticles with a diameter of ~10 nm, the sintering temperature is $\sim 0.3T_M$, while for $d \sim 5$ nm we have $T_{NS} \sim 0.1T_M$. In addition, a dense jet radiates similarly to a surface emitter because of radiation self-absorption.

In order to increase the efficiency of energy deposition in the jet at low particle concentrations and to reduce the radiative losses, a special optical multipass scheme has been developed based on cone-shaped and cylindrical mirrors. This scheme minimizes the radia-

tive losses and ensures the complete utilization of laser radiation, which is spent on heating the powder even at a rather low particle densities in the jet.

Conclusion. A comparison with the other known SLC processes showed that the energy consumption for sintering three-dimensional objects using the proposed method of laser radiation energy introduction into a powder jet is about 2×10^3 J/g. This provides for a tenfold higher efficiency of the SLC process as compared to that of the DLF and LENS processes, while simultaneously increasing the precision of processing and ensuring a higher coefficient of powder utilization.

REFERENCES

1. D. Thoma, G. Lewis, *et al.*, in *Proceedings of the 15th International Thermal Spray Conference, Nice, 1998,* pp. 1205–1210.
2. Yu. Chivel, Proc. SPIE **5399**, 228 (2004).
3. J. McLeod, J. Opt. Soc. Am. **44**, 592 (1954).
4. A. P. Ivanov, V. A. Loyko, and V. P. Dik, *Light Propagation in Densely Packed Dispersive Media* (Nauka i Tekhnika, Minsk, 1988) [in Russian].
5. E. I. Asinovsky and L. S. Polak, Khim. Vys. Énerg. **26**, 276 (1992).

Translated by P. Pozdeev

Technical Physics Letters, Vol. 31, No. 1, 2005, pp. 13–17. Translated from Pis'ma v Zhurnal Tekhnicheskoĭ Fiziki, Vol. 31, No. 1, 2005, pp. 24–34.

The Surface Pressure in a Faceted Nanocrystal

M. N. Magomedov

Institute for Problems of Geothermics, Dagestan Scientific Center, Russian Academy of Sciences, Makhachkala, Dagestan, Russia

e-mail: mahmag@iwt.ru

Received July 6, 2004

Abstract—An expression for the surface pressure P_{sf} in a nanocrystal with a free surface is obtained. The nanocrystal is assumed to have the shape of a parallelepiped with a square base and the number of atoms N that can vary from eight to infinity. The surface pressure depends on the nanocrystal size ($P_{sf} \sim N^{-1/3}$), and this dependence increases when the shape of the nanocrystal deviates from cubic. For any substance, there exists a certain inversion temperature T_i at which the $P_{sf}(T)$ curves for nanocrystals of various dimensions intersect. The dispersion of nanocrystals leads to a growth of the surface pressure at $T < T_i$ and to a decrease in this pressure at $T > T_i$. It is also established that, as the size of nanocrystals decreases, the surface pressure produces compression of the crystals below a certain temperature T_{e0} and stretches the crystals at higher temperatures. © *2005 Pleiades Publishing, Inc.*

The pressure caused by the presence of a free surface in bounded systems is called surface pressure (P_{sf}) or the Laplace pressure [1, 2]. It is commonly accepted that the surface pressure is determined by the surface curvature radius and is zero for a flat surface [1, 2]. Moreover, the very existence of the surface pressure has sometimes been disputed [3–7]. Arguments in favor of the "absence of the Laplace pressure" were based on the results of experiments showing that the crystal lattice parameter is independent of the number N of atoms in a nanocrystal (or even increases with decreasing N).

In order to clarify this situation, let us consider a system of N identical atoms occurring at a temperature T and a pressure P. A change in the free energy of this system dependent on the temperature, volume (V), the number of atoms, and the surface area (Σ) is described by the equation

$$dF(T, V, N, \Sigma) = -SdT - PdV + \mu dN + \sigma d\Sigma, \quad (1)$$

where S, μ, and σ are the entropy, chemical potential, and specific (per unit area) free surface energy (called surface tension in liquids), respectively.

In a bounded system, the pressure is defined by the general expression

$$\begin{aligned} P(T, V, N) &= -(d(F/N)/d(V/N))_{T, N} \\ &= P_{in} - (d(\sigma\Sigma/N)/d(V/N))_{T, N} = P_{in} - P_{sf}. \end{aligned} \quad (2)$$

The first term (P_{in}) is the internal pressure, which reflects a change in the free energy due to isothermal variation of the specific volume with neglect of the surface (i.e., for $\Sigma/V = 0$). The second term (P_{sf}) describes the pressure related to a change in the specific surface energy caused by a variation of the specific volume. In the general case, the latter term can be written as

$$P_{sf} = \sigma(d\Sigma/dV)_{T, N} + (\Sigma/N)(d\sigma/d(V/N))_{T, N}. \quad (3)$$

Here and in Eq. (2), the sign is selected so that $P_{sf} > 0$ corresponds to the compression of the crystal.

Now let us consider a nanocrystal having the shape of a rectangular parallelepiped with the total number of atoms N, of which N_{base} are accommodated on the edge of a square base and $N_{side} = fN_{base}$, on the side edge of the parallelepiped. The total number of atoms is $N = fN_{base}^3/\alpha$, where $f = N_{side}/N_{base}$ is the shape parameter, $\alpha = \pi/6k_{pack}$ is the parameter of the microstructure, and k_{pack} is the packing factor. The crystal–vacuum interface is assumed to be the Gibbs geometric surface [8].

Previously [9–11], it was demonstrated that the mean coordination number k_3 as a function of the crystal size (determined by the number of atoms N or the crystal diameter d) and shape (determined by the shape parameter f) is given by the formulas

$$\begin{aligned} k_3^*(N, f) &= \langle k_3\rangle/k_3(\infty) = 1 - Z_s(f)(\alpha^2/N)^{1/3}, \\ k_3^*(d^*, f) &= 1 - 3^{1/2}L_d(f)\alpha/d^*; \quad d^* = d/c, \end{aligned} \quad (4)$$

where c is the average distance between the centers of the nearest-neighbor atoms and $Z_s(f)$ and $L_d(f)$ are the crystal habitus functions defined as

$$\begin{aligned} Z_s(f) &= (1 + 2f)/3f^{2/3}, \\ L_d(f) &= [(2f + 1)/3f][(2 + f^2)/3]^{1/2}. \end{aligned} \quad (5)$$

1063-7850/05/3101-0013$26.00 © 2005 Pleiades Publishing, Inc.

The volume, surface area, and "diameter" (d is the distance between the most distant atoms) in the rectangular parallelepiped are expressed as

$$V = N_{\text{base}}^3 f c^3 = N\alpha c^3,$$

$$\begin{aligned}\Sigma &= 2N_{\text{base}}^2(1+2f)c^2\alpha_s = 6c^2\alpha_s(N\alpha)^{2/3}Z_s(f),\\ d &= N_{\text{base}}(2+f)^{1/2}c = 3^{1/2}c\alpha_d(N\alpha)^{1/3}Z_d(f),\end{aligned} \quad (6)$$

$$Z_d(f) = f^{-1/3}[(2+f^2)/3]^{1/2},$$

where α_s and α_d are coefficients reflecting the density of atomic packing on the side face (i.e., in the surface layer) and on the edge of the nanocrystal, respectively.

Using formulas (3) and (6), the surface pressure can be expressed as

$$P_{sf} = 2[\alpha_s Z_s(f)/V^{1/3}][2\sigma + c(d\sigma/dc)_{T,N}]. \quad (7)$$

Here, the first term describes a change in the surface area related to variations of the nanocrystal volume at σ = const. It is this contribution that is usually referred to as the Laplace pressure [1, 2]. For a spherical drop of radius r, this pressure is $P_{ls} = 2\sigma/r$ [2]. For the Laplace pressure in a crystal of arbitrary shape with an effective diameter $d = 2r$, expressions (6) and (7) yield $P_{ls} = (4\sigma/d)3^{1/2}L_d(f)\alpha$. In particular, for a cubic crystal ($f = 1$) we obtain $P_{ls} = (4\sigma/d)3^{1/2}\alpha$, which differs from the formula for the spherical drop by the coefficient dependent on the crystal structure: $3^{1/2}\alpha = 1.225$ for $k_{\text{pack}} = 0.7405$ (hexagonal close-packed lattice); 1.333 for $k_{\text{pack}} = 0.6802$ (body centered cubic lattice); 2.667 for $k_{\text{pack}} = 0.3401$ (diamond lattice). Thus, the Laplace pressure in a nanocrystal is always greater than that in a spherical drop of the same diameter, and the more "loose" the crystal structure, the greater the excess.

The second term in formula (7) reflects a change in the specific surface energy caused by isothermal variations of the density. In liquids, this contribution is usually ignored taking into account the nature of the liquid state, whereby isothermal expansion of the surface leads to a supply of additional atoms from the bulk. If the surface density remains unchanged, the second terms in expressions (3) and (7) are zero. As for solids, these terms in the expressions for the surface pressure cannot be considered vanishing [7].

Let atoms in the nanocrystal interact as described by a pair potential of the Mie–Lennard-Jones type [12, 13]:

$$\begin{aligned}\varphi(r) &= [D/(b-a)][a(r_0/r)^b - b(r_0/r)^a]\\ &= [D/(b-a)]\{a[r_0/(c+r')]^b - b[r_0/(c+r')]^a\},\end{aligned} \quad (8)$$

where D and r_0 are the depth and coordinate of the potential well minimum, respectively, and b and a are the parameters characterizing the rigidity and range of the potential, respectively.

Describing the vibrational spectrum of the nanocrystal in terms of the Einstein model and within the framework of the nearest-neighbor approximation, we obtain the following expression for the specific (per unit area) free surface energy of the nanocrystal under consideration [11]:

$$\begin{aligned}\sigma(T,V,N) &= (dF/dk_3^*)_{V,T}[(dk_3^*/df)_{\alpha,N}/(d\Sigma/df)_{\alpha,N,c}]\\ &= [k_3(\infty)D/12c^2\alpha_s]\{(bR^a - aR^b)/(b-a)\\ &\quad - 3[k_b\Theta/k_3(N)D]E_w(\Theta/T)[\Theta/\Theta + A_w\xi]\}.\end{aligned} \quad (9)$$

Here, k_b is the Boltzmann constant, Θ is the Einstein temperature, $\gamma = -(d\ln\Theta/d\ln V)_T$ is the Grüneisen parameter, $R = r_0/c$, and

$$E_w(\Theta/T) = 0.5 + [\exp(\Theta/T) - 1]^{-1}. \quad (10)$$

The characteristic Einstein temperature (we assume that Θ is independent of T) and the Grüneisen parameter can be expressed as [14, 15]

$$\begin{aligned}\Theta &= A_w\xi\{-1 + [1 + (6D/k_bA_w\xi^2)]^{1/2}\},\\ \gamma &= (b+2)\Theta/6(\Theta + A_w\xi),\end{aligned} \quad (11)$$

where m is the atomic mass, $\hbar$ is the Planck constant, $\xi = 9/k_3(\infty)$, and

$$\begin{aligned}A_w &= K_R[5k_3(N,f)ab(b+1)/192(b-a)]R^{b+2},\\ K_R &= \hbar^2/k_br_0^2m.\end{aligned} \quad (12)$$

Substituting expression (9) into Eq. (7), we obtain an equation for the reduced surface pressure,

$$\begin{aligned}\bar{P}_{sf} = P_{sf}6\alpha r_0^3/Dk_3(\infty) &= W_sR^3\{-[ab(R^a - R^b)/(b-a)]\\ &\quad + 9\gamma(N)[k_b\Theta(N)/k_3(N)D]Y_E(x,y)E_w(y)\},\end{aligned} \quad (13)$$

where $x = A_w(N)\xi/\Theta(N)$, $y = \Theta(N)/T$, and

$$\begin{aligned}W_s &= 1 - k_3^* = Z_s(f)(\alpha^2/N)^{1/3}\\ &= Z_s(f)\alpha(c/V^{1/3}) = 3^{1/2}L_d(f)\alpha/d^*,\\ Y_w(x,y) &= [1/(1+x)]\{t(y) - [x(1+2x)/(1+x)]\},\\ t(y) &= 1 - \{2y\exp(y)/[\exp(2y) - 1]\}.\end{aligned} \quad (14)$$

As can be seen from Eq. (13), the absolute value of the surface pressure increases when f differs from unity (i.e., when the shape of the nanocrystal deviates from cubic).

The first term in Eq. (13) is the "static" surface pressure, which appears because the average distance between the centers of the nearest-neighbor atoms differs from the coordinate of the minimum of potential (8) (this difference is caused by a change in the system density). The second term is the "vibrational" surface pressure related to the oscillations of atoms in the lattice sites. As can be seen from Eq. (13), the first term vanishes in the range of low pressures, where $R \cong 1$, and, therefore, the sign of the function $P_{sf}(N, f)$ is determined by the term

$$P_w = \gamma^*(\Theta^*/k_3^*)Y_w(x, y)E_w(y). \quad (15)$$

In this expression, the arguments in all the functions depend on k_3^* as described by the formulas

$$y = \Theta(N)/T = \Theta^*/T_e, \quad T_e = T/\Theta(\infty),$$

$$\Theta^* = \Theta(N, f)/\Theta(\infty) \cong (k_3^*)^{1/2}, \quad (16)$$

$$x = A_w(N)\xi/\Theta(N) \cong [A_w(\infty)\xi/\Theta(\infty)](k_3^*)^{1/2} = x_\infty(k_3^*)^{1/2},$$

$$\gamma^* = \gamma(N, f)/\gamma(\infty) \cong (1 + x_\infty)/(1 + x),$$

where the asterisk denotes (as in expressions (4)) normalization to the macroscopic analog.

Therefore, the sign of the surface pressure for $R \cong 1$ is determined by three arguments of the function $P_w(x_\infty, k_3^*, T_e)$. The quantity T_e is the relative temperature of the system (with respect to the Einstein temperature). According to Eqs. (4), the quantity k_3^* characterizes the size and shape of the nanocrystal: the smaller the crystal (or the more its shape deviates from cubic), the lower the value of k_3^*. The behavior of $k_3^*(N, f)$ has been studied in detail elsewhere [9–11], in particular, $k_3^*(N_{min} = 8, f = 1) = 0.5$. The quantity $x_\infty = A_w(\infty)\xi/\Theta(\infty)$ characterizes the quantum properties of substances in a macrocrystalline state: the smaller x_∞ is, the more "classical" the macrocrystal. This "quantization" parameter, evaluated as $x_\infty \cong [k_b A_w(\infty)\xi^2/6D]^{1/2}$, is essentially the ratio of the energy zero-point oscillations to the energy of chemical binding. This quantity can be also related to the de Buhr parameter ($\Lambda_B = \hbar/r_0(2mD)^{1/2}$) characterizing the role of the zero-point oscillations in a crystal [16]:

$$k_b A_w(\infty)\xi^2/6D = \xi^2\zeta_p\Lambda_B^2/3;$$
$$\zeta_p = A_w(\infty)/K_R \quad (17)$$
$$= [5k_3(\infty)ab(b+1)/192(b-a)]R^{b+2}.$$

At low pressures (i.e., at $R = 1$), for $b \cong 2a \gg 1$, we can readily obtain an estimate of $\xi^2\zeta_p/3 \cong 3a/k_3(\infty)$. Therefore, the quantization parameter is on the same order of magnitude as the de Buhr parameter: $x_\infty \cong a\Lambda_B[3/k_3(\infty)]^{1/2}$. In the case of $R = 1$, the quantization parameter is approximately constant for certain groups of elements and can be estimated as

$$x_\infty(R = 1) \approx \begin{cases} 10^{-(2-3)} \ll 1, & \text{for metals, diamond,} \\ & \text{Si, Ge, Sn, Kr, and Xe;} \\ 0.1\text{–}0.2 < 1, & \text{for Ne and Ar;} \\ 0.5\text{–}1, & \text{e.g., for crystals of He and} \\ & \text{H isotopes.} \end{cases} \quad (18)$$

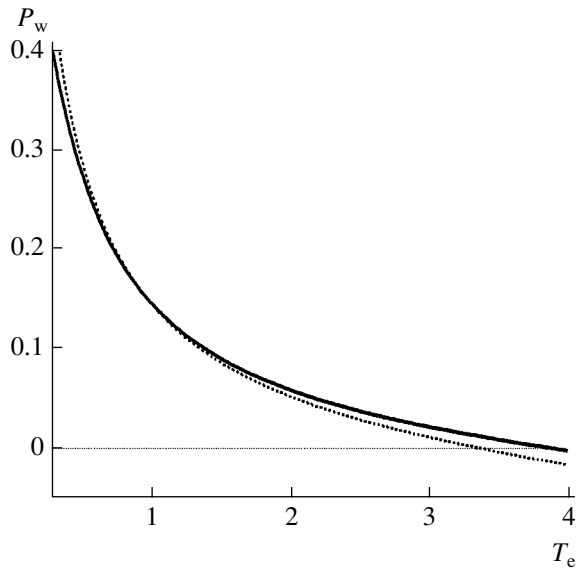

Fig. 1. Plots of the function $P_w(x_\infty, k_3^*)$ versus relative temperature $T_e = T/\Theta(\infty)$ for the quantization parameter $x_\infty = 0.01$ (corresponding to substances with strong chemical binding) and the dimensional parameter $k_3^* = 0.9$ (solid curve) and 0.5 (dotted curve). The functions $P_w(0.01, k_3^*)$ change sign at $T_{e0} = 3.94$ for $k_3^* = 0.9$ and at $T_{e0} = 3.41$ for $k_3^* = 0.5$, and intersect at the inversion temperature $T_{ei} \cong 0.95$.

Figures 1–3 show the plots of $P_w(k_3^*)$ versus the relative temperature $T_e = T/\Theta(\infty) = 0$–4 for various values of the relative mean coordination number $k_3^* = 0.1$–1.0 and the quantization parameter $x_\infty = 0.01$, 0.1, and 0.5. As can be seen, in all cases (i.e., for substances of any type), there is a temperature at which all the curves of $P_w(k_3^*, T_e)$ intersect. This point will be referred to as the "temperature of inversion of the size dependence of the surface pressure" and denoted $T_{ei}(x_\infty) = T_i(x_\infty)/\Theta(\infty)$. For $T < T_i(x_\infty)$, isothermal dispersion of the crystal leads to an increase in the surface pressure, whereas at $T >$

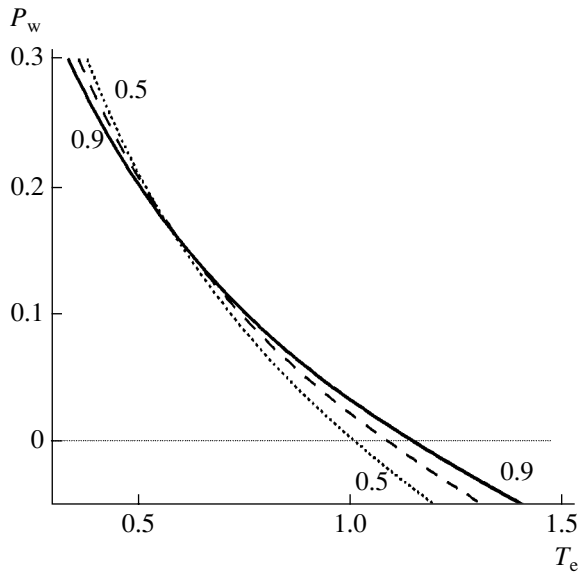

Fig. 2. Plots of the function $P_w(x_\infty, k_3^*)$ versus relative temperature $T_e = T/\Theta(\infty)$ for the quantization parameter $x_\infty = 0.1$ (corresponding to substances such as neon) and the dimensional parameter $k_3^* = 0.9$ (solid curve), 0.7 (dashed curve), and 0.5 (dotted curve). The functions $P_w(0.01, k_3^*)$ change sign at $T_{e0} = 1.16$, 1.10, and 1.02 for $k_3^* = 0.9$, 0.7, and 0.5, respectively. The three curves intersect at the inversion temperature $T_{ei} \cong 0.58$.

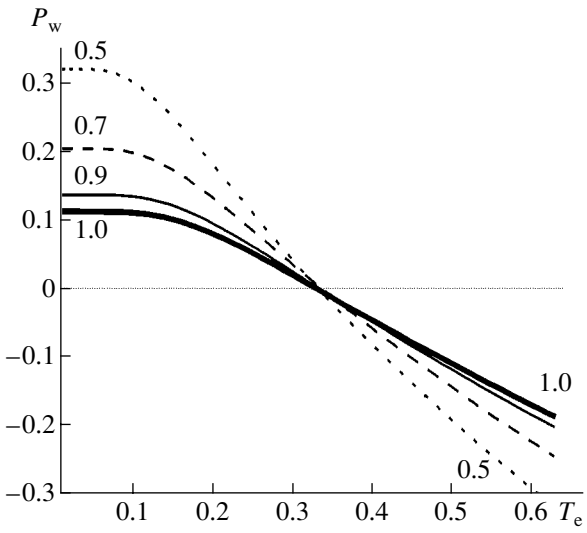

Fig. 3. Plots of the function $P_w(x_\infty, k_3^*)$ versus relative temperature $T_e = T/\Theta(\infty)$ for the quantization parameter $x_\infty = 0.5$ (corresponding to an *o*-D_2 crystal) and the dimensional parameter $k_3^* = 1.0$ (thick solid curve), 0.9 (thin solid line), 0.7 (dashed curve), and 0.5 (dotted curve). All the functions $P_w(0.5, k_3^*)$ change sign and intersect at $T_{ei0} = 0.336$ (i.e., the inversion and "zero-surface-pressure" temperatures coincide).

$T_i(x_\infty)$, the dispersion leads to an increase in $P_w(N)$. The data in Figs. 1–3 show that the relative inversion temperature decreases with increasing parameter x_∞.

As can be seen from Figs. 1–3, the relative temperature, $T_{e0} = T_0(x_\infty)/\Theta(\infty)$ at which the function $P_w(k_3^*, T_e)$ changes sign decreases with increasing "quantization" parameter x_∞. This "zero-surface-pressure" temperature depends both on the quantization parameter x_∞ and on the relative mean coordination number (dimensional parameter) k_3^*. As can be clearly seen in Figs. 1–3, the slope of the $T_{e0}(k_3^*)$ dependence decreases to zero for $x_\infty = 0.5$ and becomes negative for $x_\infty > 0.5$.

The observed behavior can be explained by the competition of two forces operating on the surface of the nanocrystal:

(i) The resultant force of attraction of a surface atom to the surrounding atoms. This force (which is maximum for atoms occurring on the edges and, especially, at the vertices of the nanocrystal) tends to draw the surface atom inside the nanocrystal and compresses the nanocrystal: the greater the dimensional parameter k_3^*, the stronger the compression.

(ii) The force resulting from atomic oscillations, the energy of which increases with the temperature. This force, which tends to knock the surface atom out of the crystal, produces expansion of the nanocrystal surface.

At low temperatures, the first (compressing) force predominates. As the temperature increases, the second (expanding) force grows (this growth being more pronounced for the greater dimensional parameter k_3^*). As a result, at a certain temperature of inversion of the size dependence of the surface pressure, $T_{ei}(x_\infty)$, the size-dependent variation of the first and second forces compensate one another. At the "zero-surface-pressure" temperature, $T_{e0}(x_\infty)$, the two forces equilibrate each other. The greater the dimensional parameter k_3^*, the higher the contribution of the expanding "vibrational" force and the lower the T_{ei} and T_{e0} values.

It is this interplay of the surface factors that accounts for the contradictory experimental data reported in the literature, whereby the same substance can be characterized by a lattice parameter decreasing or increasing (or remaining unchanged) in the course of dispersion (decrease in size) of nanocrystals (see reviews [3–7, 17, 18]).

Acknowledgments. The author is grateful to A.D. Filenko, K.N. Magomedov, and Z.M. Surkhaeva for their help with this paper.

This study was supported by the Russian Foundation for Basic Research (project no. 02-03-33301) and the Russian Academy of Sciences (OEMMPU project no. 7/067-095/050504-229).

REFERENCES

1. L. D. Landau and E. M. Lifshitz, *Course of Theoretical Physics*, Vol. 5: *Statistical Physics* (Nauka, Moscow, 1976; Pergamon, Oxford, 1980), Part 1.
2. I. P. Bazarov, *Thermodynamics* (Vysshaya Shkola, Moscow, 1976; Pergamon Press, Oxford, 1964).
3. L. K. Grigor'eva, N. S. Lidorenko, E. L. Nagaev, *et al.*, Fiz. Tverd. Tela (Leningrad) **29**, 1517 (1987) [Sov. Phys. Solid State **29**, 868 (1987)].
4. V. I. Gorchakov, E. L. Nagaev, and S. P. Chizhik, Fiz. Tverd. Tela (Leningrad) **30**, 1068 (1988) [Sov. Phys. Solid State **30**, 620 (1988)].
5. Yu. I. Petrov, Zh. Fiz. Khim. **63**, 2757 (1989).
6. V. I. Zubov, I. D. Morokhov, and N. P. Tret'yakov, *Problems of Quantum and Statistical Physics* (Univ. Druzhby Narodov, Moscow, 1989), pp. 108–116.
7. E. L. Nagaev, Usp. Fiz. Nauk **162** (9), 49 (1992) [Sov. Phys. Usp. **35**, 747 (1992)].
8. J. W. Gibbs, *Thermodynamics and Statistical Mechanics (The Collected Works)* (Yale Univ. Press, New Haven, Conn., 1948).
9. M. N. Magomedov, Fiz. Tverd. Tela (St. Petersburg) **45**, 907 (2003) [Phys. Solid State **45**, 953 (2003)].
10. M. N. Magomedov, Fiz. Tverd. Tela (St. Petersburg) **45**, 1159 (2003) [Phys. Solid State **45**, 1213 (2003)].
11. M. N. Magomedov, Fiz. Tverd. Tela (St. Petersburg) **46**, 924 (2004) [Phys. Solid State **46**, 954 (2004)].
12. M. N. Magomedov, Zh. Fiz. Khim. **62**, 2103 (1988).
13. M. N. Magomedov, Zh. Fiz. Khim. **63**, 2943 (1989).
14. M. N. Magomedov, Zh. Fiz. Khim. **61**, 1003 (1987).
15. M. N. Magomedov, Fiz. Tverd. Tela (St. Petersburg) **45**, 33 (2003) [Phys. Solid State **45**, 32 (2003)].
16. J. O. Hirschfelder, Ch. F. Curtiss, and B. B. Bird, *Molecular Theory of Gases and Liquids* (Wiley and Sons, New York, 1954).
17. Yu. I. Petrov, *Physics of Small Particles* (Nauka, Moscow, 1984) [in Russian].
18. A. I. Gusev and A. A. Rempel', *Nanocrystalline Materials* (Fizmatlit, Moscow, 2001) [in Russian].

Translated by P. Pozdeev

Technical Physics Letters, Vol. 31, No. 1, 2005, pp. 18–20. Translated from Pis'ma v Zhurnal Tekhnicheskoĭ Fiziki, Vol. 31, No. 1, 2005, pp. 35–41.

Variability of the Elastic Properties of Multiwalled Carbon Nanotubes

V. A. Gorodtsov and D. S. Lisovenko*

Institute for Problems in Mechanics, Russian Academy of Sciences, Moscow, Russia

** e-mail: lisovenk@ipmnet.ru*

Received July 16, 2004

Abstract—The results of numerous experimental investigations of carbon nanotubes show evidence of a considerable variability in their mechanical properties. Based on the common features of the structures of graphite and multiwalled carbon nanotubes (MWNTs), it is demonstrated that structural polytype transitions are among the probable factors responsible for this variability. Analysis of the MWNT behavior under torsion shows that the torsional stiffness of MWNTs depends on the elastic moduli, the number and magnitudes of which vary with the local symmetry of the MWNT structure (on the transition from rhombohedral to hexagonal and turbostratic modifications). The effect of structural transformations on the Young modulus in stretched MWNTs is evaluated. © *2005 Pleiades Publishing, Inc.*

Introduction. Carbon nanotubes (CNTs), which have been extensively studied in recent years, are structurally close to graphite (to a certain approximation, these tubes can be considered as graphite sheets rolled up into cylinders). For this reason, the properties of CNTs are also much like the properties of graphite. On the other hand, since the transverse dimensions of CNTs are comparable with the interatomic distance, thin tubes also exhibit significant differences from graphite (i.e., the scaling effect takes place).

The results of numerous experimental investigations into the mechanical characteristics of CNTs show considerable variability of the values obtained in various studies, even in the course of repeated measurements in the same experiment (see review [1]). This variability of elastic properties was observed, in particular, in the study of the torsional oscillations of multiwalled carbon nanotubes (MWNTs) [2]. The obtained estimates of the torsional stiffness and the corresponding effective shear moduli showed evidence of a significant (tenfold) increase in these values in the course of repeated twisting. These changes were assigned [2] to modification of the mechanical bonds between the adjacent graphene shells of MWNTs, influencing their behavior in the course of subsequent torsional oscillations. The experimental results [2] were interpreted under the assumption that force moments were applied directly to the outer shell of an MWNT, whereas the inner cylindrical layers could readily slip with respect to one another and weakly interacted with the outer shell. Other experimental and theoretical data [3, 4] confirmed the assumption concerning small friction between graphene layers, with these interactions possessing a van der Waals character in contrast to the strong covalent binding within each shell. The primary slippage of the inner layers could result in a small effective thickness of the loaded part of the CNT, thus accounting for the understated torsional stiffness. The growth of the torsional stiffness in the course of repeated loading was attributed [2] to an increase in the effective thickness due to the increasing coupling between the (initially sliding) shells, which was explained by distortion of the tube shape and the formation of strain-induced structural defects.

We would like to concentrate on a somewhat different possibility. We believe that the observed variability in elastic properties can also be related to the phase (polymorphous) transitions proceeding in strained CNTs. As is well known, natural graphite contains, in addition to the main hexagonal α phase, a considerable proportion of rhombohedral (trigonal) β graphite. The difference between the α and β phases reflects symmetry-related distinctions between the two types of sequential packaging of graphene planes uniformly covered by hexagons of covalent bonds between carbon atoms. The hexagonal and rhombohedral configurations correspond to different sequences of graphene planes of the *ABAB*… and *ABCABC*… types. Note that differences between the elements *A*, *B*, and *C* consist only in small parallel shifts of the otherwise similar graphene planes. The same situation takes place in MWNTs consisting of several graphene sheets rolled up into cylinders. Easy relative slippage of the graphene planes in the graphite or cylindrical shells in nanotubes implies readily proceeding phase transitions from one type of crystal structure to another caused by small shear strains. The elastic properties of the hexagonal and rhombohedral graphite modifications (in CNTs, the symmetry differences are retained on a local level) may differ not only in the magnitude of the elastic moduli, but in their number as well [5].

1063-7850/05/3101-0018$26.00 © 2005 Pleiades Publishing, Inc.

Torsion of nanotubes. Let us consider a small homogeneous torsion of a hollow cylindrical rod, representing the simplest model of an MWNT in the continuum approximation. This analysis is, in fact, a simple generalization of the solution of a classical problem with isotropic elasticity [5] for the case of a crystal possessing the rhombohedral symmetry. The result for a hexagonal crystal will be obtained as a particular case.

In the case of small strain in a rhombohedral graphite structure, the tensor of elastic moduli λ_{ijkl} determining the linear relationship between the stress tensor σ_{ij} and the strain tensor u_{kl} (Hooke's law)

$$\sigma_{ij} = \lambda_{ijkl}u_{kl}, \quad \lambda_{ijkl} = \lambda_{jikl} = \lambda_{klij}, \tag{1}$$

is represented by six independent moduli:

$$\lambda_{1111}, \lambda_{1122}, \lambda_{2233}, \lambda_{2323}, \lambda_{3333}, \lambda_{1123}. \tag{2}$$

Here, the graphene plane is basal and coincides with the plane (1), (2), while the crystallographic *c*-axis corresponds to the third direction.

Proceeding to the MWNT model in the form of a hollow cylindrical rod, we use a simplifying assumption concerning the validity of the corresponding Hooke's law with constant elastic moduli in the orthogonal curvilinear system of coordinates (r, φ, z) related to the rod. In the theory of anisotropic elasticity, this situation is referred to as curvilinear anisotropy [6]. This approximation is based on the fact that graphene plane (1), (2) in the cylindrical rod model is rolled up into a circular cylindrical surface (z, φ) and retains a local crystal symmetry.

The main relations of the elasticity theory (the equilibrium equations and Hooke's law) for the homogeneous torsion of this rod are satisfied provided that only the following components of the displacement vector, the strain tensor, and the stress tensor are nonzero:

$$u_\varphi = zr\tau, \quad u_z = \frac{\lambda_{1123}}{2\lambda_{2323}}r^2\tau, \quad u_{z\varphi} = \frac{\tau}{2}r, \quad u_{zr} = \frac{\lambda_{1123}}{2\lambda_{2323}}r\tau, \tag{3}$$

$$\sigma_{z\varphi} = \frac{\tau}{2}\left(\lambda_{1111} - \lambda_{1122} - \frac{2\lambda_{1123}^2}{\lambda_{2323}}\right)r, \tag{4}$$

where τ is the torsion angle (proportional to the torque $M = C\tau$ of the pair of forces applied to the free rod end). The torsional stiffness coefficient C also enters into a linear relation for the elastic energy per unit length of the rod:

$$F = \frac{1}{2}\int \sigma_{\alpha\beta}u_{\alpha\beta}df = \frac{1}{2}C\tau^2. \tag{5}$$

Calculation of the energy integral for a hollow cylindrical rod with the outer and inner radii R_2 and R_1, respectively, leads to the following expressions of the torsional stiffness in terms of the elastic moduli and radii:

$$C = \frac{\pi}{4}\left(\lambda_{1111} - \lambda_{1122} - \frac{2\lambda_{1123}^2}{\lambda_{2323}}\right)(R_2^4 - R_1^4) = \frac{\pi}{4}\left(c_{11} - c_{12} - \frac{2c_{14}^2}{c_{44}}\right)(R_2^4 - R_1^4). \tag{6}$$

Here, the second representation makes use of the conventional matrix notation for the elastic coefficients (instead of the tensor quantities).

Thus, the torsional stiffness of an MWNT with a periodic shell packaging of the *ABCABC*… type is proportional to one positive definite combination of four elastic moduli. In a particular case of $c_{14} = \lambda_{1123} = 0$, we obtain the corresponding value for a periodic shell packaging of the *ABAB*… type:

$$C = \frac{\pi}{4}(c_{11} - c_{12})(R_2^4 - R_1^4). \tag{7}$$

Here, the torsional stiffness is proportional to the difference of only two elastic moduli. Eventually, in the course of the transition from one crystal structure type to another, a change in the torsional stiffness is primarily related to the appearance of a new modulus (c_{14}) and to a change of the c_{44} value. Significant variations in the other two moduli, c_{11} and c_{12}, are unlikely because these coefficients reflect the high stiffness of the graphene layer, which is not significantly influenced by a change in the order of alternation of weakly interacting, rather distant, shells of an MWNT. In contrast, the shear modulus c_{44} may be expected to exhibit significant variations in response to a change in the character of relative displacement of the adjacent graphene layers. According to the experimental data [7], this quantity (the smallest among elastic moduli) exhibits a considerable (severalfold) scatter. Quantitative estimates of the related variability are difficult to obtain because no experimental data are available for the elastic moduli of rhombohedral graphite.

The aforementioned possibility of a phase transition with the transformation of the periodic structure of nanotubes occurring in the course of torsion is neither the only nor the most likely one. In the case of small straining, a more probable scenario seems to be that with sequentially accumulated local disorder in the periodic packaging of layers in MWNTs. Such a primary disorder in layer packaging is called a stacking fault. As the straining develops, the stacking faults are accumulated in a way that may eventually lead to the formation of structures with a random alternation of layers. In the case of graphite, this corresponds to the formation of a turbostratic modification, which is most favorable from the standpoint of entropy. This term may be applied to MWNTs with randomly packaged cylindrical graphene layers.

In the absence of ordered graphene layers, turbostratic graphite possesses, on average, a transverse isotropy because the *c*-axis perpendicular to these planes is, in fact, the axis of infinite order (C_∞). A conditional average for the elastic moduli, whereby one (e.g., the outer) layer is fixed, differs little from the turbostratic situation. This system is characterized by the same symmetry axis of the sixth order as that for the external layer. For the elastic properties under consideration, this implies a continuous symmetry of the basal plane (transverse isotropy) [5]. Thus, in CNTs of the hexagonal and turbostratic types, the variability can be related only to differences in the values of elastic moduli. We may expect that the shear modulus would grow with the increasing number of defects in the material.

The above considerations were based on the assumption concerning the possibility of describing MWNTs within the framework of the theory of continuum. However, as the shell thickness and diameter decrease, the discrete character of the molecular structure of the CNTs will be more pronounced. This will lead, in particular, to a difference in the symmetry of CNTs formed in different variants of the process of rolling the graphene layer into tubes. The CNTs may exhibit a difference in helicity [1], which will also lead to a certain variation of their elastic properties.

Stretching of nanotubes. The possible easy transformation of structural polytypes into one another may, generally speaking, also account for the variability of some of the other mechanical characteristics of layered materials.

Below, we restrict the analysis to evaluation of the stretching of a hollow cylindrical rod with a curvilinear anisotropy of the rhombohedral (in particular, hexagonal) type. This rod model successfully simulates MWNTs. The straining of a rod with this anisotropy by the stretching force *p* (per unit surface area of the edge cross section) is radially inhomogeneous (the homogeneous case corresponds to an isotropic material [5]). In this case, the only nonzero normal components of the stress tensor are

$$\sigma_{rr}(r), \quad \sigma_{\varphi\varphi}(r), \quad \sigma_{zz}(r) \quad (\sigma_{r\varphi} = \sigma_{z\varphi} = \sigma_{zr} = 0), \quad (8)$$

which exhibit power dependence on the radial coordinate. The general character of the stressed state in a cylindrical tube remains unchanged upon the transition from local rhombohedral to hexagonal symmetry.

Taking into account Hooke's law, the equations of equilibrium, and the boundary conditions on the side and edge faces of the model hollow rod, we obtain a relation between the load *p* and the longitudinal strain component u_{zz}, which proves to be independent of the radial coordinate. Then, the ratio $p/u_{zz} = E$ determines the dependence of the Young modulus on the four moduli of compliance and the ratio of the inner and outer radii of the hollow cylinder (this cumbersome expression is not presented here). For a thin-walled tube ($R_2 - R_1 \ll R_2$), only the dependence on a single compliance modulus is retained, and the expressions simplify to

$$E \approx \frac{1}{s_{11}}, \quad (9)$$

$$2s_{11} = \frac{c_{33}}{(c_{11}+c_{12})c_{33} - 2c_{13}^2} + \frac{c_{44}}{(c_{11}-c_{12})c_{44} - 2c_{14}^2}. \quad (10)$$

As can be seen from the last formula, this single compliance modulus is expressed via five elastic moduli, one of which (c_{14}) vanishes in the partial case of α graphite.

Estimation of the Young modulus of an MWNT with a local hexagonal symmetry using the elastic moduli of α graphite [7] yields an experimentally confirmed result: $E \approx 1$ TPa.

On stretching a locally-rhombohedral tube, the longitudinal tensile strain is accompanied by a transverse contraction and inhomogeneous shear,

$$u_{r\varphi} = \frac{s_{14}}{2}(\sigma_{\varphi\varphi}(r) - \sigma_{zz}(r)), \quad (11)$$

$$s_{14} = -\frac{c_{44}}{(c_{11}-c_{12})c_{44} - 2c_{14}^2}, \quad (12)$$

which may lead to a phase transformation of the structure as a result of the facilitated slippage of graphene shells. However, relations (9) and (10) show that significant variability of the Young modulus during such structural polytype transitions is unlikely.

Acknowledgments. This study was supported by the Russian Academy of Sciences (OEMMPU program no. 13).

REFERENCES

1. D. Qian, G. J. Wagner, W. K. Liu, *et al.*, Appl. Mech. Rev. **55**, 495 (2002).
2. P. A. Williams, S. I. Papadakis, A. M. Patel, *et al.*, Phys. Rev. Lett. **89**, 255502 (2002).
3. J. Cumings and A. Zettl, Science **289**, 602 (2000).
4. J. Servantie and P. Gaspard, Phys. Rev. Lett. **91**, 185503 (2003).
5. L. D. Landau and E. M. Lifshitz, *Course of Theoretical Physics*, Vol. 7: *Theory of Elasticity* (Nauka, Moscow, 1987; Pergamon, New York, 1986).
6. S. G. Lekhnitskiĭ, *Elasticity Theory for Anisotropic Solids* (Gostekhizdat, Moscow, 1950) [in Russian].
7. O. L. Blakslee, D. G. Proctor, E. J. Seldin, *et al.*, J. Appl. Phys. **41**, 3373 (1970).

Translated by P. Pozdeev

Technical Physics Letters, Vol. 31, No. 1, 2005, pp. 21–24. Translated from Pis'ma v Zhurnal Tekhnicheskoĭ Fiziki, Vol. 31, No. 1, 2005, pp. 42–49.

Point Defects as the Centers of Titanium Dioxide Sensitization in the Visible Spectral Range

A. A. Lisachenko* and R. V. Mikhaĭlov

Fock Institute of Physics, St. Petersburg State University, St. Petersburg, Russia

** e-mail: lisachen@photonics.phys.spbu.ru*

Received July 1, 2004

Abstract—The formation of surface point defects in the initial stage of TiO_2 reduction ($x \le 10^{12}$ cm^{-2}) has been studied by mass spectrometry and ultraviolet photoelectron spectroscopy (UPS). Heating to 720 K or UV illumination in ultrahigh vacuum creates surface color centers in TiO_2 with an energy spectrum extending from the Fermi level to the valence band top. The continuous photoelectron spectrum exhibits a peak at 2.7 eV, which varies in a manner correlated with the behavior of the optical absorption bands at 2.55 and 2.81 eV assigned to oxygen vacancies in the TiO_2 crystal structure. The interaction of the surface point defects with molecular oxygen has been studied and a special form of the photoadsorbed oxygen (with E_{des} = 1.37 eV) is found. It is shown that the surface color centers may serve as centers of TiO_2 sensitization in the visible spectral range.

Introduction. Titanium dioxide (TiO_2) is among the most extensively studied oxide compounds [1]. This is related, in particular, to the wide use of TiO_2 for photoelectric and photocatalytic conversion of UV radiation energy in the region of intrinsic optical absorption ($\lambda < 380$ nm or $h\nu \ge 3.2$ eV) [2, 3]. Since this spectral range accounts for less than 3% of the total solar radiation, it is a usual practice to shift the sensitivity range of TiO_2 toward the visible spectral interval by doping the base oxide with organic dyes or ambivalent metals [4]. However, organic dyes sharply reduce the possibility of using the doped material in ultrahigh-vacuum (UHV) technologies, while foreign metal ligands decrease the efficiency of photoconversion in the UV range [5]. In this context, it was of interest to study the possibility of sensitizing TiO_2 by using the intrinsic structural defects possessing absorption bands in the visible range [1, 6, 7]. A relatively small concentration of such defects might be compensated by rather long lifetimes of their excited states [8].

The efficiency of defects in photoactivated reactions with charge transfer is determined by a combination of optical, electrical, and kinetic parameters characterizing the nature of the optical transition, the positions of local levels in the energy bands, and the cross sections of the interaction with reactants. Unfortunately, data available on the nature and properties of color centers are very restricted, since the overwhelming majority of experimental investigations were performed on stoichiometric (free of color centers) TiO_2 and the reported results refer predominantly to the most readily accessible (110) face of rutile, which is the most stable crystal modification of titanium dioxide [1].

The aim of this study was to determine the conditions of formation of color centers in readily available, practically used meso- and nanostructures of TiO_2, to study the mechanism of electron transfer for the surface defects, and to search for correlations in the chain "atomic defect structure–electron energy spectrum–optical spectrum–adsorption characteristics."

Experimental. The investigation was performed on TiO_2 of a Degussa P-25 grade, which is most widely used in various technologies [1]. This material comprises a mixture of meso- and nanoparticles of anatase and rutile, with an average grain size of ~50 nm, and is free of color centers in the initial state. The structural defects were generated under the action of "soft" factors, by thermo- or photoactivation under UHV conditions. Oxygen exchange with the gas phase was monitored by determining changes in the gas-phase composition with the aid of mass spectrometry. The adsorbed phase was studied by method of thermodesorption spectroscopy (TDS). Variations in the energy spectrum of electron states, the magnitude of band bending, and the Fermi level position, were studied *in situ* by means of UV photoelectron spectroscopy (UPS) [7]. A change in the optical absorption of a sample in the interval from 0.5 to 5.0 eV was monitored by diffuse reflectance spectroscopy [7].

The UPS measurements were performed using the photoelectron spectrometer (8.43 eV) described in [9], which was specially modified for *in situ* investigation of the ultimately low density of electron states in the

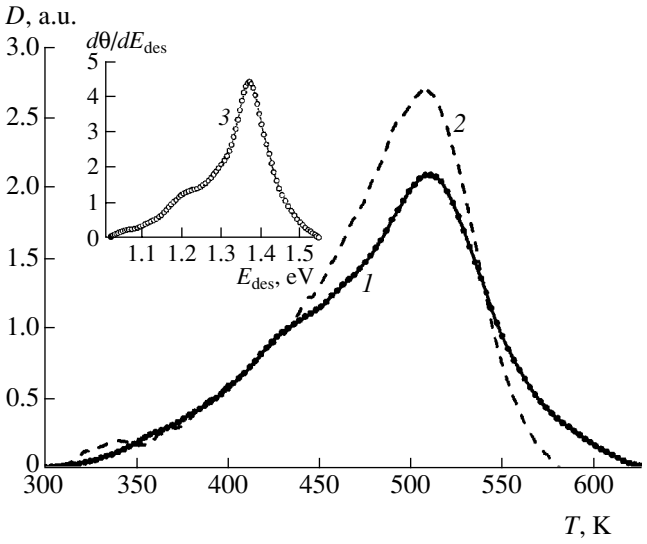

Fig. 1. Thermodesorption spectra of oxygen adsorbed on TiO_2 upon reduction (*1*) by heating and (*2*) by illumination under UHV conditions. The inset shows the results of numerical calculations of the desorption rate $d\theta/dt$ as a function of E_{des} using the Polyanyi–Wigner equation.

bandgap. The energy resolution of the instrument was not worse than 100 meV, and the accuracy of the energy calibration relative to E_F was 10 meV. The high aperture of the electron energy analyzer (34°) and the use of finely dispersed samples made it possible to obtain photoelectron spectra integrated over all the possible values of the wavevector **k** that is of principal significance for research.

The as-received TiO_2 samples were preliminarily purified *in situ* in a flow of pure oxygen (99.99% O_2 at the reactor input) at a pressure of 0.5 Torr and a temperature of $T = 750$ K, with continuous monitoring of the gas phase composition at the exit of the reactor. In the initial stage of heating, the analyses showed the desorption of a considerable amount of H_2O, CO, NO, and NO_2. The samples were heated in oxygen for not less than 200 h, until the oxygen concentration in the gas phase reached 99.9% at $T = 750$ K. This condition of the TiO_2 sample will be referred to as the initial "oxidized" state. Then, "reduced" samples were obtained by heating the initial "oxidized" material under UHV conditions at $T = 750$ K. The regimes of thermal treatments were selected so as to retain the initial content of the anatase and rutile phases in the samples and to ensure high reproducibility of the experimental results.

The samples were exposed to the radiation of a high-pressure mercury lamp (DRT-120) with a thermal filter and a set of standard optical filters (LOMO, Russia). The experimental procedures are described in more detail elsewhere [7].

TDS study of adsorbed oxygen species. Heating or illumination of the initial "oxidized" TiO_2 sample under UHV conditions are accompanied by the desorption of oxygen and the appearance of optical absorption in the 0.5–3.2 eV range. This coloration was attributed to the optical absorption by free electrons (a continuum at $h\nu \le 1.5$ eV), Ti^{3+} ions (a band at 2.0 eV), and oxygen vacancies (bands at 1.17, 2.55, and 2.81 eV) [7]. The reverse effects, manifested by the adsorption of oxygen and bleaching of the sample, were observed during subsequent heating or illumination of the sample in an oxygen-containing atmosphere. Although the amount of adsorbed and photoadsorbed oxygen in our experiments did not exceed 10^{-4} monolayer, this nevertheless led to dramatic changes in the optical and photoelectron spectra of TiO_2.

Figure 1 shows the typical thermodesorption spectrum of oxygen (curve *1*) adsorbed on a "reduced" (see above) sample. In addition to the main desorption peak with a maximum at 510 K, there are two smaller maxima at 360 and 425 K. The peak at 410–430 K is characteristic of TiO_2 reduction and assigned to the radical-anion O_2^- adsorbed species. Using the intensity of this peak, it is possible to evaluate the concentration of electron-donor centers on the sample surface [7]. The peak at 360–380 K is retained in oxidized (bleached) samples. The process of desorption at 460–600 K is explained by decomposition of the $[O_s^- \ldots O_2]$ complexes formed as a result of the interaction between O_2 and the hole centers in wide-bandgap oxides [8]. This form of adsorbed oxygen is specific to photoadsorption (Fig. 1, curve *2*). Changes in the thermodesorption spectrum observed in the high-temperature region ($T > 540$ K) upon illumination of the samples will be considered separately.

The results of the TDS measurements are indicative of the presence of energetically nonuniform adsorption bonds. In order to determine the kinetic parameters from the experimental thermodesorption spectra, it is possible to use the general form of the Polyanyi–Wigner equation,

$$-d\theta/dt = \nu(\theta^n/\beta)\exp(-E_{des}/(RT)),$$

where θ is the surface coverage of the adsorbate, ν is the frequency factor, n is the order of desorption ($n = 1$ and 2 for the molecular and associative desorption, respectively), and β is the linear sample heating rate used in TDS measurements.

The $E_{des}(\theta)$ function was determined by numerically solving a system of equations for the $d\theta/dt$, θ, and T values at each point of the experimental spectrum. The parameters ν and n were selected so that the error of approximation would not exceed the experimental uncertainty. The resulting distribution function is presented in the inset in Fig. 1 (curve *3*). As can be seen, this curve reveals three peaks corresponding to the des-

orption energies E_{des} = 1.05, 1,25, and 1.37 eV on a continuous background.

UPS investigation. Figure 2 shows the pattern of evolution of the photoelectron spectra measured in the course of various treatments of TiO_2 samples. The samples in the as-received state had a thermoelectric work function of φ_1 = 4.1 eV, a photoelectric work function of φ_2 = 4.6 eV, and a spectrum of occupied states beginning 0.5 eV below the Fermi level E_F' (Fig. 2, curve *1*). After the standard training in oxygen (i.e., in the initial "oxidized" state), the Fermi level decreased by 0.5 eV (E_F), so that φ_1 increased to 4.6 eV (and remained in this position in the course of subsequent experiments), whereas φ_2 unchanged (Fig. 2, curve *2*). In the course of subsequent heating of the "oxidized" sample under UHV conditions, whereby the mass spectra showed desorption of oxygen, the density of occupied states, according to the photoelectron spectra, increased in the entire energy range, as manifested by the peaks at 1.95, 2.3, 2.75, 3.15, and 3.75 eV (Fig. 2, curves *3* and *5*). The following admission of oxygen restored the initial spectrum (Fig. 2, curve *2*) and removed the heating-induced coloration. The reduction–oxidation cycles could be multiply repeated, showing reproducible characteristics of the sample.

The density of states could be also increased by illumination of the sample under UHV conditions (Fig. 2, curves *4* and *6*). A specific feature of the photoreduction is the appearance of states in the region of 3.8–4.3 eV, the appearance of peaks at 0.7 and 0.1 eV, and an increase in the relative contribution of states in the 2.7–3.2 eV interval. The spectral features at 2.7–3.2 eV are probably related to an increase in the oxygen adsorption coverage observed for illuminated samples (Fig. 1, curve *2*). Indeed, the electron states at 2.7–3.2 eV in the photoelectron spectra, as well as the adsorbed oxygen species with E_{des} = 1.37 eV (Fig. 1, curve *2*), are formed both in the dark and during photoadsorption, whereas the states at 3.8–4.3, 0.7, and 0.1 eV do not appear upon thermal reduction.

With respect to the method of formation and the character of interaction with oxygen, the behavior revealed by UPS correlates with that observed in the spectra of induced optical absorption studied previously [7]. The optical absorption bands at 2.55 and 2.81 eV, assigned to the oxygen vacancies in TiO_2, correlate with the photoelectron peak at 2.7 eV. It should be noted that the formation of paramagnetic complexes $[O_s^- \ldots O_2]$ in TiO_2 irradiated with 2.8-eV quanta in oxygen was also revealed by EPR [10]. The hole centers O_s^- are formed as a result of the electron transfer from the neighboring anion to a resonance-excited oxygen vacancy. The adsorption on the hole centers corresponds to a thermodesorption peak with E_{des} = 1.37 eV. This form of photoadsorbed oxygen is characterized by high activity in the reactions of oxidation and isotope exchange [8].

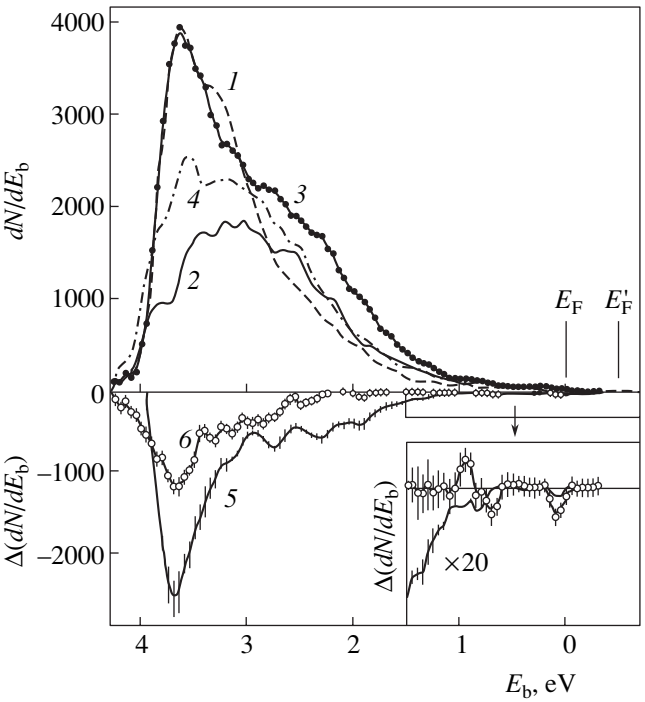

Fig. 2. UV photoelectron spectra of TiO_2 in various states: (*1*) as-received; (*2*) purified ("oxidized") by heating in oxygen; (*3*, *4*) reduced in UHV by heating to 723 K or illumination, respectively; the difference curves *5* (curve *3* subtracted from curve *2*) and *6* (curve *4* subtracted from curve *2*) reveal the effects of reduction. The binding energy E_b is measured from the Fermi level; E_F' and E_F are the positions of the Fermi level in the as-received and purified ("oxidized") sample, respectively.

In conclusion, thermo- and photoactivation of TiO_2 in vacuum may provide the formation of local color centers in the entire visible spectral range. These centers correspond to a continuous spectrum of electron states extending from the valence band top to the Fermi level. All these color centers interact with molecular oxygen to form di- and triatomic charge transfer complexes. The results of our investigation have revealed correlations in the chain "atomic defect structure–electron energy spectrum–optical spectrum–adsorption characteristics." It is established that the interaction of molecular oxygen with photoactivated *F*-type centers leads to the formation of a specific active oxygen form with E_{des} = 1.37 eV. The whole body of obtained data points to the possibility of using *F*-type intrinsic defects for TiO_2 sensitization in the visible spectral range.

Acknowledgments. This study was supported by the Ministry of Science and Education of the Russian Federation within the framework of the Federal Scientific-Technological Program "Research and Development in Preferred Scientific Directions 2002–2006"

(State Contract no. 40.012.1.1.1152) and by the INTAS Foundation (grant no. 03-51-6088).

REFERENCES

1. U. Diebold, Surf. Sci. Rep. **48**, 53 (2003).
2. M. Anpo, Stud. Surf. Sci. Catal. **130**, 157 (2000).
3. M. Formenti, H. Courbon, A. Lissatchenko, *et al.*, J. Vac. Sci. Technol. **9**, 947 (1972).
4. H. Yamashita, M. Harada, A. Tanii, *et al.*, Catal. Today **63**, 63 (2000).
5. N. Serpone, D. Lawless, J. Disdier, *et al.*, Langmuir **10**, 643 (1994).
6. I. Nakamura, N. Negishi, S. Kutsuna, *et al.*, J. Mol. Catal. A: Chem. **161**, 205 (2000).
7. A. A. Lisachenko, V. N. Kuznetsov, M. N. Zakharov, and R. V. Mikhailov, Kinet. Katal. **45**, 205 (2004).
8. A. A. Lisachenko, Phys. Low-Dimens. Semicond. Struct. **7**/**8**, 1 (2000).
9. P. O. Artamonov and A. A. Lisachenko, Khim. Fiz. **11**, 344 (1992).
10. A. E. Cherkashin, A. M. Volodin, S. V. Koshcheev, *et al.*, Usp. Fotoniki **7**, 86 (1980).

Translated by P. Pozdeev

Technical Physics Letters, Vol. 31, No. 1, 2005, pp. 25–26. Translated from Pis'ma v Zhurnal Tekhnicheskoĭ Fiziki, Vol. 31, No. 1, 2005, pp. 50–53.

Effect of Oxygen Deficiency on the Cationic States of Iron in a Series of Oxides with Various Perovskitelike Structures

L. D. Zaripova, N. V. Boltakova, A. A. Valiullin, and Sh. Sh. Bashkirov

Kazan State University, Kazan, Tatarstan, Russia
Proton R&D Center, Kazan, Tatarstan, Russia
e-mail: public.mail@ksu.ru; proton@tbit.ru
Received July 14, 2004

Abstract—Compounds representing several series of complex oxides with perovskitelike structures have been studied by Mössbauer spectroscopy. Analysis of the quadrupole splitting–isomer shift diagrams constructed using the results of these measurements shows that increasing oxygen deficiency in the structures of the compounds studied is accompanied by variation of the coordination and valence state of iron. *© 2005 Pleiades Publishing, Inc.*

Complex oxides of copper and other *d* metals possessing anion-deficient perovskitelike structures have received much attention due to variable crystallographic coordination and mixed valence of metal ions in these compounds. This interest is related to the prospects of obtaining, by means of controlled variation of the cation composition in a broad range, compounds with desired combinations of properties. The large variety of possible cation substitutions suggests that this modification offers a powerful method for obtaining materials with unusual characteristics. On the other hand, the crystal structure and physical properties of these complex oxides strongly depend on the concentration and arrangement of oxygen vacancies [1].

The ability of trivalent iron to adopt octahedral and (to a lesser extent) pyramidal coordination suggests that iron can substitute for copper in a regular manner. Using the method of selective doping, it is possible not only to obtain substituted compounds but also to stabilize complex oxides with perovskitelike structures in systems with rare earth elements [2–4].

We studied a series of compounds belonging to orthoferrites, $LnFe_{2/3}Mo_{1/3}O_3$ (Ln = La, Ce, Pr, Nd), and oxygen-deficient perovskitelike oxides of various structural types: $Pr_4BaCu_4FeO_{13-\delta}$ (δ = 0, 0.5; 4–1–5 type), $Ln_{8-y}Sr_yCu_{8-x}Fe_xO_{20}$ (Ln = La, Nd, Pr; y = 1.6–4; x = 1.6–3; 8–8–20 type), and $YBa_{2-y}La_yCu_{3-x}Fe_xO_{7-\delta}$ and $Y_{1-y}Ca_yBa_{2-y}La_yCu_{3-x}Fe_xO_{7-\delta}$ (y = 0.25, 05; x = 0.06, 0.12; $\delta \approx 0.05$; 1–2–3 type). All compounds were obtained from the laboratory headed by Prof. G.V. Bazuev at the Institute of Solid State Chemistry (Ural Division, Russian Academy of Sciences, Yekaterinburg).

The main method used in our investigation was Mössbauer spectroscopy using ^{57}Fe isotope. In some cases, additional information was obtained by means of X-ray diffraction.

The perovskitelike structures of all types studied in our experiments have a common distinctive feature in the form of layers, packets, or frameworks of MeO_6 octahedra sharing vertices (Me = Cu, Fe, and Mo) or their residues—MeO_5 pyramids, MeO_4 squares, or MeO_2 dumbbells in oxygen-deficient compounds [5].

The samples were selected and studied in a certain order, so that each next series had a structure with a greater oxygen deficiency per unit cell of ideal perovskite with an ABX_3 formula unit (where A and B are cations and X is an anion): (1) ABX_3 (orthoferrites); (2) $A_5B_5X_{15-2} = 5 \times ABX_{2,6}$ (4–1–5); (3) $A_8B_8X_{24-4} = 8 \times ABX_{2,5}$ (8–8–20); (4) $A_3B_3X_{9-2} = 3 \times ABX_{2,3}$ (1–2–3).

After analysis of the Mössbauer data inside each group [6–8], we combined the results of measurements for all samples. This joint consideration was based on the quadrupole splitting (K) and isomer shift (d) observed at room temperature. These parameters were plotted in the form of a K–d diagram (see figure). As can be seen, the experimental points in this diagram form groups, so that the K–d plane appears to be subdivided into several parts. For convenience, dashed lines in the figure show this subdivision into regions corresponding to a certain ion type (charge) and coordination.

An analysis of the diagram presented in the figure leads to the following conclusions.

(i) The magnetic ordering of iron cations (at room temperature) in all oxides with perovskitelike structures arises only in octahedral positions. This can be explained by the fact that an increase in the oxygen deficiency leads to rupture of the Fe–O–Fe chains mediating in the exchange interaction.

1063-7850/05/3101-0025$26.00 © 2005 Pleiades Publishing, Inc.

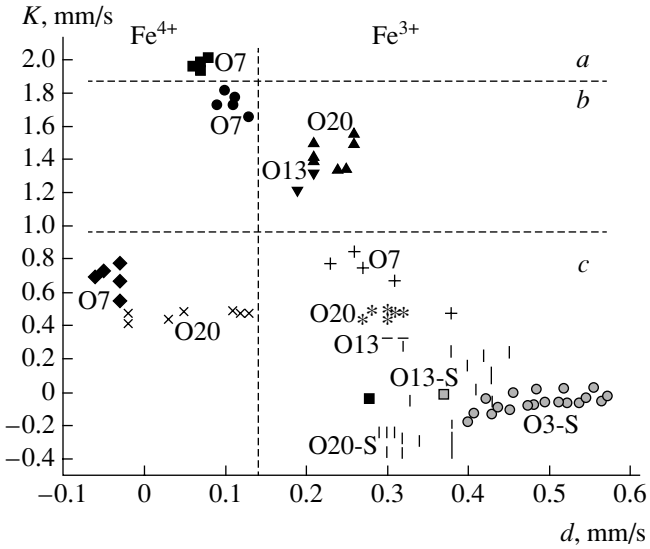

Plot of the quadrupole splitting K versus isomer shift d. Experimental points exhibit grouping with respect to the type of oxygen coordination of iron ions (*a*, square; *b*, pyramid; *c*, octahedron), structural symmetry (O7, 1–2–3; O20, 8–8–20; O13, 4–1–5; O3, orthoferrites), and room-temperature magnetic ordering (S).

(ii) In orthoferrites and 4–1–5 oxides, iron occurs only in the form of Fe^{3+} ions, while in oxygen-deficient compounds of the 8–8–20 and 1–2–3 types, iron ions also occur in a mixed $Fe^{3+} + Fe^{4+}$ valence state. As the deficiency of structural anions increases, the relative content of Fe^{4+} ions grows.

(iii) In compounds of the 8–8–20 and 4–1–5 types, iron (irrespective of the concentration) partly occupies pyramidal positions in addition to the octahedral positions (even in cases when all iron can, theoretically, be arranged in the octahedral positions). In oxides of the 1–2–3 type, iron substitutes for copper only in Cu(1) positions and adopts various oxygen coordinations (flat square, square pyramid, octahedron).

Thus, iron atoms in the perovskitelike structures in most cases occupy octahedral positions, which are followed (in the order of decreasing "occupancy") by square pyramids and planar squares. This behavior is explained (i) by the tendency of iron ions to adopt octahedral coordination [9] and (ii) by the fact that, in oxygen-deficient structures, the first two coordinations are achieved not only by directly occupying these positions, but also as a result of attracting additional oxygen to the environment.

(iv) An increase in the oxygen deficiency leads to a decrease in the symmetry of structural polyhedra, whereby orthoferrite structures (with the most symmetric polyhedra) are followed by compounds of the 4–1–5, 8–8–20, and 1–2–3 types.

Acknowledgments. This study was supported by the NIOKR-RT Foundation (project no. 06-6.1-142), the US Civilian Research and Development Foundation for the Independent States of the Former Soviet Union (CRDF grant no. REC-007), and the Presidential Program of Support for Leading Scientific Schools in Russia (project no. NSh-1708.2003.2).

REFERENCES

1. W. T. Fu, O. Xu, A. A. Verheijen, *et al.*, Solid State Commun. **73**, 291 (1990).
2. T. I. Chupakhina, G. V. Bazuev, and N. A. Kirsanov, Zh. Neorg. Khim. **46**, 204 (2001).
3. G. V. Bazuev, N. V. Lukin, N. A. Kirsanov, *et al.*, Sverkhprovodimost **6**, 1663 (1993).
4. G. V. Bazuev, N. V. Lukin, N. V. Krasil'nikov, *et al.*, Zh. Neorg. Khim. **44**, 341 (1999).
5. K. S. Aleksandrov and B. V. Beznosikov, Kristallografiya **42**, 613 (1997) [Crystallogr. Rep. **42**, 556 (1997)].
6. Sh. Sh. Bashkirov, A. A. Valiullin, L. D. Zaripova, *et al.*, Izv. Ross. Akad. Nauk, Ser. Fiz. **65**, 962 (2001).
7. Sh. Sh. Bashkirov, A. A. Valiullin, L. D. Zaripova, *et al.*, in *Anniversary Collection of Selected Works of the Academy of Sciences of Tatarstan Republic* (Foliant, Kazan, 2002), pp. 51–59.
8. Sh. Sh. Bashkirov, L. D. Zaripova, T. I. Chupakhina, *et al.*, in *Proceedings of the 5th All-Russia Scientific Conference "Oxides: Physicochemical Properties," Ekaterinburg, 2000*, pp. 82–85.
9. R. Genouel, C. Michel, N. Nguyen, *et al.*, J. Solid State Chem. **115**, 469 (1995).

Translated by P. Pozdeev

Technical Physics Letters, Vol. 31, No. 1, 2005, pp. 27–32. Translated from Pis'ma v Zhurnal Tekhnicheskoĭ Fiziki, Vol. 31, No. 1, 2005, pp. 54–66.

Acoustostimulated Expansion of the Short-Wavelength Sensitivity Range of AlGaAs/GaAs Solar Cells

E. B. Zaveryukhina[a,*], N. N. Zaveryukhina[b], L. N. Lezilova[b], B. N. Zaveryukhin[b,], V. V. Volodarskiĭ[c], and R. A. Muminov[b]**

[a] *National University of Uzbekistan, Tashkent, Uzbekistan*

[b] *Physical Engineering Institute, "Solar Physics" Research and Production Corporation, Academy of Sciences of the Republic of Uzbekistan, Tashkent, Uzbekistan*

[c] *PSP Company, Obninsk, Kaluga oblast, Russia*

*e-mail: * k4685@rambler.ru; ** boris.zav@sarkor.uz; oybtm@physic.uzsci.net*

Received May 25, 2004; in final form, August 10, 2004

Abstract—The effect of ultrasonic waves on the spectral sensitivity of solar energy converters based on AlGaAs/GaAs heterostructures has been studied. Ultrasonic treatment of a zinc-doped graded-gap $Al_xGa_{1-x}As$ film leads to the formation of a surface layer sensitive to electromagnetic radiation in the wavelength range $\lambda < 0.551$ μm. It is established that this layer is formed as a result of the acoustostimulated inward diffusion of zinc from the surface to the bulk of the graded-gap layer. The observed expansion of the short-wavelength sensitivity range and an increase in the efficiency of nonequilibrium charge carrier collection in AlGaAs/GaAs solar cells are due to improvement of the crystal defect structure and the dopant redistribution under the action of ultrasound. © *2005 Pleiades Publishing, Inc.*

Introduction. The task of controlled variation of the physical properties of semiconductor materials under the action of external factors is an important problem in the physics of semiconductors. As is well known, one such factor is ultrasonic radiation: propagating in a semiconductor crystal, ultrasonic waves change its properties, in particular, the optical characteristics [1]. In the context of solving the above task, it is expedient to continue investigations of the effect of ultrasonic waves on the characteristics of semiconductor devices.

This paper presents the results of experimental investigations of the influence of ultrasonic waves on the spectral characteristics of solar cells based on AlGaAs/GaAs heterostructures. The study was a logical continuation of our previous research [1], which showed that an exposure to ultrasonic radiation leads to a change, depending on the ultrasonic treatment (UST) parameters, in the spectral coefficient of reflection of silicon and gallium arsenide crystals, the base materials of modern semiconductor photoelectronics. To the best of our knowledge, no systematic data on the effect of ultrasonic waves on the working characteristics of GaAs-based solar cells are available. Some published results showed evidence of the positive character of changes in the characteristics of silicon-based solar cells under the action of ultrasonic waves [2, 3].

Gallium arsenide possesses a greater optical absorption coefficient, a wider bandgap, and higher mobilities of charge carriers as compared to the analogous characteristics for silicon, which accounts for the higher efficiency η of solar cells based on the former material. The theoretical limit of η for GaAs solar cells under standard AM1 solar illumination conditions exceeds 30%. The most widely used system in GaAs-based solar cells operating in an AM1 regime with $\eta \geq 17\%$ is a heterostructure of the n^+-GaAs–n-GaAs–p-GaAs–p-$Al_xGa_{1-x}As$ type fabricated by means of a relatively simple liquid phase epitaxy (LPE) method [4, 5].

Experimental. The experiments were performed with AlGaAs/GaAs-based solar cells fabricated using the following technology. The substrates for LPE-grown heterostructures were [111]-oriented single crystal n-GaAs wafers with a thickness of d = 350–400 μm, doped with tin (n^+-GaAs(Sn)) to $N \sim (1.5–3) \times 10^{18}$ cm^{-3}. The sequential epitaxial layers were n-GaAs(Sn) with a thickness of d = 12–14 μm and an electron density of $N_e = (2–5) \times 10^{17}$ cm^{-3}; diffusion-doped p-GaAs:Zn with a thickness of 0.8–1.5 μm and a hole concentration $p = 6 \times 10^{17}–4 \times 10^{18}$ cm^{-3}, obtained by zinc diffusion from the liquid phase; and the frontal p-$Al_xGa_{1-x}As$ with x = 0.3–0.8 and a thickness of l = 0.7–4.5 μm, doped with zinc to $(1–3) \times 10^{18}$ cm^{-3}. Then, an antireflection coating was formed by anodic oxidation of the uppermost $Al_xGa_{1-x}As$ layer, and ohmic contacts of a certain configuration were formed using the conven-

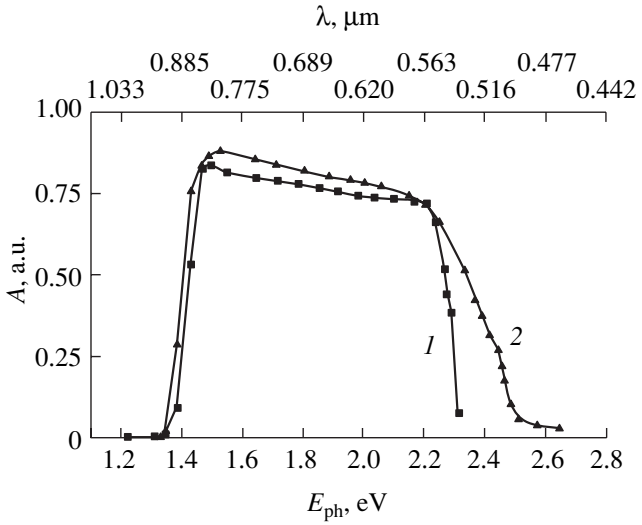

Fig. 1. The spectral characteristic of the photosensitivity A of an AlGaAs/GaAs solar cell (sample 13) measured (*1*) before and (*2*) after the UST at f = 25 MHz and P = 0.25 W/cm^2 for t = 65 min (T = 293 K).

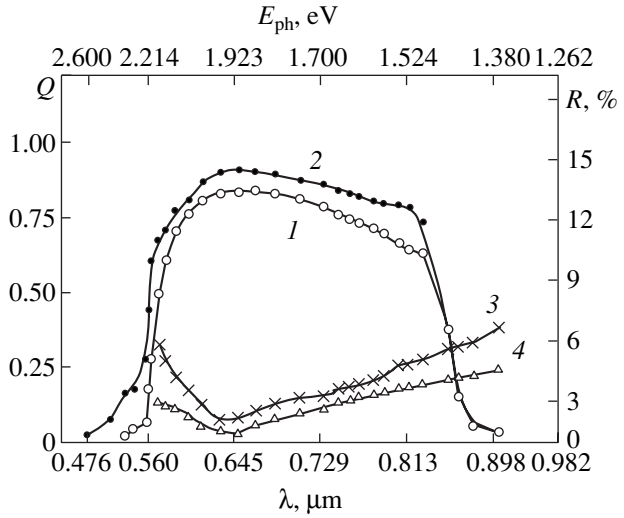

Fig. 2. The spectral dependence of the (*1*, *2*) charge carrier collection efficiency Q and (*3*, *4*) reflection coefficient R of an AlGaAs/GaAs solar cell (sample 13) measured (*1*, *3*) before and (*2*, *4*) after the UST at f = 25 MHz and P = 0.25 W/cm^2 for t = 65 min (T = 293 K).

tional photolithographic technique and electrochemical deposition of silver and nickel. The area M of the entrance window of the AlGaAs/GaAs solar cells varied from 0.25 to 2.25 cm^2.

The characteristics of the AlGaAs/GaAs solar cells were measured using a source imitating solar radiation and operating under conditions corresponding to AM1.5 illumination at a radiant flux power S = 850 W/m^2. The experimental procedure consisted in determining the photoelectric characteristics of the AlGaAs/GaAs solar cells before and after the room-temperature UST with monochromatic ultrasonic waves in various regimes. The monochromatic electromagnetic radiation was incident onto the outer surface of a wide-bandgap p-$Al_xGa_{1-x}As$ layer from the side of the entrance window. The AlGaAs/GaAs solar cells were exposed to longitudinal ultrasonic waves in the range of frequencies f = 0.8–25 MHz and power densities P = 0.1–5 W/cm^2 in the entrance window, at a variable exposure time of t = 15–60 min. The ultrasonic waves were transferred from a piezoelectric transducer (driven by a generator) to the AlGaAs/GaAs receiver via a liquid medium.

Parameters of an AlGaAs/GaAs solar cell (sample 13 with M = 0.25 cm^2, measured at T = 293 K, AM1.5, S = 850 W/m^2) before and after UST (f = 25 MHz, P = 0.25 W/cm^2, t = 65 min, T = 293 K)

Parameter	Before UST	After UST
Short-circuit current density I_{SC}, mA/cm^2	20.84	22
Open-circuit voltage V_{OC}, V	0.942	0.946
Filling factor *ff*	0.75	0.75
Efficiency η, %	17.32	18.36
Spectral sensitivity range λ, μm	0.534–900	0.466–0.900

Results and discussion. We studied a total of 30 AlGaAs/GaAs solar cells before and after the UST in various regimes characterized by the parameters *f*, *P*, and *t*. The most significant improvement in the photoelectric characteristics was observed for AlGaAs/GaAs solar cells irradiated with ultrasonic waves at $f \geq 15$ MHz and $P < 1$ W/cm^2 for $t > 45$ min. Figures 1 and 2 and the table present the results of our measurements of the spectral and functional characteristics for sample 13, which is a typical representative of the given series of AlGaAs/GaAs solar cells, with an p-$Al_xGa_{1-x}As$ (x = 0.4) layer thickness of l = 4 μm measured before and after the UST at f = 25 MHz and P = 0.25 W/cm^2 for t = 65 min.

Let us consider, in some detail, the data presented in the table and Figs. 1 and 2. The spectral characteristic (photoresponse A versus wavelength λ) of the solar cell measured before the UST exhibits a maximum at λ ≈ 0.775 μm (corresponding to the photon energy E_{ph} = 1.6 eV) followed by a smooth decrease in the photoresponse A in the wavelength interval λ = 0.563–0.775 μm and a sharp decrease in A above this interval at λ = 0.775–0.892 μm (E_{ph} = 1.6–1.39 eV). The occurrence of a maximum in the region of photon energies above the GaAs bandgap width is indicative of the fact that the p–n junction is situated within the AlGaAs layer of the heterostructure. The drop in A in the wave-

length range at $\lambda > 0.775$ μm is mostly caused by a decrease in the hole diffusion length L_p determined by the presence of various defects. As is known [7, 8], graded-gap solid solutions feature built-in electric fields favoring more complete and fast charge collection on the electric contacts. Deviation of the shape of the spectral characteristic (photoresponse A) from the rectangular profile, which is manifested by the A value gradually decreasing in the interval $\lambda = 0.775$–0.563 μm, shows that the existing electric field gradient in the p-$Al_xGa_{1-x}As$ layer cannot provide for a fast drift and complete collection of nonequilibrium electrons.

An analysis of the data on the response signal amplitude k of the AlGaAs/GaAs solar cells operating as pulsed radiation receivers at $\lambda = 0.700$ μm [9, 10] revealed the presence of centers of electron trapping and recombination in the sensitive layer. This was indicated by the slow growth of the response signal amplitude according to the law $k(V) \sim V^n$ with $n = 1/2 < 1$ (V is the bias voltage). The presence of these electrically active centers decreases the electric field strength and increases the probability of carrier trapping in the graded-gap layer. Indeed, it was demonstrated [11] that traps present in the sensitive layer of receivers lead to the formation of regions where the electric field is very small or even absent. This results in a strong trapping of nonequilibrium carriers, leading to polarization of the receiver and, hence, to a decrease in its sensitivity and the response signal amplitude. The same factor (the presence of traps) is responsible for a decrease in the built-in electric field, the trapping of nonequilibrium carriers in the p-$Al_xGa_{1-x}As$ layer, and the observed decrease in the photoresponse amplitude A observed in our samples.

One possible reason for an increase in the short-circuit current I_{SC} observed upon the UST is the ultrasound-induced suppression (neutralization) of the centers of electron trapping and recombination in the sensitive layer, that is, in the region of effective carrier photogeneration [12]. This is confirmed by an increase in the signal amplitude in the wavelength interval $\lambda = 0.775$–0.563 μm and by the appearance of a photoresponse in the interval $\lambda = 0.551$–0.466 μm. This acoustostimulated expansion of the short-wavelength sensitivity range is clearly illustrated in Fig. 1 (curve *2*). Expansion of the photoresponse toward the long-wavelength region ($\lambda > 0.849$ μm) is much less significant. The acoustostimulated photoresponse at $\lambda > 0.849$ μm due to neutralization of the trapping and recombination centers was reported for a cascade narrowband GaAs photoconverter [13].

The usual way to expand the short-wavelength sensitivity range of $Al_xGa_{1-x}As$/GaAs solar cells is through (a) an increase in the x component fraction in the $Al_xGa_{1-x}As$ solid solution and (b) a decrease in the p-$Al_xGa_{1-x}As$ layer [6]. However, the action of ultrasonic waves on the AlGaAs/GaAs solar cells under the conditions used in our experiments can change neither the x value nor the thickness of the p-$Al_xGa_{1-x}As$ epilayer. For this reason, we believe that the acoustostimulated photoresponse in the short-wavelength spectral range ($\lambda < 0.551$ μm) is caused, for the most part, by three factors.

Factor 1: the formation of photosensitive subsurface $Al_xGa_{1-x}As$ layers with an increased resistivity ρ as compared to that in the bulk of $Al_xGa_{1-x}As$ as a result of the acoustostimulated inward diffusion of zinc from the surface to bulk of the graded-gap layer. The possibility of this phenomenon is justified by the following considerations and is confirmed by the results of experiments with zinc diffusion in the ultrasonic field presented below.

It is known that, as the photon energy E_{ph} increases, the region of nonequilibrium carrier generation shifts toward the surface of the narrow-bandgap p-$Al_xGa_{1-x}As$ layer in the entrance window. The p-$Al_xGa_{1-x}As$ film in our solar cells, as well as in the semiconductor detectors of nuclear radiation [14], contains "dead" layers, insensitive with respect to the ionizing radiation. The presence of such layers poses problems even for the technology of nuclear radiation detectors, which (being intended for the detection of radiation that has a much lower intensity than solar radiation) are more precise devices than the solar cells. Since the principles of AlGaAs/GaAs solar cells are generally the same as those underlying the operation of nuclear radiation detectors (generation, drift, and collection of nonequilibrium carriers on electric contacts of the detector), the solar cells can also be considered as detectors of electromagnetic radiation, with the entire set of drawbacks inherent in these devices (loss of generated carriers, crystal structure defects, "dead" layers, etc.).

Our analysis showed that the absence of photoresponse (a lack of photosensitivity) observed for the $Al_xGa_{1-x}As$ solar cells in the range $\lambda < 0.551$ μm (Fig. 1, curve *1*) is related to the high conductivity σ of the subsurface region in the p-$Al_xGa_{1-x}As$ layer on the side of the entrance window exposed to the incident electromagnetic radiation. It was established that the zinc concentration N_{Zn} measured using a JSM 5910LV electron microprobe (JEOL, Japan) in a subsurface region with a thickness of $L \leq 01$–0.15 μm was 2–4 times greater than that in the bulk of the p-$Al_xGa_{1-x}As$ layer. This gradient of N_{Zn} arises in the course of fabrication of the AlGaAs/GaAs solar cells and results in the formation of a Zn-saturated subsurface region with a submicron thickness, which is not sensitive ("dead" layer) with respect to electromagnetic radiation at $\lambda < 0.551$ μm.

The appearance of the photoresponse in this spectral range can be provided by decreasing σ of this nonphotosensitive layer. In the technology of nuclear radiation

detectors, the task of creating a high-ohmic subsurface region is usually solved by incorporating lithium atoms into *p*-Si [14]. A decrease in conductivity of the subsurface region leads to the buildup of an additional (graded-gap) electric field E_v of the same sign as in the entire *p*-$Al_xGa_{1-x}As$ layer. The appearance of this additional graded-gap layer with the electric field E_v implies an expansion of the spectrally sensitive region of the AlGaAs/GaAs solar cells toward the surface, which must provide for the photoresponse to photons with $E_{ph} > 2.25$ eV ($\lambda < 0.551$ μm). In fact, we observed the appearance of such a photoresponse in AlGaAs/GaAs solar cells upon the UST (Fig. 1, curve *2*), which provided evidence for the acoustostimulated formation of photosensitive *p*-$Al_xGa_{1-x}As$ layers (or the disappearance of "dead" layers) near the surface of the entrance window.

The results of experimental measurements of the zinc concentration in samples with *p*-$Al_xGa_{1-x}As$ layer thicknesses up to 50 μm, which had the same initial compositions and N_{Zn} values as those in our AlGaAs/GaAs solar cells, showed that the UST for t = 240–360 min and above led to a three- to fivefold decrease in N_{Zn} in the subsurface layers. In these experiments, the dopant concentration was determined using electron-probe microanalysis with layer-by-layer ion-beam etching [1]. The UST parameters f and P in these experiments were the same as those used for the activation of the AlGaAs/GaAs solar cells. Therefore, the appearance of the photosensitive subsurface *p*-$Al_xGa_{1-x}As$ layers is related to the acoustostimulated inward diffusion of zinc from the surface to the bulk of the $Al_xGa_{1-x}As$ layer. Theoretical investigation into the effect of ultrasonic waves on the process of impurity diffusion in semiconductors was reported in [15].

Factor 2: the acoustostimulated decomposition of impurity clusters. The existence of this phenomenon is confirmed by the character of variation of the spectral dependence of the efficiency $Q(\lambda)$ of the nonequilibrium charge carrier collection measured in the wavelength interval λ = 0.448–0.982 μm. Figure 2 reveals the effect of UST on $Q(\lambda)$ in the region $\lambda < 0.532$ μm As can be seen from these data, the UST increases the spectral sensitivity range from λ = 0.532 μm (curve *1*) to λ = 0.476 μm (curve *2*) and provides for a general increase in the magnitude of $Q(\lambda)$. This result indicates that, in addition to the acoustostimulated diffusion of zinc, the UST produces annealing of the recombination centers [16] and induces decomposition of the impurity clusters similar to that observed in [17]. Both our data [18] and the results reported in [17] show that the UST leads to an increase in the mobility μ of charge carriers. The growth of the drift velocity due to the increase in μ decreases the probability of carrier trapping and, hence, increases the efficiency of charge carrier collection.

In this context, it should be noted that the influence of ultrasound on the spectrum of local states in GaAs-based heterostructures was studied in [19], where it was established that the UST leads to a spatial and chemical ordering of the near-contact regions in these structures. The results concerning the ultrasound-induced reconstruction of the defect subsystem of a crystal [19] generally agree with our data, which also show evidence of a certain improvement in the crystal defect structure in the subsurface regions of solar cells based on A_3B_5 compounds. It is this modification of the subsurface regions under the action of ultrasonic waves that accounts for the observed expansion of the spectral sensitivity range toward shorter wavelengths and an increase in the efficiency of nonequilibrium charge carrier collection.

Factor 3: a change in the character of the electromagnetic radiation reflection from the *p*-$Al_xGa_{1-x}As$ layer upon UST. It has previously been established that an UST leads to a rearrangement of the system of photoelectrically active defects in semiconductors [20] and modifies their optical properties [1]. In the present investigation, we also studied the effect of UST on the optical reflection coefficient R of the *p*-$Al_xGa_{1-x}As$ layer in the series of samples where this layer had the same thickness and composition as those in our AlGaAs/GaAs solar cells. The R value was measured as described in [1]. This experiment showed that the UST at f = 20 MHz and P = 0.25 W/cm^2 for t = 60 min and above led to a decrease in the coefficient R, as can be seen from a comparison of the reflectance curves measured before (Fig. 2, curve *3*) and after the UST (curve *4*). The observed decrease in R can be explained using the notions about the acoustostimulated diffusion of impurities [1, 15]. The acoustostimulated inward diffusion of zinc from the surface to the bulk of the *p*-$Al_xGa_{1-x}As$ layer in the entrance window makes the surface less "metallized," which decreases the reflection coefficient.

The observed shift in the position of the minimum in the $R(\lambda)$ from λ = 0.630 μm toward longer wavelengths (λ = 0.645 μm) after the UST is also indicative of a decrease in the zinc concentration at the sample surface. The UST-induced changes in the composition and structure of the subsurface region in the entrance window also naturally modify the other optical characteristics [7, 20], including the coefficients of optical absorption, transmission, and refraction. A decrease in the reflection coefficient and the corresponding increase in absorption must also be accompanied by the appearance and enhancement of the photoresponse in a certain interval of wavelengths, which was actually observed in experiment. Exact determination of the optical losses and their separation into reflection and absorption types are outside of the scope of this study.

The observed increase in the photoresponse amplitude A in the wavelength interval λ = 0.775–0.563 μm

(Fig. 1, curve *2*) and the growth in the charge carrier collection coefficient Q (Fig. 2, curve *2*) upon UST is related to neutralization of the trapping and recombination centers in the p-$Al_xGa_{1-x}As$ layer. An analysis of the variation in the A and Q values shows evidence in favor of the acoustostimulated transformation of defects, analogous to that previously reported in [12–20], which leads to the neutralization of traps and smoothening of the potential relief of the electric field in the volume of the photosensitive region of a solar cell. This naturally results in a more complete collection of nonequilibrium carriers on the electric contacts of the device, which is confirmed by the passage from $n < 1$ to $n > 1$ in the power dependence of the response, $A \sim V^n$, after the UST of solar cells.

It is necessary to mention the possibility of an acoustic-wave-induced variation of the properties of the anodic oxide, which may also influence the characteristics of photosensitive structures. Indeed there are data suggesting that ultrasound may change the properties of oxides; in particular, it was demonstrated [21] that the UST of a metal–insulator–semiconductor structure decreases the built-in charge in the insulator and reduces the charge of the surface states. Therefore, the coefficients of the reflection R and refraction Ψ of an electromagnetic wave propagating through such an ultrasound-modified insulator layer will differ from the corresponding values prior to the treatment. We also checked for the possibility of the acoustostimulated variation of R and Ψ and the electrical parameters of the anodic oxide. The results of these experiments showed that the characteristics of anodic oxide change upon the UST at the frequencies $f > 50$ MHz, which were not used for the UST of our solar cells. Based on these data, we believe that the influence of the acoustostimulated changes in the optical properties of anodic oxide in our experiments with solar cells was either small or absent.

Therefore, improvement of the functional characteristics of AlGaAs/GaAs solar cells as a result of the UST (see table) is related to residual phenomena such as the redistribution of impurities, the formation of electrically inactive defects, etc.

Conclusions. (1) Irradiation of graded-gap zinc-doped p-$Al_xGa_{1-x}As$ solid solutions with ultrasonic waves at a power density of $P < 1$ W/cm^2 and a frequency of $f > 15$ MHz leads to a decrease in the zinc concentration in the subsurface layer. This result is due to the acoustostimulated inward diffusion of zinc from the surface to the bulk of the graded-gap layer.

(2) The resulting zinc-depleted layer becomes sensitive to electromagnetic radiation with wavelengths $\lambda <$ 0.551 eV as a result of the modified character of the reflection and absorption of the incident radiation. The electric field in the modified graded-gap layer stimulates the effective collection of the nonequilibrium charge carriers generated by photons in this layer, which provides for the appearance of the photoresponse to photons with the energies $E_{ph} > 2.25$ eV.

(3) Irradiation of AlGaAs/GaAs solar cells with ultrasonic waves at $f \geq 15$ MHz and $P \leq 1$ W/cm^2 leads to an increase in the efficiency of collection of the nonequilibrium charge carriers, which is explained by an improved crystal defect structure in the subsurface layer, and expands the short-wavelength sensitivity range to $\lambda = 0.476$ μm.

(4) Although the results of the ultrasound-induced improvement of the characteristics of AlGaAs/GaAs solar cells are not on a record level, the results of our investigation show the high potential of the development of acoustic methods for increasing the efficiency of solar cells based on various semiconductor materials.

Acknowledgments. The authors are grateful to N.N. Chernikov (Moscow) for his help in these investigations.

REFERENCES

1. B. N. Zaveryukhin, N. N. Zaveryukhina, and O. M. Tursunkulov, Pis'ma Zh. Tekh. Fiz. **28** (18), 1 (2002) [Tech. Phys. Lett. **28**, 752 (2002)].
2. A. Iskanderov, V. D. Krevchik, R. A. Muminov, and I. U. Shadybekov, Geliotekhnika, No. 6, 19 (1988).
3. A. Iskanderov, V. D. Krevchik, R. A. Muminov, and I. U. Shadybekov, Geliotekhnika, No. 4, 25 (1989).
4. V. M. Andreev, L. M. Dolginov, and D. N. Tret'yakov, in *Liquid-Phase Epitaxy in Semiconductor Device Technology* (Sov. Radio, Moscow, 1975) [in Russian].
5. B. N. Zaveryukhin, A. Iskanderov, Kh. Kh. Ismailov, *et al.*, Geliotekhnika, No. 1, 11 (1987).
6. V. M. Andreev, T. M. Golovner, M. B. Kagan, *et al.*, Fiz. Tekh. Poluprovodn. (Leningrad) **7**, 2289 (1973).
7. A. N. Imenkov, N. Nazarov, B. S. Suleimanov, *et al.*, Fiz. Tekh. Poluprovodn. (Leningrad) **12**, 2377 (1978) [Sov. Phys. Semicond. **12**, 1413 (1978)].
8. Zh. I. Alferov, V. M. Andreev, Yu. M. Zadiranov, *et al.*, Pis'ma Zh. Tekh. Fiz. **4**, 1128 (1978) [Sov. Tech. Phys. Lett. **4**, 149 (1978)].
9. V. K. Eremin, Candidate's Dissertation (Leningrad, 1978).
10. B. N. Zaveryukhin, N. N. Zaveryukhina, R. A. Muminov, and O. M. Tursunkulov, Pis'ma Zh. Tekh. Fiz. **28** (5), 75 (2002) [Tech. Phys. Lett. **28**, 207 (2002)].
11. V. K. Eremin, N. B. Strokan, and N. I. Tisnek, Fiz. Tekh. Poluprovodn. (Leningrad) **9**, 530 (1975) [Sov. Phys. Semicond. **9**, 347 (1975)].
12. B. N. Zaveryukhin, V. D. Krevchik, R. A. Muminov, and A. Sh. Shamigdiev, Fiz. Tekh. Poluprovodn. (Leningrad) **20**, 525 (1986) [Sov. Phys. Semicond. **20**, 330 (1986)].
13. B. N. Zaveryukhin, N. N. Zaveryukhina, L. N. Lezilova, and E. B. Zaveryukhina, in *Proceedings of the 3rd World Conference on Photovoltaic Energy Conversion and the*

18th European PV Solar Energy Conference (Osaka, 2003), Vol. 3P-B5-38, p. 74.

14. G. Dearnaley and D. C. Northrop, *Semiconductor Counters for Nuclear Radiations* (Wiley, New York, 1963).
15. V. D. Krevchik, R. A. Muminov, and A. Ya. Yafasov, Phys. Status Solidi A **63**, K159 (1981).
16. A. A. Alaev, V. M. Andreev, B. N. Zaveryukhin, *et al.*, in *Photovoltaic Phenomena in Semiconductors: Proceedings of the 2nd Scientific Conference on Physics and Chemistry of Semiconductors* (Ashkhabad, 1991), pp. 221–222.
17. P. I. Baranskiĭ, A. E. Belyaev, S. M. Komirenko, and N. V. Shevchenko, Fiz. Tverd. Tela (Leningrad) **32**, 2159 (1990) [Sov. Phys. Solid State **32**, 1257 (1990)].
18. B. N. Zaveryukhin, R. A. Muminov, N. N. Zaveryukhina, *et al.*, in *Proceedings of the Conference on Photoelectric Phenomena in Semiconductors* (Tashkent, 2004), pp. 2–4.
19. I. B. Ermolovich, V. V. Milenin, R. V. Konakova, and L. N. Primenko, Fiz. Tekh. Poluprovodn. (St. Petersburg) **31**, 503 (1997) [Semiconductors **31**, 427 (1997)].
20. V. L. Gromashevskiĭ, V. V. Dyakin, *et al.*, Ukr. Fiz. Zh. **9**, 550 (1984).
21. P. B. Parchinskiĭ, S. I. Vlasov, R. A. Muminov, *et al.*, Pis'ma Zh. Tekh. Fiz. **26** (10), 45 (2000) [Tech. Phys. Lett. **26**, 420 (2000)].

Translated by P. Pozdeev

Technical Physics Letters, Vol. 31, No. 1, 2005, pp. 33–35. Translated from Pis'ma v Zhurnal Tekhnicheskoĭ Fiziki, Vol. 31, No. 1, 2005, pp. 67–72.

Self-Reflection in a Plane-Parallel Semiconductor Plate Caused by Two-Photon Excitation of Biexcitons

L. Yu. Nad'kin and P. I. Khadzhi

Trans-Dniester State University, MD 3300 Tiraspol-3, Moldova

e-mail: tdsu4@idknet.com

Received April 7, 2004

Abstract—Taking into account two-photon excitation of biexcitons leads to an increase in the multistable transmission of a thin plane-parallel semiconductor plate, which is a manifestation of the phenomenon of self-reflection of a propagating wave. © *2005 Pleiades Publishing, Inc.*

It was demonstrated [1–4] that a semi-infinite absorbing medium modeled by a system of two-level atoms can feature the phenomenon of self-reflection. By this we imply the appearance of a backward wave in an optically homogeneous semi-infinite medium, which is the wave reflected from a spatially inhomogeneous nonlinear refractive index profile induced by the field of the forward wave. Previously, we showed [5–10] that the phenomenon of self-reflection also takes place in a system of excitons and biexcitons in semiconductors, provided that the exciton–photon interaction, exciton–biexciton conversion, and the single- and double-pulse two-photon excitation of biexcitons from the ground state of the semiconductor crystal are taken into account. It was proved that self-reflection is a consequence of the optical Stark effect, which leads to renormalization of the energy spectrum of the system at high levels of laser excitation.

It should be noted that all features of the self-reflection manifestations were studied in semi-infinite crystals [1–10]. Evidently, this phenomenon may also take place in a plane-parallel semiconductor plate of a finite thickness at the normal incidence of laser radiation on one of the plate faces. However, one should take into account that the phenomenon of self-reflection in this case is significantly complicated by the presence of a Fresnel reflection from the rear face of the plate. We believe that it is impossible to separate the contribution of self-reflection and that of the Fresnel reflection from the rear face to the total multistable reflection. However, we may note that, if the length of the domain of high-density elementary excitations is smaller than the plate thickness, the plate essentially represents two sequential Fabry–Perot resonators induced by the propagating wave field. The transmission (reflection) function of these resonators has a rather complicated character. A change in the excitation level results in the thickness of one of these Fabry–Perot resonators (or the corresponding domains) decreasing, whereas the other resonator (domain) thickness increases. At a high excitation level, the entire plate becomes the domain of high-density excitations and the role of self-reflection in the total multistable reflection of the plate decreases. By the same token, the role of self-reflection is also negligibly small at low excitation levels, whereby the field amplitude in the medium exhibits exponential variation.

We have studied the contribution of self-reflection to the transmission (reflection) function of a plane-parallel semiconductor plate as dependent on the excitation level and the plate thickness (L), making allowance for the single-pulse two-photon excitation of biexcitons from the ground state of the crystal. Previously [7], it was shown that this process gives rise to self-reflection in a semi-infinite medium. The permittivity ε of the semiconductor in such a case is [7]

$$\varepsilon = \varepsilon_1 + i\varepsilon_2 + \frac{\alpha_0}{\delta^2 + 1}(-\delta + i)|E|^2, \qquad (1)$$

where ε_1 and ε_2 are the real and imaginary components of permittivity in the zero-field limit; E is the propagating wave field amplitude; $\delta = \Delta\gamma/\gamma$; γ is the attenuation constant, $\Delta = \omega - \omega_0$ is the resonance detuning between the frequency of the propagating radiation (ω) and the transition frequency (ω_0); and α_0 is the Kerr constant.

Consider an electromagnetic wave with the electric field amplitude E_i and the frequency ω incident along the normal onto the front face of a plane-parallel semiconductor plate. The spatial distribution of the wave field intensity in a stationary regime is determined by a solution of the wave equation

$$\frac{d^2E}{dz^2} + \left(\varepsilon_1 + i\varepsilon_2 + \frac{\alpha_0}{\delta^2 + 1}(-\delta + i)|E|^2\right)E = 0, \qquad (2)$$

where $z = \dfrac{\omega}{c}x$, c is the speed of light in vacuum, and x is the coordinate measured in the wave propagation direction. The boundary conditions at the points $x = 0$

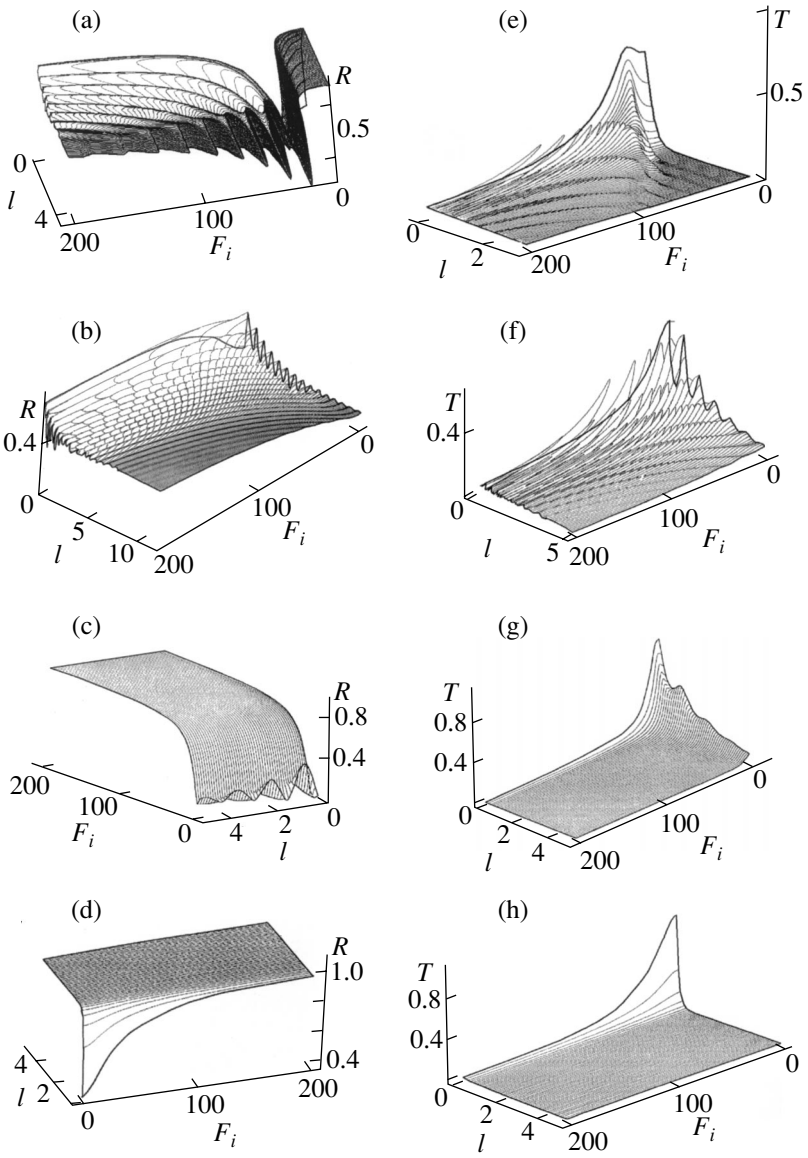

Fig. 1. Dependence of the (a–d) reflection coefficient R and (e–h) transmission coefficient T on the normalized plate thickness l and the normalized incident radiation amplitude F_i calculated for $\varepsilon_2 = 1.5$, $\alpha_0 = 1$ and various pairs of the parameters (ε_1, δ): (a, e) –15, –15; (b, f) –15, 15; (c, g) 15, 15; (d, h) 15, –15.

and $x = L$ reflect the continuity of tangential components of the electric and magnetic fields:

$$E_i + E_r = E|_{z=0}; \quad E_i - E_r = -i\frac{\partial E}{\partial z}\bigg|_{z=0}, \qquad (3)$$

$$E_t = E|_{z=L}, \quad E_t = -i\frac{\partial E}{\partial z}\bigg|_{z=L}, \qquad (4)$$

where E_i, E_r, and E_t are the amplitudes of the incident, reflected, and transmitted waves, respectively. Below, for the sake of simplicity, we use the normalized field amplitudes defined as

$$F(z) = E(z)\sqrt{\alpha_0}, \quad F_{i,r,t} = E_{i,r,t}\sqrt{\alpha_0}. \qquad (5)$$

Since the exact analytical solutions of Eq. (2) are not available, we have used a numerical method successfully employed previously [5–10].

Below, we consider the results of numerical calculations for the coefficients of reflection $R = |F_r/F_i|^2$ and transmission $T = |F_t/F_i|^2$ as functions of the incident radiation amplitude (F_i) and the plate thickness (l). In these calculations, the minimum normalized plate thickness $l = 2\pi\frac{L}{\lambda}$ was set equal to 0.1.

The diagrams of the reflection coefficient $R(l, F_i)$ and transmission coefficient $T(l, F_i)$ are presented in Figs. 1a–1d and 1e–1h, respectively. Similarly to the case of a semi-infinite medium [7], there are four

regimes of radiation propagation in this medium that can be distinguished as being dependent on the signs of the resonance detuning δ and the real permittivity component ε_1.

For $\delta < 0$ and $\varepsilon_1 < 0$, the system is characterized by nontransmission of the propagating wave field with a small amplitude $F^2 < \varepsilon_1/(\alpha_0\delta)$ but exhibits transmission for $F^2 > \varepsilon_1/(\alpha_0\delta)$. For small plate thicknesses, an increase in the incident wave amplitude is initially accompanied by a slow decrease in the reflection coefficient. After passing through a minimum at a certain value of F_i, the reflection coefficient starts to increase and, eventually, tends to unity at high incident wave amplitudes. The depth of the minimum increases with the plate thickness (see Fig. 1a). The transmission coefficient slightly increases, exhibits a maximum, and then rapidly decreases and tends to zero at high incident wave amplitudes (Fig. 1e). At high incident wave amplitudes, the system features the regions of multistability, which are more pronounced for the reflection coefficient (Fig. 1a). As the plate thickness is increased, the multistability loops shift toward smaller F_i values, decrease in size, and acquire an oscillatory character. In addition, increasing plate thickness leads to the appearance of multistability loops in the region of low field amplitudes (Fig. 1a). These loops exhibit stronger self-reflection than the loops formed in stronger fields. An increase in the linear size of the plate leads to a growth in the size of the multistability loops appearing in small fields. The behavior of $T(l, F_i)$ also exhibits a similar trend but, in contrast to the reflection coefficient, the loops of multistability do not appear in small fields or large-size plates because the radiation cannot penetrate through the entire plate thickness.

In the case of $\delta < 0$ and $\varepsilon_1 > 0$, the surfaces describing $R(l, F_i)$ (Fig. 1b) and $T(l, F_i)$ (Fig. 1f) behave somewhat differently, since the permittivity corresponds to transmission for both low and high fields. A limiting transition to the case of a semi-infinite plate [7] is observed for much thicker plates, which indicates that the incident radiation penetrates to a considerable depth. For small incident wave amplitudes, the $R(l)$ and $T(l)$ functions exhibit oscillatory behavior, which is less pronounced in thicker plates. In relatively thin plates, the behavior of $R(F_i)$ and $T(F_i)$ is similar to that described above (see Figs. 1a and 1e): both functions exhibit multistability regions. However, no multistability is observed in the plates of greater size, and the system exhibits virtually constant reflection (transmission) for various incident wave intensities.

For $\delta > 0$ and $\varepsilon_1 > 0$ (Figs 1c and 1g), the R and T surfaces exhibit oscillations at small incident wave intensities, which are analogous to those observed in the preceding case (Figs. 1b and 1f). This is explained by the fact that behavior of the energy reflection and transmission coefficients in weak fields depends on the permittivity to a greater extent than on the field amplitude. As the incident pulse amplitude increases, the reflection coefficient tends to unity (and the transmission, to zero). No bistability or multistability is observed in this case. The main features in the behavior of the reflection and transmission coefficients are related to the nontransmission of the incident radiation in the medium at large field intensities.

Finally, the R and T surfaces in the case of $\delta > 0$ and $\varepsilon_1 < 0$ (Figs 1d and 1h) correspond to nontransmission for all fields. In this case, the reflection coefficient is unity almost everywhere, except for a narrow region at very small thicknesses and fields. Accordingly, the transmission coefficient is almost always negligibly small. Hence, the relation $R + T = 1$ is satisfied because the incident radiation virtually does not penetrate into the medium and the absorption is practically absent.

The above peculiarities in the behavior of the reflection and transmission coefficients as functions of the excitation intensity are related to the appearance of sharp peaks in the internal reflection coefficient inside the medium. This is indicative of the pumping-field-induced formation of a Fabry–Perot resonator. It is reflection from the edge of this resonator that accounts for the observed multistability. The obtained results show that the sharp dependence of the transmission (reflection) coefficient on the plate thickness is especially pronounced for small plate thicknesses. When the plate thickness coincides with the length of the domain of high density of biexcitons, the plate features the enhanced interference that is manifested by sharp variations in the transmission coefficient.

REFERENCES

1. L. Roso-Franko, Phys. Rev. Lett. **55**, 2149 (1985); J. Opt. Soc. Am. B **4**, 1878 (1987).
2. V. Malyshev and E. C. Jarque, J. Opt. Soc. Am. B **12**, 1868 (1995).
3. V. A. Malyshev and D. K. Kharke, Opt. Spektrosk. **82**, 630 (1997) [Opt. Spectrosc. **83**, 967 (1997)].
4. W. Forysiak, R. G. Flesch, J. V. Moloney, and E. M. Wright, Phys. Rev. Lett. **76**, 3695 (1996).
5. K. D. Lyakhomskaya and P. I. Khadzhi, Zh. Tekh. Fiz. **70**, 89 (2000) [Tech. Phys. **45**, 1457 (2000)].
6. K. D. Lyakhomskaya and P. I. Khadzhi, Kvantovaya Élektron. (Moscow) **29**, 43 (1999).
7. K. D. Lyakhomskaya, P. I. Khadzhi, and D. A. Markov, Pis'ma Zh. Tekh. Fiz. **26** (7), 18 (2000) [Tech. Phys. Lett. **26**, 276 (2000)].
8. K. D. Lyakhomskaya, L. Yu. Nad'kin, and P. I. Khadzhi, Kvantovaya Élektron. (Moscow) **31**, 67 (2001).
9. K. D. Lyakhomskaya, L. Yu. Nad'kin, and P. I. Khadzhi, Opt. Spektrosk. **92**, 301 (2002) [Opt. Spectrosc. **92**, 267 (2002)].
10. P. I. Khadzhi, L. Yu. Nad'kin, and K. D. Lyakhomskaya, in *Proceedings of the International Quantum Electronic Conference IQEC 2002, Moscow, 2002*, p. 237.

Translated by P. Pozdeev

Technical Physics Letters, Vol. 31, No. 1, 2005, pp. 36–39. Translated from Pis'ma v Zhurnal Tekhnicheskoĭ Fiziki, Vol. 31, No. 1, 2005, pp. 73–81.

Response of the Electric Resistance of 40-nm-Thick $La_{0.67}Ca_{0.33}MnO_3$ Films to an Increase in the Lattice Mismatch between Film and Substrate

Yu. A. Boikov* and V. A. Danilov

Ioffe Physicotechnical Institute, Russian Academy of Sciences, St. Petersburg, 194021 Russia

** e-mail: yu.boikov@mail.ioffe.ru*

Received July 14, 2004

Abstract—We have studied the structure and resistivity of 40-nm-thick $La_{0.67}Ca_{0.33}MnO_3$ (LCMO) films coherently grown on (001)-oriented $La_{0.29}Sr_{0.71}Al_{0.65}Ta_{0.35}O_3$ single crystal substrates bearing epitaxial interlayers of strontium titanate with a thickness of 7 or 70 nm. As the effective mismatch between the crystal lattice parameters of the film and substrate increases, the ρ value exhibits a sharp growth, while the maximum of the $\rho(T)$ curve shifts by ~40 K toward lower temperatures. At $T < 150$ K, the temperature dependence of the resistivity of the LCMO films obeys the relation $\rho \sim \rho_1 T^{4.5}$, where the coefficient ρ_1 decreases with increasing applied magnetic field strength and with decreasing lattice mismatch between the manganite film and the substrate. © *2005 Pleiades Publishing, Inc.*

Perovskitelike manganites of the $La_{0.67}(Ca,Sr)_{0.33}MnO_3$ type are promising materials for the readout heads in magnetic memory devices [1], magnetic random access memory cells [2], IR radiation sensors [3], etc. For these practical applications, manganite solid solutions have to be obtained in the form of thin layers on the surface of substrates made of the materials used in microelectronics. Thin films of $La_{0.67}(Sr,Ca)_{0.33}MnO_3$ grown on substrates with a considerable mismatch m between the crystal lattice parameters and a significant difference between the linear expansion coefficients β of the film and substrate are mechanically stressed. The effective lattice mismatch is defined as $m = (a_S - a_L)/a_S$, where a_S and a_L are the crystal lattice parameters of the substrate and deposited layer, respectively.

Despite a large number of investigations into the structure and properties of heteroepitaxial $La_{0.67}(Sr,Ca)_{0.33}MnO_3$ layers, the mechanisms responsible for the observed increase in the resistivity ρ of these films grown on substrates with increasing m are still insufficiently clear.

This Letter presents the results of an experimental investigation of the temperature dependence of ρ and the magnetoresistance of thin $La_{0.67}Ca_{0.33}MnO_3$ (LCMO) manganite films with a thickness of $d = 40$ nm coherently grown on substrates with different positive m values.

The LCMO films were obtained by means of laser deposition (ComPex 205, KrF, $\lambda = 248$ nm, $\tau = 30$ ns). The film growth conditions are described in detail elsewhere [4, 7]. The films were obtained on polished (001)-oriented $La_{0.29}Sr_{0.71}Al_{0.65}Ta_{0.35}O_3$ (LSATO) single crystal substrates with a thickness of $d_1 = 500$ μm (Crystek, USA). In order to obtain 40-nm-thick LCMO films on substrates with different m but the same β values, the (001)LSATO surface was covered (immediately prior to the LCMO growth) by a layer of $SrTiO_3$ (STO) with a thickness of $d_2 = 7$ or 70 nm. The STO layer was grown by laser deposition under the same conditions as the manganite film. Since $d_1 \gg d_2$, the temperature coefficient of linear expansion of the STO/LSATO substrate was determined by that of LSATO ($\beta \approx 10 \times 10^{-6}$ K^{-1} [8]).

The structures of the STO interlayers and LCMO films on STO/LSATO were studied by X-ray diffraction (Philips X'pert MRD; ω/2θ and ϕ scans; rocking curves). The layer thicknesses were determined from data on the width of the satellite Laue peaks clearly observed on the X-ray diffractograms (Fig. 1). In order to evaluate the crystal lattice parameters of the grown films, the ω/2θ scans were performed so that the incident and reflected X-ray beams were in the plane perpendicular to the (101) or (001) planes in the LSATO crystal.

The dc resistance R of the LCMO films was measured in the van der Pauw geometry in the absence of magnetic fields or in a magnetic field of $\mu_0 H = 0$–5 T. The measurements were performed on square manganite films with four silver contacts deposited at the corners. The resistivity ρ was calculated as $\rho = R\pi d/\ln 2$ [9]. The magnetic field was applied parallel to the substrate plane.

The results of the X-ray diffraction measurements confirmed that the two-layer LCMO/STO hetero-

structures were epitaxially grown on the (001)LSATO surface so that the (001) planes and [010] directions in both LCMO and STO were parallel to the corresponding planes and directions of LSATO. Figure 1 shows fragments of X-ray diffractograms for the (40 nm)LCMO/(7 nm)STO/LSATO and (40 nm)LCMO/(70 nm)STO/LSATO heterostructures. The presence of Laue satellites in these patterns is indicative of the homogeneity of film thicknesses in the STO/LCMO bilayer. The $\omega/2\theta$ and ϕ scans for the LCMO films grown on (001)LSATO substrates without buffer layers were reported in [4]. The unit cell parameters of the manganite film and the STO interlayers measured in the substrate plane ($a_\parallel$) and along the normal to the substrate surface ($a_\perp$) are given in the table. Since the lattice parameter of the cubic STO single crystal (a = 3.905 Å [10]) was greater than the parameter of the pseudocubic unit cell of LSATO (a = 3.868 Å [8]), the STO interlayer grown on the (001)LSATO surface occurred under the action of lateral compressive stresses. The $a_\parallel$ value in a 7-nm-thick STO layer was smaller than that in the 70-nm-thick layer (see table). As the d_2 value increased, the mechanical stresses in the STO layer exhibited partial relaxation. The unit cell volume $V_{eff} = a_\perp a_\parallel^2$ (see table) in STO interlayers elastically strained by the substrate (biaxial compression) was smaller than the value in a free STO single crystal (~59.55 $Å^3$ [10]).

The positive effective mismatch m between the crystal lattice parameters of the LCMO film (pseudocubic lattice with a = 3.858 Å [11]) and the LSATO substrate covered with an STO buffer layer increased from 0.3% for a 7-nm-thick interlayer to 0.7% for the 70-nm-thick interlayer. The growth in m with increasing d_2 gives rise to biaxial lateral tensile stresses in the manganite film. As a result, the parameter $a_\perp$ of the manganite film in the (40 nm)LCMO/(70 nm)STO/LSATO heterostructure is smaller than that in the (40 nm)LCMO/(7 nm)STO/LSATO structure (see table). This decrease in $a_\perp$ of the manganite film with increasing STO interlayer thickness in the (40 nm)LCMO/STO/LSATO heterostructure is clearly manifested by a shift of the (002)LCMO peak in the X-ray diffractograms (Fig. 1). The parameter $a_\parallel$ of the 40-nm-thick LCMO films grown on both the (70 nm)STO/LSATO and (7 nm)STO/LSATO substrates coincided with the corresponding value in the STO interlayer (see table). Thus, the LCMO manganite films were coherently grown on the STO/LCATO surface.

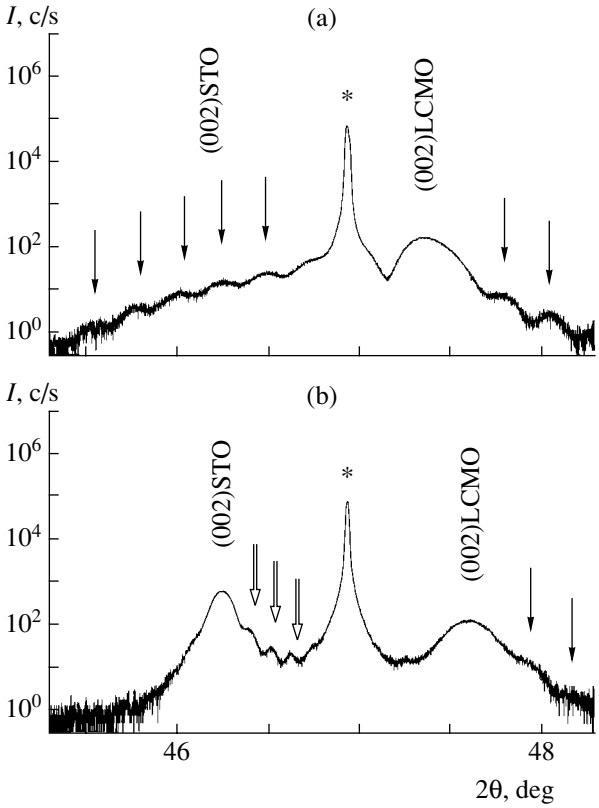

Fig. 1. The X-ray diffractograms ($CaK_{\alpha 1}$, $\omega/2\theta$ scan) of (a) (40 nm)LCMO/(7 nm)STO/LSATO and (b) (40 nm)LCMO/(70 nm)STO/LSATO heterostructures measured so that the incident and reflected X-ray beams were in the plane perpendicular to (001)LSATO. Arrows indicate the Laue satellite peaks for the manganite film, asterisks indicate (002)LSATO reflections, and double arrows indicate the Laue satellites for the STO interlayer.

It should be noted that biaxial lateral tensile stresses operating in the course of nucleation and growth of the manganite film favor an increase in the unit cell volume (see table). The mechanisms responsible for the change in V_{eff} in biaxially stressed LCMO films were considered

Crystal lattice parameters of layers in (40 nm)LCMO/STO/(001)LSATO heterostructures

Sample no.	STO interlayer				LCMO manganite film				
	d_2, nm	$a_\perp$, Å	$a_\parallel$, Å	V_{eff}, $Å^3$	d, nm	$a_\perp$, Å	$a_\parallel$, Å	V_{eff}, $Å^3$	FWHM, deg
1	7	3.94*	3.87*	59.01	40	3.833	3.868	57.40	0.08
2	70	3.923	3.887	59.27	40	3.817	3.888	57.57	0.10

Note: The error of determination for the $a_\perp$ and $a_\parallel$ values was ±0.003 Å for the LCMO and STO layers with thicknesses above 35 nm, and ±0.01 Å for a 7-nm-thick STO interlayer (indicated by asterisk).

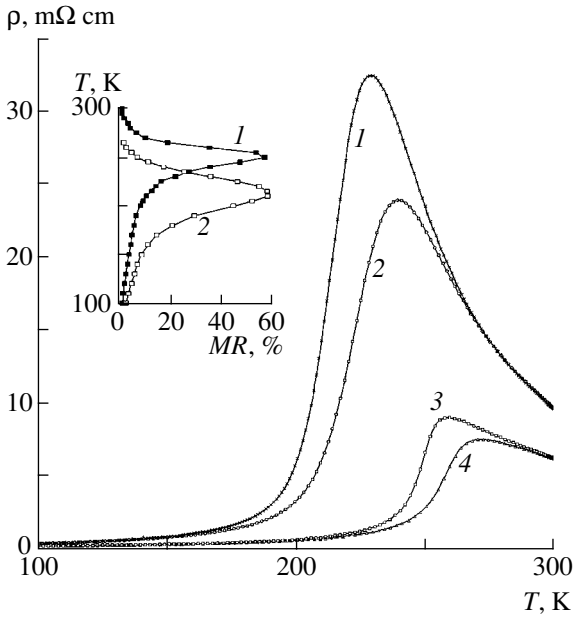

Fig. 2. Temperature dependences of the resistivity ρ for 40-nm-thick LCMO films grown on (*1*, *2*) (70 nm)STO/LSATO and (*3*, *4*) (7 nm)STO/LSATO substrates, measured (*1*, *3*) without a magnetic field ($\mu_0 H = 0$ and (*2*, *4*) with an applied magnetic field $\mu_0 H = 1$ T. The inset shows the temperature dependence of the magnetoresistance at $\mu_0 H = 1$ T for 40-nm-thick LCMO films on (*1*) (7 nm)STO/LSATO and (*2*) (70 nm)STO/LSATO substrates.

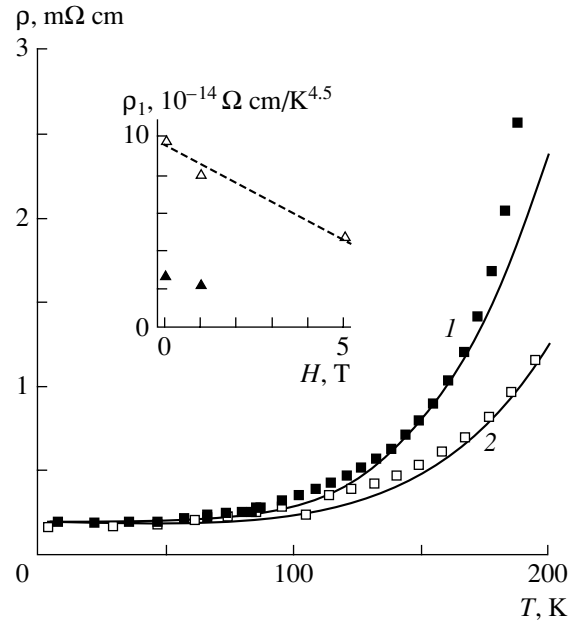

Fig. 3. Temperature dependences of the resistivity ρ for 40-nm-thick LCMO films grown on a (70 nm)STO/LSATO substrate and measured in the range $T < 200$ K (*1*) without a magnetic field ($\mu_0 H = 0$) and (*2*) with an applied magnetic field ($\mu_0 H = 5$ T). Squares present the experimental data and solid curves show the results of calculations using relation (1) for the same film. The inset shows the magnetic-field dependence of the coefficient ρ_1 for the LCMO films grown on (70 nm)STO/LSATO (open triangles) and (7 nm)STO/LSATO (black triangles) substrates; the dashed line shows that the coefficient ρ_1 exhibits an almost linear decrease with increasing magnetic field strength.

in [5, 7]. The full width at the half maximum (FWHM) of the $\omega - 2\theta$ rocking curve for the (002)LCMO reflection in the (40 nm)LCMO/(70 nm)STO/LSATO heterostructure was FWHM = 0.1°, which was about 20% greater than the value observed for the (40 nm)LCMO/(7 nm)STO/LSATO structure (see table).

Figure 2 shows the temperature dependences of the resistivities of 40-nm-thick LCMO films grown on (7 nm)STO/LSATO and (70 nm)STO/LSATO substrates. The $\rho(T)$ curve of the (40 nm)LCMO/(7 nm)STO/LSATO heterostructure exhibits a maximum at $T_M \approx 260$ K, which virtually coincides with the temperature of the analogous maximum observed for the bulk stoichiometric samples and epitaxial LCMO films heat-treated in oxygen [4]. An increase in the effective lattice mismatch between the manganite film and the STO/LSATO substrate leads to an increase in the maximum value of resistivity and to a shift of the $\rho(T)$ curve toward lower temperatures (Fig. 2). This behavior is related to oxygen depletion of the films formed under conditions of biaxial tensile stresses [7]. The high density of oxygen vacancies in the volume of the manganite film favors a decrease in the relative concentration of Mn^{4+} ions and increases the scatter of the effective bond lengths between manganese ions and oxygen ions. Both these factors lead to an increase in the ρ value and to a decrease in the temperature of the ferromagnetic ordering of electron spins on manganese ions in the LCMO film.

The sharp drop in the resistivity of the manganite films observed when the temperature decreases from T_M to 200 K is related to an increase in the density and size of high-conductivity ferromagnetic percolation channels in the volume and to a decrease in the relative disorientation of electron spins on manganese ions. At $T \ll T_M$, the main part of the LCMO film volume occurs in the ferromagnetic state. According to [12], the temperature dependence of the electric conductivity in the ferromagnetic phase of perovskitelike manganites obeys the relation

$$\rho = \rho_0 + \rho_1 T^{4.5}, \qquad (1)$$

where the constant component ρ_0 depends on the density of defects in the ferromagnetic phase and the factor ρ_1 depends on the degree of disorientation of the electron spins on manganese ions.

Figure 3 shows the temperature dependences of the resistivities of a 40-nm-thick LCMO film grown on a (70 nm)STO/LSATO substrate that were measured in the absence of a magnetic field ($\mu_0 H = 0$, black squares) and in an applied magnetic field ($\mu_0 H = 5$ T, open

squares). The solid curves present the temperature dependences $\rho(T)$ calculated using relation (1) with $\rho_0 = 0.18$ mΩ cm ($\rho_0 = \rho(4.2\ \text{K})$) and the ρ_1 values determined for $\rho(T^{4.5})$ plots fitted to the experimental curves in the range $4.2\ \text{K} < T < 50\ \text{K}$. The parameter ρ_1 exhibits a linear decrease with increasing field in the $\mu_0 H = 0$–5 T interval (see the inset in Fig. 3). This behavior is explained by damping of the spin waves with increasing magnetic field strength. An analogous magnetic-field dependence of ρ_1 for the epitaxial LCMO films was reported by Snyder *et al.* [13]. For comparison, the inset in Fig. 3 shows the values of ρ_1 determined for a 40-nm-thick LCMO film grown on a (7 nm)STO/LSATO substrate and measured at $\mu_0 H = 0$ and 1 T (the LCMO film was formed under the conditions of weak mechanical stresses). As can be seen, the ρ_1 value for the LCMO film grown on the (70 nm)STO/LSATO substrate is about three times that of the film grown on the (7 nm)STO/LSATO substrate. The relatively high ρ_1 values observed for the LCMO films grown on the STO/LSATO substrates with a greater lattice mismatch suggest that inhomogeneous mechanical stresses operating during the deposition of the manganite layer lead to an increase in the spatial disorientation of the vector of spontaneous magnetization in ferromagnetic domains of the film.

The inset in Fig. 2 shows the temperature dependence of the magnetoresistance $MR = [\rho(\mu_0 H = 1\ \text{T}) - \rho(\mu_0 H = 0)]/\rho(\mu_0 H = 0)$ for the LCMO films grown on STO/LSATO substrates with $d_2 = 7$ and 70 nm. The maximum absolute values of the negative magnetoresistance at $\mu_0 H = 1$ T for the manganite films in both cases reached $MR = 60\%$. As the effective lattice mismatch between the LCMO film and the STO/LSATO substrate increases from 0.3 to 0.7%, the maximum of the $MR(T)$ curve shifts by approximately 40 K toward lower temperatures and the peak width exhibits an almost twofold increase (see the inset in Fig. 2). This broadening, observed for the (40 nm)LCMO/(70 nm)STO/LSATO heterostructure, can be related to the high and inhomogeneous density of oxygen vacancies in the film volume and/or to the high spatial disorientation of the electron spins on manganese ions in the film grown on the substrate with a large mismatch *m*.

Acknowledgments. This study was supported in part by the Presidium of the Russian Academy of Sciences within the framework of the program "Low-Dimensional Quantum Nanostructures" (project no. 9B19) and by the Russian Foundation for Basic Research (project no. 04-02-16212).

REFERENCES

1. Y. Tokura, *Colossal Magnetoresistive Oxides*, Ed. by Y. Tokura (Gordon and Beach, Amsterdam, 2000), p. 2.
2. S. S. P. Parkin, K. P. Roche, M. G. Samant, *et al.*, J. Appl. Phys. **85**, 5828 (1999).
3. A. Goyal, M. Rajeswari, R. Shreekala, *et al.*, Appl. Phys. Lett. **71**, 2535 (1997).
4. Yu. A. Boikov, T. Klaeson, and A. Yu. Boikov, Zh. Tekh. Fiz. **71** (10), 54 (2001) [Tech. Phys. **46**, 1260 (2001)].
5. Yu. A. Boikov, T. Claeson, and A. Yu. Boikov, Fiz. Tverd. Tela (St. Petersburg) **45**, 1040 (2003) [Phys. Solid State **45**, 1090 (2003)].
6. Yu. A. Boikov and V. A. Danilov, Pis'ma Zh. Tekh. Fiz. **30** (13), 12 (2004) [Tech. Phys. Lett. **30**, 535 (2004)].
7. Yu. A. Boikov, R. Gunnarsson, and T. Claeson, J. Appl. Phys. (2004) (in press).
8. Crystek Corporation, LSATO Specification.
9. T. I. Kamins, J. Appl. Phys. **42**, 4357 (1971).
10. R. W. G. Wyckoff, *Crystal Structures* (Interscience, New York, 1964), Vol. 2, p. 394.
11. C. J. Lu, Z. L. Wang, C. Kwon, and Q. X. Jia, J. Appl. Phys. **88**, 4032 (2000).
12. K. Kubo and N. Ohata, J. Phys. Soc. Jpn. **33**, 21 (1972).
13. G. J. Snyder, R. Hiskes, S. DiCarolis, *et al.*, Phys. Rev. B **53**, 14434 (1996).

Translated by P. Pozdeev

Technical Physics Letters, Vol. 31, No. 1, 2005, pp. 4–8. Translated from Pis'ma v Zhurnal Tekhnicheskoĭ Fiziki, Vol. 31, No. 1, 2005, pp. 9–16.

Method of Determining the Control Functions for Wave Processes in Regions with Mobile Boundaries (Cylindrical Symmetry)

V. S. Krutikov

Institute of Pulsed Processes and Technologies, National Academy of Sciences of Ukraine, Nikolaev, Ukraine

e-mail: ipre@iipt.aip.mk.ua

Received July 1, 2004

Abstract—Exact analytical solutions of the wave equation in regions with mobile boundaries for the general case of cylindrical symmetry are obtained using an original method previously developed for solving inverse problems with allowance for the interaction of nonlinear arguments. The obtained solutions are universal and valid for both inverse and direct problems. A method of eliminating logarithmic singularities, known to exist in the case of cylindrical symmetry, is proposed for the quantitative determination of the control functions of wave processes in regions with mobile boundaries. © *2005 Pleiades Publishing, Inc.*

As is known, the wave equation serves a base mathematical model for many physical processes, and investigations of the related phenomena are frequently aimed at solving the task of controlling such processes. The possibility of controlling these processes usually depends both on the availability of exact analytical solutions of the inverse wave problem (control problem) and (to an even greater extent) on the formulation of mathematical models providing a theoretical description for the entire physical variety of wave fields. One such important mathematical model is offered by the wave equation considered in regions with mobile (probably permeable) boundaries.

As is known, control is a function of organized systems of various types (biological, physical, technical, social, etc.) aimed at retaining a certain structure, maintaining a certain regime of activity, or realizing a certain program and reaching set goals. The solution of a control problem consists in determining the corresponding control function. Within the framework of the mathematical problem under consideration, control implies knowledge of either (case 1) the function of velocity (of the motion and permeability of the mobile boundary) or (case 2) the function of pressure (at the mobile boundary). The aim of investigations related to the control problem is to determine the control functions for the two cases, ensuring the obtaining of preset wave fields of velocity and pressure at the points of interest, including the near-field zone and the mobile boundary surfaces (where the experimental determination of these fields is difficult or impossible), and providing the desired variation of these fields over time.

Wave processes in the regions with mobile boundaries of a cylindrical symmetry are among the most difficult to investigate [1, 2]. Until recently, no methods were available for solving the inverse wave problems in these regions, and such problems were not considered in mathematical physics. An original approach to the wave problems involving mobile boundaries was proposed for the first time and developed by the author based on the method of inverse problems with allowance for the interaction of nonlinear arguments [3, 4]. Using this method, exact analytical expressions were obtained relating the values of the pressure and velocity functions at an arbitrary point in the wave zone to the control functions, that is, to the pressure at the mobile boundary and the velocity of the motion of this boundary. Determination of the control functions in cases 1 and 2 is of considerable importance, both from the standpoint of basic knowledge and in practical applications. Once such functions are available, it is possible, for example, to use an energy balance equation [5, 6] for determining the law of power supply to an expanding plasma front of electric discharge or a laser pulse in liquid and for obtaining a preset form of the function of pressure or velocity in a compressed medium.

However, the exact relations for the control functions exhibit singularities because the complex argument of these functions involves the law of variation of the radius of a mobile boundary, which is unknown a priori and has to be determined (in the general case, it can be nonlinear). This study presents an attempt to develop methods for the elimination of such singularities and for the quantitative determination of the control functions of wave processes in regions with mobile boundaries.

1063-7850/05/3101-0004$26.00

A wave equation with cylindrical symmetry has the following form:

$$\varphi_{tt} - a^2\varphi_{rr} - a^2 r^{-1}\varphi_r = 0, \quad (1)$$

where φ is the velocity potential, r is the coordinate, t is the time, and a is the velocity of the perturbation propagation in the initially unperturbed liquid medium. Considering zero initial conditions and applying the unilateral Laplace transformation, we obtain the operator equation

$$r\bar{\varphi}_{rr}(r, s) + \bar{\varphi}_r(r, s) - \frac{s^2}{a^2} r\bar{\varphi}(r, s) = 0. \quad (2)$$

Substituting x for $\frac{s}{a}r$, we arrive at the equation

$$\Phi_{xx} + \frac{1}{x}\Phi_x - \Phi = 0.$$

The general solution of this equation is

$$\Phi = C_1 I_0\left(\frac{s}{a}r\right) + C_2 K_0\left(\frac{s}{a}r\right). \quad (3)$$

Here, I_0, K_0, and K_1 (introduced below) are modified Bessel functions. For an infinite medium, we have $C_1 = 0$ because the functions under consideration have to be finite at $r \longrightarrow \infty$. When an arbitrary law of the pressure variation $P = f(r_1, t)$ is set at a fixed point r_1 in the wave zone (i.e., the inverse problem is solved) [3, 4], we obtain

$$\bar{\varphi} = -\frac{\bar{f}(r_1, s)K_0(\mu, r)}{s\rho K_0(\mu, r_1)}, \quad \bar{\varphi}_r = \frac{\bar{f}(r_1, s)K_1(\mu, r)}{a\rho K_0(\mu, r_1)}, \quad s\bar{\varphi} = -\frac{\bar{f}(r_1, s)K_0(\mu, r)}{\rho K_0(\mu, r_1)}, \quad (4)$$

where $\mu = s/a$, s is the Laplace transformation parameter, ρ is the density of the medium, $P = -\rho\varphi_t$, and $v = -\varphi_r$. The passage to originals (inverse transformation) in Eqs. (4) in each particular case can be performed in a rational way depending on the form of function f.

In the general case, we obtain the control functions $P(R(t), t)$ and $v(R(t), t)$, which obey the following relations:

$$\left|\int_0^t P(r, t-\tau)X(r_1)d\tau = \int_0^t f(r, \xi-\tau)X(r)d\tau\right|_{r = R(t)}, \quad (5)$$

$$\left|\rho\int_0^t v(r, t-\tau)X(r_1)d\tau = \int_0^t \frac{1}{r} f(r, \xi-\tau)X(r)\left(\tau + \frac{r}{a}\right)d\tau\right|_{r = R(t)}, \quad (6)$$

$$\left|\frac{\rho}{2}\int_0^t [r^2(t-\tau) - r_0^2]X(r_1)d\tau = \int_0^t f^*(r, \xi-\tau)X(r)\left(\tau + \frac{r}{a}\right)d\tau\right|_{r = R(t)}, \quad (7)$$

$$X(r) = \left(\tau^2 + 2\frac{r}{a}\tau\right)^{-1/2}, \quad X(r_1) = \left(\tau^2 + 2\frac{r_1}{a}\tau\right)^{-1/2},$$

$$\xi = t - \frac{r - r_0}{a}, \quad f^* = \int_0^t f(r, \xi)dt.$$

If the functions in Eqs. (5)–(7) are approximated by the Lagrange polynomials of the mth power, the control function can be expressed in terms of tabulated integrals [9, Eqs. (2.261)–(2.262)].

Setting the image of the pressure function as $P(r_1, t) = A[(t + \beta)^2 - (r_1/a)^2]^{-1/2}$ in the class of Bessel functions [10], we obtain the control functions for cases 1 and 2 in the following form:

$$P(R(t), t) = \frac{A}{\omega} - \frac{1}{2}\rho v^2(R(t), t), \quad v(R(t), t) = \frac{A(t + \beta)}{R(t)\rho\omega}, \quad (8)$$

$$R(t) = \left\{r_0^2 + \frac{2A}{\rho}[\omega - \omega_1] + \frac{2A^2}{\rho^2 a^2}\left[\ln\left|\omega - \frac{A}{\rho a^2}\right| - \ln\left|\omega_1 - \frac{A}{a^2\rho}\right|\right]\right\}^{1/2}, \quad (9)$$

where

$$\omega = \sqrt{(t + \beta)^2 - \frac{R^2(t)}{a^2}}, \quad \omega_1 = \sqrt{\beta^2 - \frac{r_0^2}{a^2}},$$

$$\beta = \alpha + \frac{r_0}{a};\ A, a, \rho, r_0, \alpha = \text{const}$$

(r_0 is the initial radius).

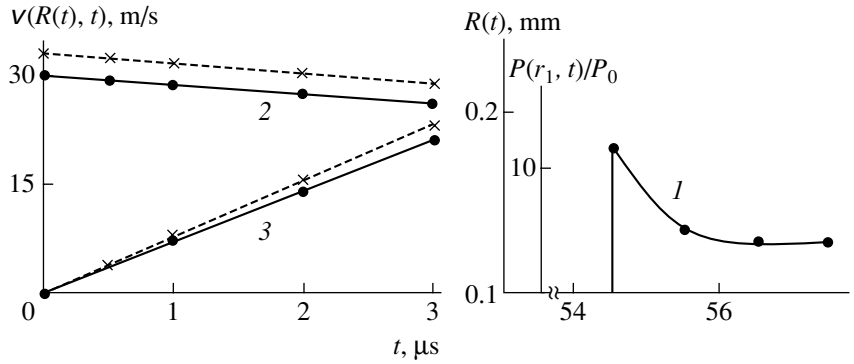

Control functions (*2*) $v(R(t), t)$ and (*3*) $R(t)$ reconstructed using preset pressure (*1*) $P(r_1, t)$ at r_1. Dashed lines (cross symbols) show the first approximation; solid lines (black circles) present the results of calculation using the complete system of equations (13) by method of characteristic curves.

In particular, for $t \longrightarrow 0$,

$$P(R(t), t) = \frac{A}{\sqrt{\left(\alpha + \frac{r_0}{a}\right)^2 - \frac{r_0^2}{a^2}}} - \frac{1}{2}\rho v^2(R(t), t), \quad (10)$$

$$v(R(t), t) = \frac{A\left(\alpha + \frac{r_0}{a}\right)}{r_0\rho\sqrt{\left(\alpha + \frac{r_0}{a}\right)^2 - \frac{r_0^2}{a^2}}}, \quad (11)$$

and for $a \longrightarrow \infty$,

$$R(t) = \sqrt{r_0^2 + \frac{2At}{\rho}}. \quad (12)$$

It should be noted that, for $\alpha \longrightarrow 0$ and $r_0 \longrightarrow 0$, formulas (8)–(12) transform into expressions obtained previously [8, Eqs. (8)–(10)].

In order to determine the control functions in cases 1 and 2 using Eqs. (5) and (6), it is necessary to know the law of variation of the mobile boundary radius. Calculations of the $R(t)$ function using Eq. (7) encounter difficulties, since the unknown function $R(t)$ enters into the argument of the function on its right-hand side.

The solution can be obtained using the iterative method.[1] The sequence of calculations is as follows:

1. Determine the value of r_2. This point is selected, based on the physical sense, as the nearest point not reached by the mobile boundary within the period of time under consideration. Since $v(R(t), t)$ is unknown and has to be determined in the course of calculations, r_2 can be approximately set with a safety margin (a) for $v(R(t), t) = \text{const} = 200$ m/s [12] or (b) using formulas (8)–(12) (the jump of pressure $P(r_1(t), t)$ for the inverse problem is known). It should be taken into account that a preset law of variation of the pressure $P(r_1, t)$ can be provided for various initial radii r_0, but the laws of motion for the boundary will be substantially different. The first approximation is calculated using Eq. (6), assuming $r = R(t) \approx r_2$ in the right-hand side. This yields the coefficients C_m of the Lagrange polynomial $v^{\mathrm{I}}(R(t), t) = \sum_0^\infty C_m t^m$ and, hence, $R^{\mathrm{I}}(t)$ in the first approximation.

2. Substituting $R^{\mathrm{I}}(t)$ into the right-hand side of Eq. (6), we obtain $v^{\mathrm{II}}(R(t), t)$ and, accordingly, $R^{\mathrm{II}}(t)$ in the second approximation, and so on. This process ensures good convergence, so that results acceptable for evaluations can be obtained even in the first approximation. Using the known $R(t)$ values (for preset A_m), the control functions in cases 1 and 2 are determined using Eqs. (5) and (6).

The solutions given by Eqs. (5)–(7) and (8)–(12) are exact (substituted into the wave equation, they make the left-hand side equal to zero) and valid for both direct and inverse problems. The boundaries of applicability of the wave equation and these exact solutions in the regions with mobile boundaries and mobile permeable boundaries have been determined in [12]; the influence of the permeability of mobile boundaries on the wave processes was considered in [8].

The data presented in the figure illustrate the results of calculations performed by method of characteristic curves [3, 13] for a system involving the equations of motion, continuity, and the state of isentropic processes in the Tait form,

$$v_t + vv_r + \rho^{-1}P_r = 0, \ \rho_t + (\rho v)'_r + (\nu - 1)r^{-1}\rho v = 0, \quad (P + B)/\rho^n = (P_0 + B)/\rho_0^n, \quad (13)$$

where B and n are constant quantities and ν is the symmetry index. We consider a cylinder expanding accord-

[1] It should be noted that Baev [11] used the iterative method for solving wave problems of a different kind not involving mobile boundaries.

ing to the law $v(R(t), t) = A\exp(-\alpha_1 t)$, where $A = 30$ m/s and $\alpha_1 = 0.046 \times 10^6$ 1/s. For the reconstruction, the pressure at $r_1 = 0.08$ m (curve *1*) for $r_0 = 0.1$ mm and $a = 1460$ m/s was approximated by the Legendre polynomial

$$P(r_1, t) = \sum_{m=0}^{\infty} A_m\left(t - \frac{r_1 - r_0}{a}\right)^m, \quad m = 0, 1, 2, 3, \quad (14)$$

where $A_0 = 11.74998$, $A_1 = -11.2383 \times 10^6$, $A_2 = 5.3499 \times 10^{12}$, and $A_3 = -0.8216 \times 10^{18}$.

The points r_2 and r_3, not reached by the moving boundary at $t_1 = 0.5 \times 10^{-6}$ s and $t_2 = 1 \times 10^{-6}$ s, respectively, are determined as $r_{2,3} = r_0 + v^* t_{1,2}$, where $v^* = 24.5$ m/s = const is the value determined using formulas (8)–(12) for $A = 11.75 \times 10^{-6}$ (kgf s)/cm^2, $\rho = 102$ (kgf s^2)/m^4, and the value of α determined from the relation [10]

$$1 \times 10^{-6} = \sqrt{\left(t^0 + \alpha + \frac{r_0}{a}\right)^2 - \frac{r_1^2}{a^2}}, \quad t^0 = \frac{r_1 - r_0}{a}.$$

These calculations yield $r_2 = 0.01125$ mm and $r_3 = 0.125$ mm.

Then, taking into account relations (6) and (14) and using the expansion $\exp(\alpha_1\tau) = 1 + \alpha_1\tau + \ldots$, we obtain the equation

$$\rho A\exp(-\alpha_1 t)\left\{\int_0^t \frac{d\tau}{X(r_1)} + \alpha_1\int_0^t \frac{\tau d\tau}{X(r_1)}\right\}$$

$$= A_0\frac{1}{r_{2,3}}\left\{\sqrt{\xi^2 + 2\frac{r_{2,3}}{a}\xi}\right\}$$

$$+ A_1\frac{1}{r_{2,3}}\left\{\left(\xi - \frac{r_{2,3}}{a}\right)Z_1 - Z_2 + \frac{r_{2,3}}{a}\xi Z_0\right\}$$

$$+ A_2\frac{1}{r_{2,3}}\left\{\left(\xi^2 - 2\frac{r_{2,3}}{a}\xi\right)Z_1 - \left(2\xi - \frac{r_{2,3}}{a}\right)Z_2 + Z_3 + \left(\xi^2\frac{r_{2,3}}{a}\right)Z_0\right\} \quad (15)$$

$$+ A_3\frac{1}{r_2}\left\{\left(-3\xi^2\frac{r_{2,3}}{a} + \xi^3\right)Z_1 + \left(-3\xi^2 + 3\frac{r_{2,3}}{a}\xi\right)Z_2\right.$$

$$\left. + \left(3\xi - \frac{r_{2,3}}{a}\right)Z_3 - Z_4 + \left(\xi^3\frac{r_{2,3}}{a}\right)Z_0\right\} + \ldots,$$

where

$$X(r_1) = \sqrt{\tau^2 + 2\frac{r_1}{a}\tau}, \quad \xi = t - \frac{r_{2,3} - r_0}{a},$$

$$Z_n = \int_0^t \frac{\tau^n d\tau}{\sqrt{t^2 + 2\frac{r_{2,3}}{a}\tau}}, \quad n = 0, 1, 2, 3, 4$$

(Z_n are tabulated integrals [9]). Substituting the above values of $r_{2,3}$ and $t_{1,2}$ into relation (15), we obtain transcendent equations for determining A and $\alpha_1 = \alpha^* \times 10^6$:

$$A\exp(-\alpha^*)\{0.19076036 + \alpha^* 0.06351\} = 6.32990393,$$

$$A\exp(-0.5\alpha^*)$$
$$\times\{0.13499004 + \alpha^* 0.022485\} = 4.46464852,$$

which can be solved by well-known methods to yield, in the first approximation,

$$A = 33, \quad \alpha_1 = 0.04462 \times 10^6 \text{ 1/s}.$$

The control functions $v(R(t), t)$ and $R(t)$ determined in the first approximation are shown in the figure by dashed lines (cross symbols). The pressure $P(R(t), t)$ was determined using the known laws of variation of the plasma front velocity and radius (direct problem), as described previously [7, 8].

Analysis of the results shows that correct control of a wave process is only possible provided that a certain level of knowledge about this process is reached (in the given case, the exact analytical expressions of the control functions for cases 1 and 2 are known). Without this exact knowledge, the control becomes merely a series of attempts to determine, by trial and error (and in most cases accidentally), the desired (or required) result, usually at the expense of lost time and funds. There are no other means of reaching the goal except those described above; solving inverse problems using the methods described in [14, 15] is problematic.

REFERENCES

1. V. K. Kedrinskiĭ, Prikl. Mekh. Tekh. Fiz., No. 4, 23 (1987).
2. V. K. Kedrinskiĭ, Fiz. Goreniya Vzryva **12**, 768 (1976).
3. V. S. Krutikov, *One-Dimensional Problems in Continuum Mechanics with Moving Boundaries* (Naukova Dumka, Kiev, 1985) [in Russian].
4. V. S. Krutikov, Dokl. Akad. Nauk **364**, 17 (1999).
5. L. M. Lyamshev, Usp. Fiz. Nauk **151**, 479 (1987) [Sov. Phys. Usp. **30**, 252 (1987)].

6. K. A. Naugol'nykh and N. A. Roĭ, *Electric Discharge in Water* (Nauka, Moscow, 1971) [in Russian].

7. V. S. Krutikov, Pis'ma Zh. Tekh. Fiz. **14**, 510 (1988) [Sov. Tech. Phys. Lett. **14**, 226 (1988)].

8. V. S. Krutikov, Dokl. Akad. Nauk **368**, 755 (1999) [Dokl. Phys. **44**, 674 (1999)].

9. I. S. Gradshtein and I. M. Ryzhik, *Table of Integrals, Series, and Products* (Nauka, Moscow, 1971; Academic, New York, 1980).

10. V. S. Krutikov, Pis'ma Zh. Tekh. Fiz. **29** (24), 7 (2003) [Tech. Phys. Lett. **29**, 1014 (2003)].

11. A. V. Baev, Dokl. Akad. Nauk SSSR **287**, 1358 (1986) [Sov. Phys. Dokl. **31**, 314 (1986)].

12. V. S. Krutikov, Akust. Zh. **42**, 534 (1996) [Acoust. Phys. **42**, 471 (1996)].

13. B. L. Rozhdestvenskiĭ and N. N. Yanenko, *Systems of Quasi-Linear Equations and Their Applications in Gas-dynamics* (Nauka, Moscow, 1968) [in Russian].

14. G. A. Grinberg, Prikl. Mat. Mekh. **31**, 193 (1967).

15. *Topics in Mathematical Physics*, Ed. by V. M. Tuchkevich (Nauka, Leningrad, 1976) [in Russian].

Translated by P. Pozdeev

Technical Physics Letters, Vol. 31, No. 1, 2005, pp. 40–42. Translated from Pis'ma v Zhurnal Tekhnicheskoĭ Fiziki, Vol. 31, No. 1, 2005, pp. 82–87.

Microwave-Stimulated Electron Trapping by Dislocations in Zinc and Cadmium Sulfides

B. M. Gorelov

Institute of Surface Chemistry, National Academy of Sciences of Ukraine, Kiev, Ukraine

e-mail: user@surfchem.freenet.kiev.ua

Received July 13, 2004

Abstract—A pulsed microwave field stimulates the tunneling trapping of electrons by dislocations and induces reversible transformations of defects in the crystals of the wide-bandgap semiconductors ZnS and CdS. © *2005 Pleiades Publishing, Inc.*

It was reported [1–3] that ultrasonic excitation of cadmium sulfide (CdS) and zinc sulfide (ZnS) crystals may lead to a reciprocating motion of dislocations, which is accompanied by the tunneling trapping of electrons from local centers and by the recharge, reconstruction, and generation of defects. These phenomena are accompanied by reversible and irreversible changes in the photoconductivity and luminescence spectra, which are determined by the character of the motion of dislocations and by the mobility of defects. The generation and irreversible reactions of defects are characteristic of the motion of dislocations and their breakaway from stoppers in the region of plastic straining at the electric field strength amplitude $E_a \approx 10^4$–10^5 V/m. In the region of elastic straining, ionization of deep centers in the field of dislocations may take place. It can be suggested that the application of a microwave field with $E \geq E_a$ to ZnS and CdS crystals makes possible the ionization and transformation of defects stimulated by the fields of moving dislocations.

This Letter reports on the results of an investigation into the ionization and transformation of defects caused by the motion of dislocations under the action of an applied microwave field. The experiments were performed on intentionally undoped high-ohmic single crystals of ZnS (cubic) and CdS with a room-temperature dark resistivity of 10^{10} and 10^7–10^9 Ω cm, respectively. The samples were cut in the form of parallelepipeds with the dimensions $2 \times 2 \times 7$ mm (ZnS) and $5 \times 5 \times 0.5$ mm (CdS). Dislocations were not intentionally introduced into the crystals studied.

The samples were placed in the node of the electric field of a transmission resonator and exposed to a pulsed electromagnetic radiation with a frequency of 9.4 GHz, a pulse power of 10^4 W, a pulse duration of 2.5 μs, a pulse repetition rate of 400 Hz, and an average power of 10 W. The irradiation was performed at room temperature in the dark. Then, the ZnS samples were characterized by the electron paramagnetic resonance (EPR) spectra of local Cr^+ and Mn^{2+} centers. The measurements were performed at 300 K in an RE-1306 spectrometer (Russia) that had a sample illumination facility equipped with a halogen lamp. The CdS samples were characterized by photoconductivity spectra measured at 77 K. The EPR and photoconductivity measurements were performed before and after microwave irradiation of the crystals.

The observed EPR spectrum of ZnS displays the well-known lines of Cd^+ and Mn^{2+} [4]. The microwave irradiation leads to a decrease in intensity of the Cr^+ line, while not affecting the Mn^{2+} line. The width and g value of the Cr^+ line does not change as a result of the irradiation. The Cr^+ centers are electron acceptors and the depth of the electron energy level can be determined from the spectra of the EPR signal excitation and quenching (Fig. 1). In the energy range $h\nu \leq 1.35$ eV, the spectrum characterizes the distribution of the levels of defect states in the bandgap, from which electrons are excited by light into the conduction band. The trapping of these electrons by Cr^{2+} ions increases the number of Cd^+ centers (Fig. 1, curve *1*). The spectrum of EPR quenching at $h\nu < 1.35$ eV reflects the process of ionization $Cr^+ \longrightarrow Cr^{2+}$ at the expense of the electron transition to the conduction band, and the minimum of $N(h\nu)$ at 1.29 eV from the conduction band bottom corresponds to the optical depth of the Cr^+ level (Fig. 1, inset (a), curve *1*). Exposure to the microwave field decreases the concentration of Cr^+ centers and modifies the entire spectrum of defect states in the bandgap. Indeed, a double 10-min exposure increases the intensity of the excitation and changes the shape of the excitation spectrum, which is indicative of the appearance of new defect states in the spectrum. In addition, the quenching band exhibits broadening and the minimum of this band shifts to 1.24 eV (Fig. 1, inset (a), curves *2* and *3*).

The kinetics of variation of the dark concentration of Cr^+ is presented in the inset (b) in Fig. 1. The expo-

1063-7850/05/3101-0040$26.00

sure to a microwave field decreases the number of Cr^+ centers, but the intensity of $Cr^+ \longrightarrow Cr^{2+}$ ionization drops with increasing exposure time. The intensity of ionization grows with decreasing initial dark concentration of Cr^+ centers and drops with decreasing irradiation power (Fig. 1, inset (b), curves *1*–*4*).

In the dark, the number of Cr^+ centers after termination of the microwave irradiation remains unchanged, which provides evidence in favor of the tunneling mechanism of the $Cr^+ \longrightarrow Cr^{2+}$ ionization process. The concentration of Cr^+ centers is restored after irradiation of the sample by a monochromatic light in the excitation wavelength range, while the excitation spectrum exhibits relaxation upon irradiation of the sample with light in various regions of the excitation range.

Thus, exposure of the ZnS sample to a high-power microwave field leads to the tunneling ionization of deep centers and modifies the spectrum of all the defect states in the bandgap. Since direct ionization of the deep centers under the action of this electromagnetic field and/or induced piezoelectric field is unlikely, we suggest that $Cr^+ \longrightarrow Cr^{2+}$ ionization is caused by the tunneling trapping of an electron on a dislocation level. The Cr^+ centers probably act as stoppers responsible for the pinning of dislocations, since an increase in the dark concentration of Cr^+ reduces the intensity of ionization. The action of microwave radiation is similar to the effect of moving dislocations on the spectrum of defects in an ultrasonic field.

An increase in intensity of the Cr^+ excitation spectrum is indicative of the growth in the number of defect states in the bandgap, while the reversibility of changes in the spectrum shows that the electromagnetic irradiation does not lead to the generation of defects or their irreversible transformation. Reversible transformation of the defect spectrum can be related to a change in the number of screening and other defects (including Cr^{2+} centers), which trap electrons and participate in the $C^{2+} \longrightarrow Cr^+$ recharge. This change takes place in the course of filling and devastation of the dislocation levels, which is accompanied by variation of the electric field of the dislocation core, dislocation barrier, and dimensions of the space charge regions of the dislocations and electron-depleted zones [5].

A relationship between the degree of filling of dislocation levels and the number of defect states in the bandgap in the presence of a microwave field is also manifested in CdS. The initial photocurrent spectrum is characterized by two weak narrow bands peaked at $\lambda_m \approx 522$ and 533 nm and one broad band with the maximum at 570 nm. Exposure to the microwave field for $t < 15$ min leads to the appearance of a dislocation band D at $\lambda_m \approx 585$ nm. The intensity of this band increases with the exposure time. This growth is accompanied by a shift of the position of the maximum of this band toward lower energies (see inset in Fig. 2) and by an increase in the dislocation noise (indicated by the bars on curve *3*). Evolution of the D band is accompanied by an increase in the intensity of the two aforementioned narrow bands. At the exposure time t increases, the two bands merge into one broad band with a maximum at $\lambda_m \approx 522$ nm (Fig. 2, curves *2* and *3*).

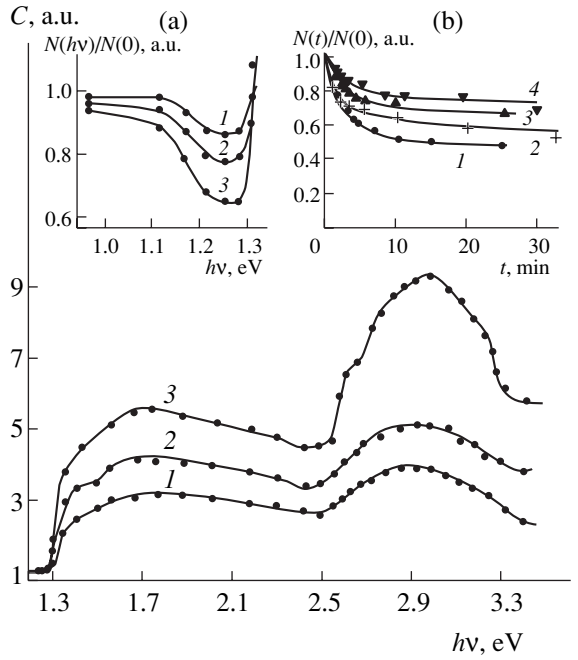

Fig. 1. The spectra of Cr^+ EPR signal excitation in ZnS (*1*) before and (*2*, *3*) after microwave irradiation of the sample for 10 and 20 min, respectively. Inset (a) shows the EPR signal quenching spectra before and after the same exposures. Inset (b) shows the kinetics of Cr^+ ionization for various initial intensities: $I(1) < I(2) < I(3) = I(4)$ (curve *4* was measured at a 10% attenuation of power).

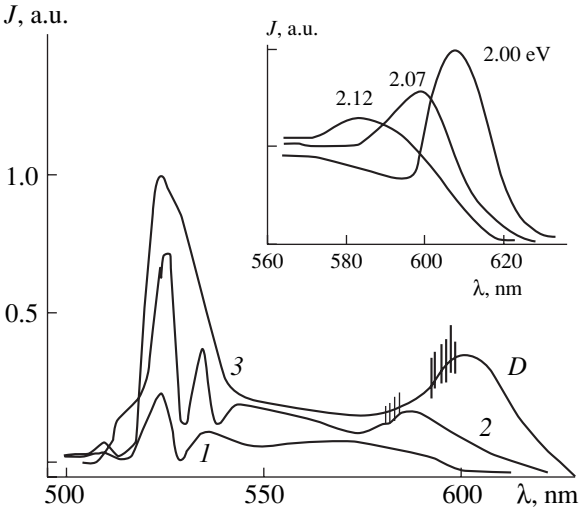

Fig. 2. The spectra of the photocurrent in CdS (*1*) before and (*2*, *3*, *4*) after microwave irradiation of the sample for 5, 10, and 15 min, respectively. The inset shows the evolution of the dislocation band D in the course of three sequential 5-min exposures. Vertical bars indicate the dislocation noise observed during the measurement of band D.

The microwave-induced changes in the spectrum of the photocurrent are reversible. Upon termination of an exposure with a duration of $t < 15$ min, the spectrum can be restored by illuminating the sample with a light at $\lambda_m \leq 522$ nm, which leads to the quenching of all three bands in the spectrum. In the dark, an increase in the microwave irradiation time to $t \approx 15$ min leads to quenching of the *D* band and the related bands at $\lambda < 540$ nm, and to restoration of the initial spectrum. Irradiation for $t > 15$ min leads to the same effect. The reversibility of the photocurrent spectrum is related to devastation of the dislocation level both on illumination and in the dark, and indicates that the external field neither produces defects nor leads to their transformation.

The aforementioned shift of the dislocation-related band toward lower energies indicates that the dislocation barrier decreases when a dislocation traps an electron, since the position of the *D* level in the course of its filling is determined by the interplay between the shift toward the valence band and the approach to the conduction band bottom as a result of the decrease in the barrier height.

The restoration of the photocurrent spectrum under illumination is related to the recombination of the electrons (trapped by dislocations) and holes appearing in the valence band upon the light-induced excitation of electrons into the conduction band from two defect levels of the valence band. In the dark, the photocurrent spectrum exhibits relaxation under the action of the microwave field because the dislocation level shifts, in the course of its filling toward the conduction band bottom, to a depth below 2.00 eV (taking into account the dislocation barrier [5]) and approaches the level of *r*-centers at $E \geq 1.4$ eV [6]. The trapping of electrons from the levels of *r*-centers creates holes in the valence band. These holes recombine with the electrons trapped by dislocations. Devastation of the dislocation level leads to the restoration of the initial spectrum.

The behavior of the spectrum of defect states under the action of a microwave field is related to variations in the degree of the dislocation level filling by trapped electrons. As the level is filled, the electron-depleted zone near dislocations decreases and the number of electron-trapping defects situated outside these depleted regions increases, which is manifested in the spectra of Cr^+ excitation and in the photocurrent spectrum. The growth in the number of charged defects and the enhancement of related fields leads to smearing and shift of the defect levels, which is reflected by the merging of the photocurrent excitation bands and by the variations in shapes of the photocurrent and Cr^+ excitation spectra.

In conclusion, the exposure of ZnS and CdS crystals to a microwave field leads to a reciprocating motion of dislocations, which is accompanied by the tunneling ionization of deep centers and reversible transformations of the spectrum of defect states in these crystals. These transformations are related to the reversible variation in the number of defects, which are situated outside the space charge regions of dislocations and participate in the excitation of the photocurrent and Cr^+ centers. The number of such defects depends on the degree of the dislocation level filling and on the size of the space charge regions of dislocations, which are influenced by the microwave field and light.

REFERENCES

1. I. V. Ostrovskiĭ, Pis'ma Zh. Éksp. Teor. Fiz. **34**, 463 (1981) [JETP Lett. **34**, 446 (1981)].
2. V. L. Gromashevskiĭ, V. V. Dyakin, E. A. Sal'kov, *et al.*, Ukr. Fiz. Zh. **29**, 550 (1984).
3. B. M. Gorelov, O. A. Korotchenkov, I. V. Ostrovskiĭ, and M. K. Sheinkman, Pis'ma Zh. Tekh. Fiz. **11**, 1315 (1985) [Sov. Tech. Phys. Lett. **11**, 543 (1985)].
4. S. A. Omel'chenko, M. F. Bulanyĭ, and O. V. Khmelenko, Fiz. Tverd. Tela (St. Petersburg) **45**, 1308 (2003) [Phys. Solid State **45**, 1688 (2003)].
5. H. F. Matare, *Defects Electronics in Semiconductors* (Wiley, New York, 1971).
6. R. H. Bube, *Photoconductivity of Solids* (Wiley, New York, 1960).

Translated by P. Pozdeev

Technical Physics Letters, Vol. 31, No. 1, 2005, pp. 43–45. Translated from Pis'ma v Zhurnal Tekhnicheskoĭ Fiziki, Vol. 31, No. 1, 2005, pp. 88–94.

Thermal Stability of FCC Structure in FeNi Films of Various Thicknesses

A. M. Gorovoi

Irkutsk Military Aircraft Engineering Institute, Irkutsk, Russia

e-mail: dmsafronov@yandex.ru

Received May 19, 2004; in final form, August 19, 2004

Abstract—Thin films of a polymorphous iron–nickel (FeNi) alloy with a nickel content of 25–30% and a thickness from 0.1 to 1.3 μm have been obtained by thermal deposition in vacuum in a setup with turbomolecular pumps. The phase transitions in these FeNi films have been studied by X-ray diffraction and magnetic phase analysis. The results of these measurements show that the crystallographic stability of a face-centered cubic (fcc) structure in a temperature interval from 70 to –196°C depends on the film thickness. It is suggested that this dependence is determined by crystal structure defects, the density of which is proportional to the film thickness and grain size. It is also established that substrate type does not influence the temperature interval for the existence of stable crystallographic modifications in the sample studied. The results can be used for determining the optimum composition and thickness of a working FeNi layer in thermovoltaic recording media, ensuring a wide operating temperature range. © *2005 Pleiades Publishing, Inc.*

It has recently been demonstrated [1–6] that thermovoltaic analog-digital data recording media of a new type can be created using the Seebeck effect in polymorphous iron–nickel (FeNi) alloys with certain composition [7]. In addition to solving problems related to the development in the design of thermovoltaic memory and its adaptation to the existing write/read facilities, it is very important to provide for a significant increase in the working characteristics of new devices as compared to those of existing analogs.

This Letter presents the results of an analysis of the factors influencing the temperature range for the reliable storage of data recorded in thermovoltaic memory. The study was aimed at providing a maximum increase in the working temperature range in comparison to that in the magnetic and magnetooptical data storage systems.

The recording medium in the proposed thermovoltaic memory is a thin film of a polymorphous FeNi alloy. Operation of this memory is based on the ability of such alloys to occur in two different stable crystal modifications representing the α phase with a body-centered cubic (bcc) lattice and the γ phase with a face-centered cubic (fcc) lattice [8]. The principle of data readout consists in thermo emf generation at the boundary between elementary data cells in the track locally heated by a sharply focused reading laser beam. If the cells differ in their phase state, the laser-induced thermo emf can be assigned logical unity; if the two adjacent cells occur in the same phase state, no thermo emf that corresponds to logical zero is generated.

A thermoelectric response signal with an amplitude of 1.9 mV/100 K is fed immediately into a readout device without any intermediate processing (in contrast to the optical and magnetic memory devices). This provides a significant increase in the signal to noise ratio and improves the quality of data readout. This circumstance and the absolute stability of the α and γ phases in FeNi alloys under the action of electromagnetic fields are the main advantages of the proposed thermovoltaic memory devices in comparison to the existing analogs. The thermomagnetic data carriers described in [1–6] can be manufactured in the form of a flexible ribbon or hard disk and adapted to the existing readout facilities.

Determination of the working temperature range of the new data recording devices reduces to establishing the boundaries for the existence of stable α and γ phases, that is, for the temperature interval in which these stable phases may coexist. The lower boundary is determined by the onset of the $\gamma \longrightarrow \alpha$ conversion (M_1), while the upper boundary corresponds to the onset of the $\alpha \longrightarrow \gamma$ transition (A_1). The results of investigations of the $\alpha \longleftrightarrow \gamma$ transformations in thin FeNi films with a composition in the indicated interval showed that it is possible to obtain a significant expansion of the region of stability of the metastable high-temperature γ phase toward lower temperatures.

In the initial (as-deposited) state, the crystal lattice in the films corresponded to the α phase. Subsequent 1-h annealing at 600°C in a vacuum of 2×10^{-6} Torr led to the $\alpha \longrightarrow \gamma$ transition with the formation of a homogeneous γ-FeNi solid solution. The temperature M_1 of the onset of the $\gamma \longleftrightarrow \alpha$ conversion was determined by means of magnetic phase analysis. For the material under consideration, this is the most sensitive technique

1063-7850/05/3101-0043$26.00 © 2005 Pleiades Publishing, Inc.

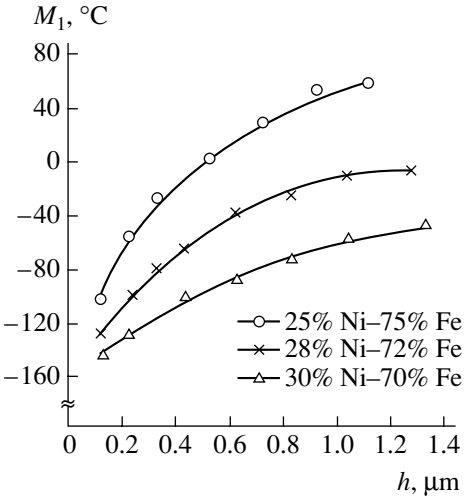

Fig. 1. The experimental dependence of the temperature of the onset of $\gamma \longleftrightarrow \alpha$ transition M_1 on the film thickness h in FeNi films of various compositions.

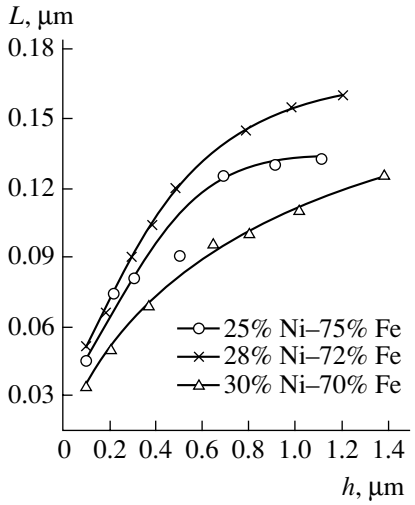

Fig. 2. A plot of the size L of coherent scattering domains versus film thickness h in FeNi films of various compositions.

capable of detecting the presence of ferromagnetic α phase regions with a total volume accounting for less than 1% in the paramagnetic γ phase of the films with a nickel content of 25 and 28%. The transition temperature M_1 in the films containing 30% Ni was detected by an increase in the magnetic moment, since the magnetization of the α phase in the samples of this composition is about five times that of the γ phase.

Since the thermovoltaic data carriers can be manufactured in the form of a hard disk with a metal base, the experiments were performed with the FeNi films deposited in vacuum onto quartz, sitall (glass-ceramic composite) plates, and copper plates with a chromium (≈0.1-μm-thick) underlayer that significantly improves the adhesion of the FeNi films to a substrate. It was established that the type of substrate used for the deposition of FeNi films does not significantly influence the transition temperature M_1, the grain size, and completeness of the $\gamma \longleftrightarrow \alpha$ conversion on cooling the samples to –196°C.

The results of our investigations show that the temperature interval for the reliable storage of data recorded in thermovoltaic media is determined primarily by the composition and thickness of the FeNi alloy film in the data track. Figure 1 shows experimental plots of the transition temperature M_1 versus thickness h of FeNi films containing 25–30% Ni. In the samples with these compositions, the transition temperature M_1 increases with the film thickness. The behavior observed in the films with increasing nickel content indicates that the temperatures of the onset of the $\gamma \longleftrightarrow \alpha$ conversion asymptotically approach the transition temperature M_1 for the massive samples. These temperatures are 100, 10, and –40°C for the alloys containing 25, 28, and 30% Ni, respectively.

The FeNi film thickness influences both the temperature corresponding to the loss of stability of the γ phase and the size of the grains of this phase (Fig. 2). It should be noted that, according to the electron-microscopic data, the grain size in thin FeNi films corresponds to the size L of coherent scattering domains calculated using the standard method based on the X-ray diffraction data [8, 9]. This implies that the grains in thin films are not separated into blocks as they are in the same alloys obtained by metallurgical methods. As a result, the density of dislocations in the grains formed in thin films is lower than that in massive samples.

This leads to the expansion of the temperature interval of stability of the γ phase in thin films of FeNi alloys and, hence, of the temperature range of reliable data storage in carriers based on such media toward lower temperatures. The factors responsible for the increase in the stability of the γ phase with respect to the $\gamma \longleftrightarrow \alpha$ phase transition should be analyzed in terms of the theory of martensitic transformations.

According to the theory of heterogeneous nucleation, the α phase in a polymorphous FeNi alloy can form at the nucleation centers, the role of which is played by the crystal lattice defects, in particular, by dislocations [10]. In the case under consideration, the degree of suppression of the $\gamma \longleftrightarrow \alpha$ conversion grows with decreasing film thickness, which can be explained by a decrease in the density of dislocations. A similar phenomenon has been observed in a nickel-based steel [11], where a significant reduction in the grain size was accompanied by a decrease in the dislocation density. It was suggested [11], that the lower density of dislocations decreased the efficiency of the nucleation and growth of α phase crystals. The results of the present investigation lead to a conclusion that the stability with respect to the $\gamma \longleftrightarrow \alpha$ transition in thin films of FeNi alloys is probably determined by the density of

dislocations, which is dependent on the film thickness and the grain size in the initial crystallographic phase.

Evidence in favor of the dislocation mechanism of nucleation of the α phase in thin FeNi films is provided, apart from the dependence of the density of dislocations on the grain size, by the possible increase in this density with increasing film thickness. In the course of the heat treatment leading to the $\gamma \longleftrightarrow \alpha$ transition, a certain fraction of dislocations can escape (owing to their mobility) at the surface of a thin film. Therefore, by analogy with what takes place in the case of decreasing grain size reduction of the film thickness must favor a decrease in the density of dislocations. Therefore, the expansion of the working temperature range of the proposed thermovoltaic data carriers [1–6], which is related to an increase in stability of the γ phase with respect to the $\gamma \longleftrightarrow \alpha$ transition with decreasing FeNi film thickness, can be due to both factors considered above. Each factor contributes to the mechanism of decrease in the phase transition temperature M_1.

Thus, the results presented in this paper show that, in developing the technology of data carriers of the thermomagnetic type, it is necessary to take into account the required working temperature range for selecting the composition and thickness of FeNi films for the recording medium. The lower boundary temperature of reliable data storage on thermovoltaic data carriers is determined by the transition temperature M_1 in an FeNi film of variable composition and thickness (Fig. 1) used in the working layer of the data carrier. The upper boundary temperature is determined by the stability of the α phase with respect to the $\gamma \longleftrightarrow \alpha$ transition, that is, by the transition temperature A_1. For thin FeNi films with a homogeneous composition, the dependence of A_1 on the percentage content of nickel is the same as in massive alloys, whereby the transition temperature monotonically decreases from 480 to 390°C as the nickel content increases from 25 to 30%.

REFERENCES

1. A. M. Gorovoĭ and M. V. Shmidt, in *Proceedings of the 2nd International Conference "Magnetic Materials," Irkutsk, 2003*, pp. 140–141.
2. A. M. Gorovoĭ and D. A. Safronov, in *Proceedings of the 2nd International Conference "Magnetic Materials," Irkutsk, 2003*, p. 138.
3. A. M. Gorovoĭ and A. N. Malov, Proc. SPIE **5129**, 255 (2003).
4. A. M. Gorovoĭ and A. N. Malov, Proc. SPIE **5134**, 155 (2003).
5. A. M. Gorovoĭ and A. N. Malov, Komp'yut. Opt. **25**, 104 (2003).
6. A. M. Gorovoĭ and A. N. Malov, Komp'yut. Opt. **25**, 109 (2003).
7. I. V. Shelkovnikov, A. M. Gorovoi, and N. A. Belebeev, in *Proceedings of the 13th All-Russia Scientific–Technical Conference on the Problems of Combat Readiness, Military Applications, Technical Exploitation, and Security of Aircraft in the Geo-Climate Conditions of Siberia, Trans-Baikalia, and Far-East Regions, Irkutsk, 2003* (IVAII, Irkutsk, 2003), Part 1, pp. 95–97.
8. M. Hansen and K. Anderko, *Constitution of Binary Alloys* (McGraw-Hill, New York, 1958).
9. S. S. Gorelik, L. N. Rastorguev, and Yu. A. Skakov, *Radiographic and Electron-Diffraction Analysis* (Metallurgiya, Moscow, 1972) [in Russian].
10. Yu. N. Petrov, Metallofizika, No. 55, 11 (1974).
11. P. Yu. Volosevich, V. N. Gridnev, and Yu. N. Petrov, Metallofizika, No. 55, 8 (1974).

Translated by P. Pozdeev

Technical Physics Letters, Vol. 31, No. 1, 2005, pp. 46–47. Translated from Pis'ma v Zhurnal Tekhnicheskoĭ Fiziki, Vol. 31, No. 2, 2005, pp. 1–5.

Damage of Integrated Circuits by High-Velocity Microparticles Penetrating Thick-Wall Obstacles

O. V. Roman, O. A. Dybov, G. S. Romanov, and S. M. Usherenko

Research Institute of Pulsed Processes, National Academy of Sciences of Belarus, Minsk, Belarus

e-mail: impuls@bn.by

Received August 3, 2004

Abstract—A flux of high-velocity microparticles, transmitted through a thick steel obstacle in the regime of superdeep penetration, also passes through the case of an integrated circuit (IC) situated behind this wall and produces damage of the IC chip. © *2005 Pleiades Publishing, Inc.*

The phenomenon of anomalous or superdeep penetration (SDP) consists in a flux of high-velocity particles impinging on a thick metal obstacle and the particles penetrating through the metal to an anomalously large depth: 10^2–10^4 times the initial particle-projectile size, which amounts to several tens or even hundreds of millimeters [1, 2]. The penetrating particles leave traces (tracks) in depth of the metal in the form of completely or partly collapsed channels, which can be revealed by chemical or electrochemical etching of cut samples. An analysis of the pattern of revealed tracks showed that their diameters are several tens or hundreds of times smaller than the particle-projectile size. Investigations of thin (≤0.5-mm-thick) plates cut from a material penetrated by a flux of particles normally incident onto the surface in the SDP regime showed no evidence of permeability, which implies that particles penetrating through the obstacle leave no through pores. These well-established facts—anomalous depth, very small channel diameter (relative to the particle-projectile size), and the absence of through porosity (perforation)—are the principal substantial features distinguishing anomalous penetration (SDP) regime from the case of penetration of separate high-velocity particles into the same obstacle.

For microscopic particles of silicon carbide, the main experimentally determined flux parameters corresponding to the SDP regime are an average density of ~2 g/cm^3 and an impact velocity of 900–300 m/s (the velocity varies in the course of interaction, which lasts for about ~200 μs [3]). When the flux of such high-velocity microparticles impinges in the SDP regime on an obstacle with a thickness below the maximum penetration depth, the particles penetrate through the material layer and escape from its rear surface together with knocked-out particles of the obstacle material. Figure 1 presents micrographs obtained by scanning electron microscopy (SEM) of plastic foils (80-μm-thick 5.5″-diameter flexible computer diskettes) perforated by particles escaping from the rear surface of a thick steel plate penetrated by silicon carbide microparticles in the SDP regime. The foil number (counted from the rear target surface) indicates its position in a stack used as a detector, which was pressed via a thin interlayer (tracing paper) to the rear surface of the steel target. Examination of the damaged foils showed that the character of their interaction with the particles-projectiles could vary [2]. In particular, inclusions contained the materials of particles and the obstacle in various proportions. In this stage of research, we did not find any correlations for this ratio.

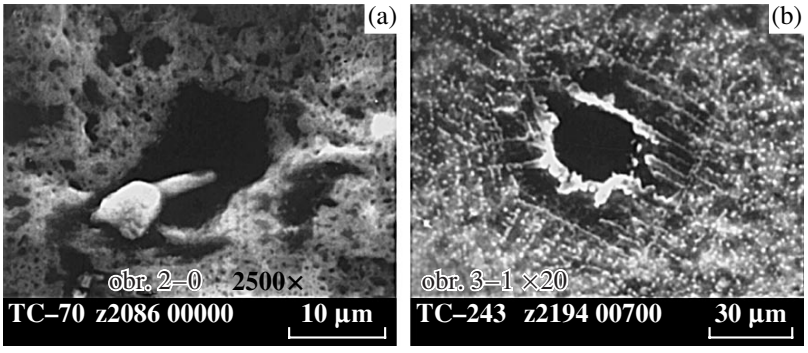

Fig. 1. SEM micrographs showing traces of the interaction of SiC particles with plastic foils behind a steel obstacle penetrated in the SDP regime: (a) 200-mm-thick steel plate, 2nd foil in a 30-layer stack; (b) 50-mm-thick steel plate, 31st foil in a 40-layer stack.

1063-7850/05/3101-0046$26.00 © 2005 Pleiades Publishing, Inc.

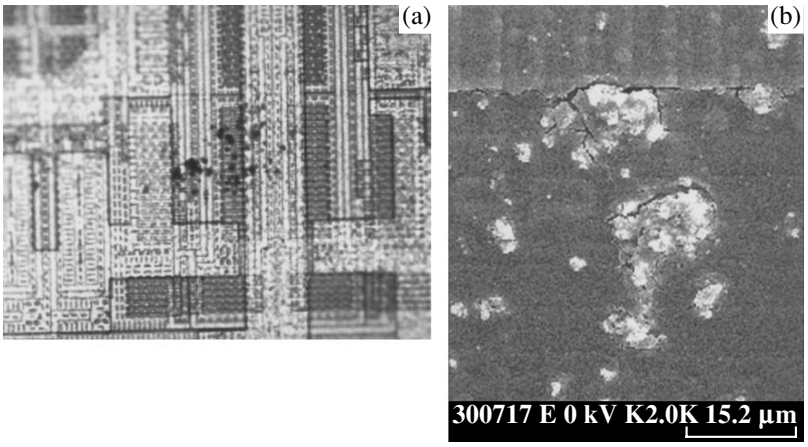

Fig. 2. Micrographs of inclusions formed in the chip of an IC by microparticles penetrating through an obstacle and the IC case in the SDP regime: (a) optical microscope, ×200; (b) scanning electron microscope, ×2000.

Previously [2], we suggested that the material (of both projectiles and obstacle) is ejected from the rear side of the obstacle in the form of a microjet. This explains the fact of penetration through a stack of 40 aluminum or copper foils (each 10 μm thick), with a trace diameter being much smaller than the particle size.

This Letter presents the results of investigation of the impact of a flux of microparticles in the SDP regime on an obstacle with a thickness below the maximum penetration depth, followed by penetration through the case of an integrated circuit (IC) placed behind the obstacle and action on the IC chip.

The flux of high-velocity particles formed as a result of the compressive action of detonation products on a cumulative lens filled with a nickel powder (particle size, 10–40 μm) [1, 2, 4]. The target comprised an assembled structure with a 200-mm-thick front wall, containing an IC in a metal-ceramic case. The IC was mounted so as to eliminate its impact on the container wall in the course of the target interaction with the impinging flux. The standard test characteristics of the IC were measured before and after experiment.

After exposure of the target to a flux of microparticles, the surface of the front wall exhibited only small and microscopic craters with the depth and diameter not exceeding 3 mm. The IC cases exhibited no visible mechanical damage. However, the measurements of standard electrical characteristics showed that 40–60% of these values fell out of the permitted range. Then, the IC case was removed and the IC chip surface was examined with the aid of an optical microscope and a scanning electron microscope. This investigation revealed point inclusions in the crystal (Fig. 2). Chemical analysis showed that these inclusions contain elements entering into compositions of the IC case and chip. The rear surface of the IC case also exhibited dark spots.

Analysis of the results of experiments described above led us to the following conclusions and suggestions.

(i) The fact of material penetration through the IC case confirms our previous assumption that the materials of projectile and obstacle escape from the rear side in the form of a microjet having a length of not less that the IC case thickness (≈200 μm), since the case could not be penetrated by a single particle (even with a diameter as small as the track width observed in the plastic foil, which was on the order of several microns).

(ii) The absence of any additional factors and conditions capable of substantially modifying the shape of the striker (microjet) emerging from an obstacle and entering (penetrating) into the foil suggests that the penetrant (consisting of the particle and obstacle materials) in the obstacle also has the form of a microjet.

(iii) Under certain conditions, the impact of a bunch of microparticles (e.g., micrometeorites occurring in the space and having definite density, velocity, and particle size corresponding to the SDP regime) on a space vehicle may result in penetration of the case wall and action on elements of the electronic equipment situated close to the wall. As demonstrated above, this may lead to equipment malfunction or even failure. The risk of such events increases due to a large amount of so-called "space spam" representing waste products of human activity in space [5].

REFERENCES

1. O. V. Roman, S. K. Andilevko, S. S. Karpenko, *et al.*, Inzh.-Fiz. Zh. **75** (4), 187 (2002).
2. O. A. Dybov, G. S. Romanov, and S. M. Usherenko, Inzh.-Fiz. Zh. **76** (5), 8 (2003).
3. O. A. Dybov, G. S. Romanov, and S. M. Usherenko, Inzh.-Fiz. Zh. **77** (1), 15 (2004).
4. S. K. Andilevko, S. S. Karpenko, and V. A. Shilkin, Pis'ma Zh. Tekh. Fiz. **25** (7), 69 (1999) [Tech. Phys. Lett. **25**, 280 (1999)].
5. L. S. Novikov, Inzh. Ékol., No. 4, 10 (1999).

Translated by P. Pozdeev

Technical Physics Letters, Vol. 31, No. 1, 2005, pp. 48–50. Translated from Pis'ma v Zhurnal Tekhnicheskoĭ Fiziki, Vol. 31, No. 2, 2005, pp. 6–12.

Efficiency of a Collective Action of Solid Projectiles upon an Obstacle at a Moderate Impact Velocity

É. É. Lin, S. K. Zhabitskiĭ, V. Yu. Mel'tsas, A. L. Mikhaĭlov, S. A. Novikov, A. L. Stadnik, and Yu. V. Yanilkin

Institute of Experimental Physics, Russian Federal Nuclear Center, Sarov, Russia

e-mail: root@gdd.vniief.ru

Received April 9, 2004; in final form, July 22, 2004

Abstract—The collective action of solid projectiles (steel spheres) on a duralumin obstacle was studied for an impact velocity on the order of 1 km/s. The experimentally observed fact that a group of spheres more effectively penetrates into obstacles than do separate spheres indicates that the solid projectiles exhibit mutual influence in the course of such a multiple impact. © *2005 Pleiades Publishing, Inc.*

Introduction. Increasing interest in the investigation of processes involved in a multiple impact of solid projectiles on an obstacle (see, e.g., [1–5]) is related to the ambiguity of notions about the efficiency and mechanisms of such interactions. A collective character of the interaction between an obstacle and a flux of solid macroscopic projectiles is most clearly manifested under conditions where the action of a single projectile is weak. In particular, this can take place at a moderate impact velocity, $U \ll U_*$, where U_* is a critical velocity above which the strength of the obstacle does not influence the character of its interaction with the projectile.

For an aluminum obstacle (U_* = 4000 m/s [2]) and iron (steel) projectiles, such moderate impact velocities occupy a narrow interval within U = 1000–2000 m/s, in which the empirical dependence of the z/d ratio (z is the penetration depth and d is the projectile diameter) on U [6] for the iron/aluminum combination exhibits characteristic bending. This behavior is related to fracture of the projectile material at high pressures and implies a sharp variation in the character of penetration into the obstacle for a single projectile. Therefore, this interval of impact velocities can be of interest for evaluating the efficiency of multiple impacts.

Experimental method and results. Impact velocities in the aforementioned interval can be obtained using an experimental scheme [7] based on the acceleration of steel spheres by the products of an explosion expanding in the channel of an evacuated shock tube after detonation of a flat explosive charge. The results of two-dimensional numerical calculations using the method described in [8] showed that this scheme can produce fluxes of like steel spheres moving with a velocity of 1100–2700 m/s, which depends on the charge thickness (Δ = 4–9 cm) and the sphere diameter (d = 2–6 mm).

In our experiments, nine steel spheres with a diameter of 5 mm (State Standard 3722–81: ball bearings) accelerated in the shock tube impinged on a duralumin (D16-T grade) target with a thickness of h = 15 or 100 mm. Using a pulsed X-ray setup, it was possible to observe the leading group of four to five spheres moving at a velocity of $U = 1400 \pm 100$ m/s and the lagging group with $U \approx 1100$ m/s. The sphere velocities were evaluated by comparing the results of X-ray monitoring of the sphere positions to the calculated curves. The time interval between the impacts of spheres from the leading group was estimated at $\Delta t \sim 10^{-6}$–10^{-5} s for two adjacent spheres; $\Delta t \sim 10^{-5}$ s for three closely spaced spheres; and $\Delta t \sim 10^{-4}$ s for the group of four to five spheres.

Collective impact under these conditions led to through perforation of a 15-mm-thick duralumin plate, in which we observed the groups of two or three "close" holes spaced 10–25 mm, and "distant" holes spaced 50–100 mm from each other. We have also found separate spheres embedded in the metal to a depth of about two sphere diameters (these spheres were most probably representing the lagging group).

In the experiments with a 100-mm-thick duralumin target (h/d = 20), we observed four spheres embedded to a depth of about 18 mm (z/d = 3.6), with their craters being spaced about 20 mm. One more crater was found close to these four, in which the sphere penetrated to a depth corresponding to about z/d = 2. According to the X-ray monitor data, this sphere lagged significantly behind the four leading spheres.

In a special experiment, a single steel sphere impinged on a 15-mm-thick duralumin plate at an impact velocity of $U = 1300 \pm 100$ m/s. In this case, we observed penetration to a relative depth of z/d = 2.2, which agrees (to within the experimental uncertainty of velocity determination) with the empirical dependence of the penetration depth on the impact velocity presented in [6].

Penetration to a relative depth of z/d = 3.6 observed for the group of four closely spaced spheres in the

1063-7850/05/3101-0048$26.00

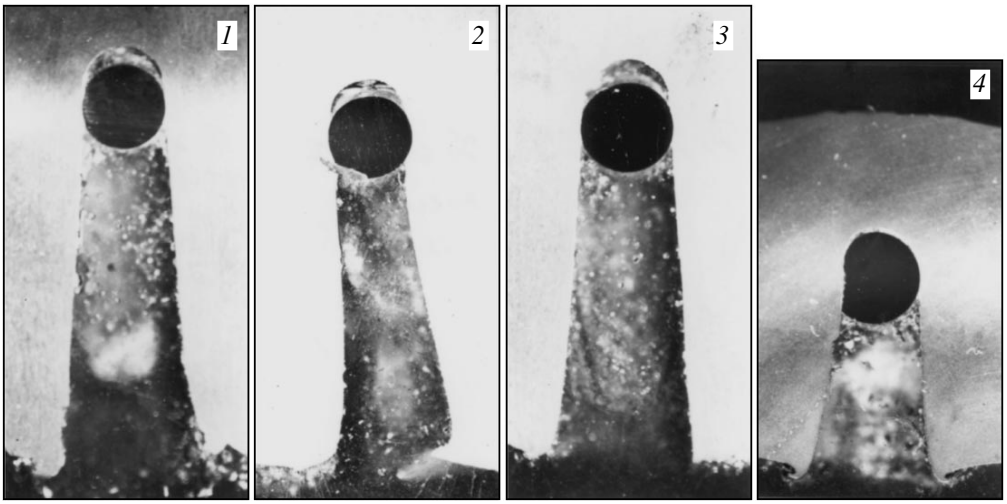

Fig. 1. The structure of craters formed in a thick duralumin target as a result of (*1*–*3*) multiple impacts of a group of steel spheres and (*4*) a single impact. The samples were sectioned strictly along the equatorial section of each sphere. The diameters of spheres after impact are (*1*) 4 mm, (*2*) 3.5 mm, and (*3*) 4 mm. The apparent relative penetration depth in the photographs exceeds the z/d value determined for the initial sphere diameter (d = 5 mm) and the crater depth (z_1 = 13 mm) measured from the front surface of the target to the sphere immediately upon impact. The real penetration depth is $z = z_1 + d$ = 18 mm and the relative penetration depth is z/d = 3.6.

"thick" duralumin target is about 1.6 times the value predicted by the aforementioned dependence [6], according to which the penetration depth of a single projectile for U = 1400 m/s is z/d = 2.3. This increase accounts for the observed multiple perforation of "thin" plates with a relative thickness of h/d = 3.

Metallographic examination of the targets revealed the following features. In the duralumin plate with h/d = 20, there was a gap between each sphere penetrating to a depth of z/d = 3.6 and the bottom of the crater. The width of this gap measured along the impact axis amounts to about 0.25d (Fig. 1). In the experiment with a single projectile, a gap between the front surface of the sphere and the bottom of the crater was about 0.05d, which is much lower as compared to the case on multiple impact. The front surfaces of embedded spheres retained duralumin layers with thicknesses on the order of 10 μm. All spheres exhibited cracks of various lengths (on the order of the sphere diameter) and a width of ~10^{-3} d, oriented approximately in the direction of impact. Near-surface layers of metal in the craters exhibit cracks and breaks. All cross sections of the duralumin samples showed traces of material melting in the region of embedded spheres. The spheres also showed evidence of partial surface fusion. In the targets with h/d = 3, the walls of through channels also exhibited a thin layer of fused duralumin. The surface of a steel sphere perforating the obstacle contained inclusions of fused duralumin.

Interpretation of results. The results of our experiments indicate that spheres exhibit mutual influence in the course of their interaction with the target. The distances between through holes and craters (ranging from 10 to 100 mm) correspond to the characteristic times of elastic wave propagation in the material $t_{el} \approx$ 2–20 μs (the effective velocity of sound in duralumin is about 5500 m/s [9]), and the characteristic times of plastic wave propagation $t_{pl} \approx$ 25–250 μs (for a plastic wave velocity of ≈400 m/s [10]). These values of t_{el} and t_{pl} are comparable with the time intervals Δt between separate impacts. This implies that the target material in the entire zone of impact features elastic and plastic waves. The interaction between these waves leads to a decrease in strength of the target material in local regions near the spheres. This is directly confirmed by the formation of a gap between each sphere and the bottom of the crater, which is more developed in the case of multiple impacts as compared to a single impact (Fig. 1).

According to [1, 5], a mechanism responsible for the local loss of stress can be related to liquefaction of the target material under the action of compression waves. This hypothesis is confirmed by the presence of fused duralumin on the bottom of the crater and on the walls. According to Khorev *et al.* [3, 4], another possible mechanism of the local loss of strength in the course of impact action can be related to the effective accumulation of damage at the defects initially present in the target material. This assumption is confirmed by the breaks observed in the material in front of stopped projectiles (and by the layer of duralumin on the front surface of the spheres in Fig. 1). We may also suggest that both these mechanisms can jointly operate in the localized regions of material near the spheres. This assumption does not contradict our experimental results.

The influence of the loss of material strength on the character of interaction between a steel sphere and an aluminum target was studied using a numerical method described in [11, 12] for the physical characteristics of the obstacle and projectile presented in [12]. It was

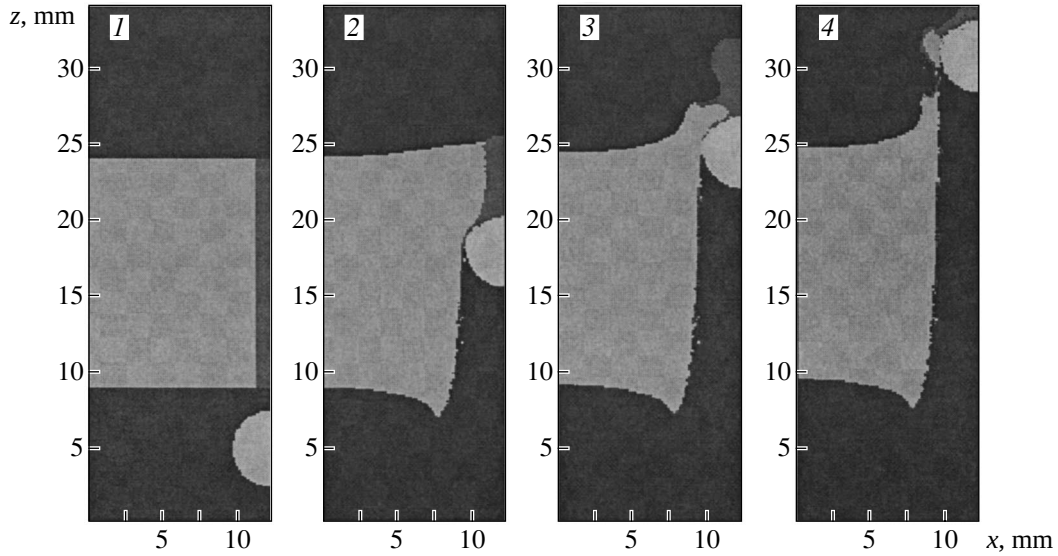

Fig. 2. Two-dimensional sections of the three-dimensional pattern of a duralumin obstacle perforated by a steel sphere observed at $t = 0$ (*1*), 15 (*2*), 30 (*3*), and 50 μs (*4*). The narrow channel at the axis of impact is characterized by a zero yield stress. The section at $x = 0$ corresponds to absolutely hard wall.

found that, for the impact parameters studied (h = 15 mm, d = 5 mm, U = 1300 m/s), a single sphere is stopped in the obstacle over a range of 12 mm, provided that the stopping medium does not lose strength and continuity. The calculated penetration depth agrees with the aforementioned empirical relation [6] for the given combination of projectile (iron) and target (aluminum) materials. Simultaneous impact of many spheres periodically arranged in the impact plane was modeled by introducing absolutely hard walls parallel to the axis of impact. Nonsimultaneous (delayed) impact was simulated by setting free boundaries at a certain distance from the axis of impact. The local loss of strength in the continuous medium was modeled by setting a yield stress equal to zero in a narrow channel along the impact axis. Use of this simplified approach is related to a rapid accumulation of damage in impact-loaded materials with a phonon excitation lifetime on the order of $\sim 10^{13}$ s. The results of numerical simulation showed perforation of the obstacle takes place both in the presence of absolutely hard walls (Fig. 2) and in the system with free boundaries. Therefore, the synchronism of multiple impacts is not very significant in the case of the local loss of strength.

Thus, we have established the increased efficiency of a collective impact of solid projectiles on an obstacle at a moderate impact velocity. Elucidation of the mechanism responsible for the local loss of strength in a material under such conditions requires further investigation.

Acknowledgments. The authors are grateful to A.V. Gladtsinov, Yu.M. Makarov, G.F. Portnyagin, S.V. Prokhorov, and N.A. Yukina for their help in carrying out this investigation.

This study was performed within the framework of Contract No. B526446 with the Lawrence Livermore National Laboratory (USA).

REFERENCES

1. S. N. Buravova, Pis'ma Zh. Tekh. Fiz. **15** (17), 63 (1989) [Sov. Tech. Phys. Lett. **15**, 689 (1989)].
2. V. M. Fomin, A. I. Gulidov, and G. A. Sapozhnikov, *High-Speed Interaction of Solids* (SO RAN, Novosibirsk, 1999) [in Russian].
3. I. E. Khorev, S. A. Zelepugin, A. A. Konyaev, *et al.*, Dokl. Akad. Nauk **369**, 481 (1999) [Dokl. Phys. **44**, 818 (1999)].
4. I. E. Khorev, V. K. Yakushev, S. A. Zelepugin, *et al.*, Dokl. Akad. Nauk **389**, 197 (2003) [Dokl. Phys. **48**, 146 (2003)].
5. O. V. Roman, S. K. Andilevko, S. S. Karpenko, *et al.*, Inzh.-Fiz. Zh. **75** (4), 187 (2002).
6. J. A. Zukas, T. Nicholas, H. F. Swift, *et al.*, *Impact Dynamics*, Ed. by J. A. Zukas (Wiley, New York, 1982).
7. E. E. Lin, V. Yu. Mel'tsas, S. A. Novikov, *et al.*, Khim. Fiz. **17**, 97 (1998).
8. S. K. Godunov, A. V. Zabrodin, M. Ya. Ivanov, *et al.*, *Numerical Solution of Multidimensional Problems of Gasdynamics* (Nauka, Moscow, 1976) [in Russian].
9. A. P. Babichev, N. A. Babushkina, A. M. Bratkovskiĭ, *et al.*, *Handbook of Physical Quantities*, Ed. by I. S. Grigoriev and E. Z. Meilikhov (Énergoatomizdat, Moscow, 1991; CRC Press, Boca Raton, 1997).
10. L. E. Kolegov, E. E. Lin, V. T. Ryazanov, and A. I. Funtikov, Prikl. Mekh. Tekh. Fiz., No. 6, 93 (1991).
11. A. L. Stadnik, V. I. Tarasov, and Yu. V. Yanilkin, Vopr. At. Nauki Tekh., Ser.: Mat. Model. Fiz. Protsessov, No. 3, 52 (1995).
12. E. E. Lin, V. Yu. Mel'tsas, A. L. Stadnik, and Yu. V. Yanilkin, Pis'ma Zh. Tekh. Fiz. **28** (17), 90 (2002) [Tech. Phys. Lett. **28**, 750 (2002)].

Translated by P. Pozdeev

Technical Physics Letters, Vol. 31, No. 1, 2005, pp. 51–54. Translated from Pis'ma v Zhurnal Tekhnicheskoĭ Fiziki, Vol. 31, No. 2, 2005, pp. 13–21.

Electron Structure and Elemental Composition of Thin Films of Europium Deposited at Room Temperature on a Si(100)2 × 1 Surface

A. Yu. Varykhalov[a], M. V. Kuzmin[b], and M. A. Mittsev[b,*]

[a] *BESSY, D-12489 Berlin, Germany*

[b] *Ioffe Physicotechnical Institute, Russian Academy of Sciences, St. Petersburg, 194021 Russia*

* *e-mail: m.mittsev@mail.ioffe.ru*

Received July 13, 2004

Abstract—Thin-film Eu–Si(100) structures formed by vacuum deposition of europium at room temperature onto a single crystal silicon surface were studied by method of photoelectron spectroscopy (PES) using synchrotron radiation. Analysis of the PES data showed that adsorption of even a small amount of metal (θ = 0.2 monolayer) leads to destruction of the surface dimers existing on the initial (2 × 1)-reconstructed Si(100) surface. The results of PES measurements, together with the structural data, indicate that deposition of europium is accompanied by the formation of a disordered metal film containing dissolved Si atoms. The concentration of silicon in the film decreases with the distance from the Eu–Si interface. Photoelectron spectra of the Si 2*p* core level of dissolved Si atoms are shifted toward lower binding energies as compared to the analogous spectra of clean silicon surface. This shift is due to the charge transfer from electropositive Eu atoms to electronegative Si atoms. © *2005 Pleiades Publishing, Inc.*

In recent years, considerable attention has been devoted to the investigation of thin-film structures obtained by deposition of rare earth metals onto single crystal silicon surface. This Letter reports on the electron properties and elemental composition of thin-film structures formed in the course of vacuum deposition of europium onto (2 × 1)-reconstructed Si(100) at room temperature (T = 300 K).

A special feature of europium, distinguishing this element among other rare earths, is that Eu atoms are divalent in the metallic state. In addition, europium is characterized by very high chemical activity. Both these factors may influence the growth mechanism and the properties of films formed in the course of europium deposition in vacuum at room temperature. The formation of silicides under such conditions is unlikely. To our knowledge, no such experiments have been reported so far.

The experiments were performed using a photoelectron spectrometer and a synchrotron radiation channel of the Russian-German Laboratory at the BESSY II storage ring (Berlin, Germany). The overall energy resolution of the instrumentation employed was 150 meV. The photoelectron spectra were excited by synchrotron radiation with a primary photon energy of $h\nu$ = 130 eV, which allowed us to study the Si 2*p* core levels, the valence band of silicon and the Eu 4*f* level. The state of the sample surface and the structure of surface films formed in the course of europium deposition were monitored by low-electron energy diffraction (LEED).

The samples were prepared using *n*-type single crystal silicon plates with a resistivity of about 1 Ω cm. Prior to experiments, the plates were heated in a vacuum chamber of the photoelectron spectrometer, first for 2 h at 900°C and then for a short time at 1450°C. This treatment ensured obtaining an atomically clean Si(100)2 × 1 reconstructed surface. The residual pressure in the spectrometer chamber during europium deposition did not exceed 2×10^{-9} mbar. The rate of deposition was typically 0.013 monolayers (ML) per second (1-ML coverage of Eu atoms corresponds to their surface density of 6.78×10^{14} cm^{-2}, which equals the density of silicon atoms on the Si(100) surface). The PES measurements were performed at room temperature in a vacuum of 3×10^{-10} mbar.

The typical photoelectron spectra observed for the Eu–Si(100) system studied are presented in Fig. 1, where the spectrum is normalized to the maximum peak height. As can be seen from Fig. 1a, deposition of even a very small amount of Eu atoms (see the spectrum for a surface coverage of θ = 0.2) leads to a decrease in manifestation of the feature (S_U) related to the asymmetric surface dimers of silicon [1, 2]. This fact indicates that adsorbed metal atoms destroy these dimers. As the metal coverage increases further, an extended wing is formed instead of the S_U feature. At θ = 6.5, this wing transforms into a clearly distinguished long step. When the metal coverage reaches θ = 10, the signals characteristic of the clean silicon surface almost completely disappear and the step transforms into two narrow peaks, which are shifted

1063-7850/05/3101-0051$26.00

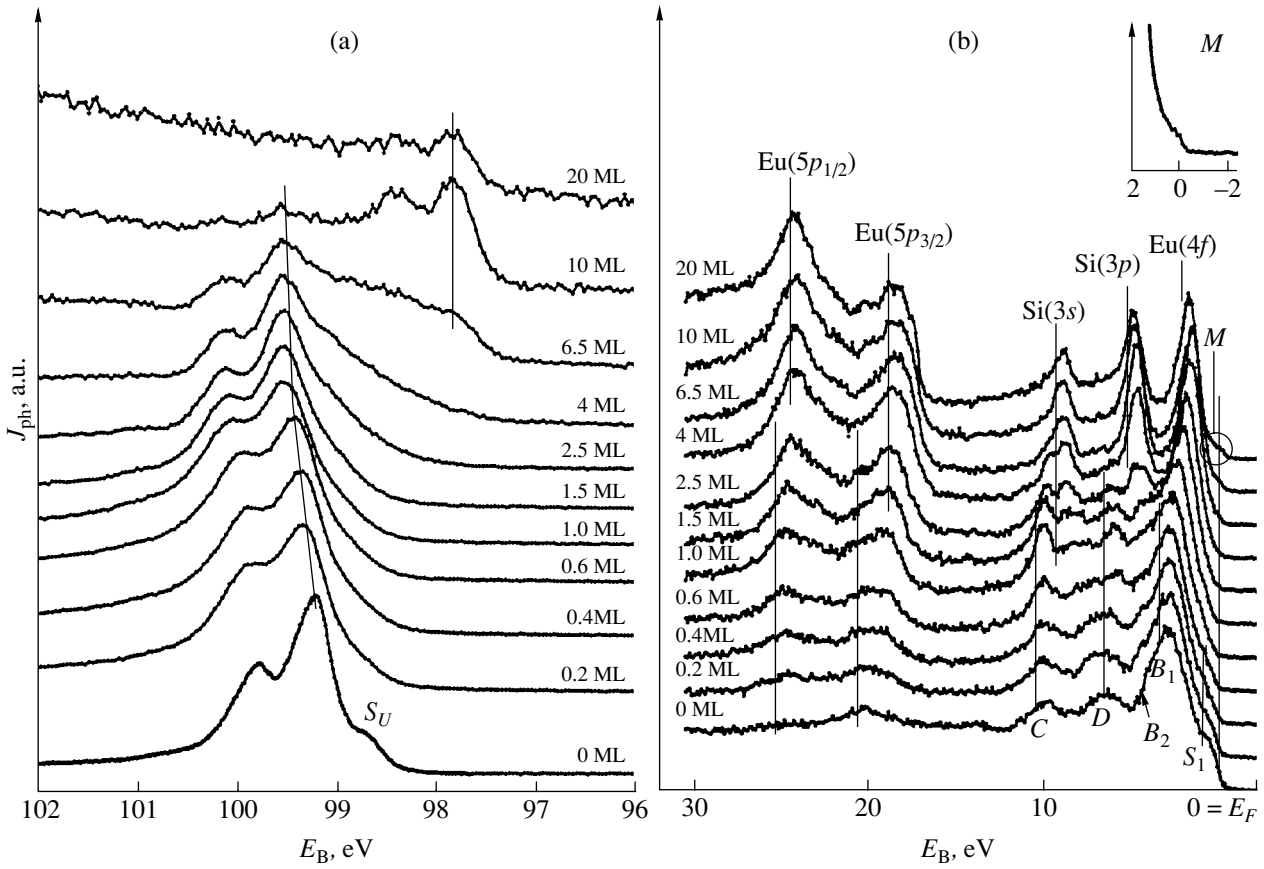

Fig. 1. Normalized photoelectron spectra of (a) the Si 2*p* level and (b) the valence band of silicon and the Eu 4*f* level in the Eu–Si(100) system for various europium coverages (indicated at the curves in ML units). The spectra were excited using synchrotron radiation with a photon energy of $h\nu$ = 130 eV.

by 1.39 eV toward lower binding energies E_B relative to the signals observed for the initial clean surface. The distance between the two peaks is the same as that for the clean silicon surface.

This pattern of evolution of the photoelectron spectra of the Si 2*p* core level of silicon can be convincingly interpreted assuming that

(a) no surface silicide formation takes place at T = 300 K;

(b) Si atoms diffuse into the growing metal film;

(c) the charge is transferred from electropositive Eu atoms to electronegative Si atoms, which decreases the binding energy of electrons populating the Si 2*p* level.

Based on these assumptions, the formation of a structureless wing and its transformation into a structureless step is reasonably explained by taking into account that (in the corresponding regions of surface coverage) the Si 2*p* spectrum contains the signals both from Si atoms occurring in the crystal lattice and from those interacting with Eu atoms at the substrate–film interface and in the volume of the metal film. Apparently, the aforementioned charge transfer will be manifested by a shift of the signals from Si atoms at the interface and in the film volume toward lower binding energies as compared to the values for the clean silicon surface. Since the state of Si atoms at the substrate–film interface differs from that in the volume of the metal film, the shift for the two groups will be different. Moreover, the shift may also vary inside each of these groups. This will take place, for example, when the film of Eu atoms is disordered. If the number of various states in which Si atoms may occur is sufficiently large and the maximum scatter of E_B exceeds the spin–orbit splitting for Si 2*p* level (0.6 eV), the photoelectron spectrum will exhibit a structureless feature (a wing or a step) shifted toward lower binding energies relative to the signals observed for the clean surface.

The results of structural investigations performed within the framework of this study showed that europium deposition onto Si(100)2 × 1 surface at 300 K leads at all coverages to the formation of films lacking, at least, a long-range order. This confirms the validity of the above considerations. Analysis of the obtained photoelectron spectra of Si 2*p* level allows us to judge qualitatively the variation of the state of dissolved Si atoms occurring in various layers of the metal film. This judgment can be based on a comparison of the photoelectron spectra obtained for small and large surface coverages (see Fig. 1a). At large coverages (θ = 10 and

20 ML), the spectra display (in contrast to the case of small θ) only two well resolved maxima belonging to the dissolved Si atoms. This character of the signals indicates that they come from Si atoms occurring in approximately equivalent positions. Since the Si atoms occurring at the interface and in the adjacent layer make no (or very small) contribution to the spectrum observed for θ = 10 and 20, we may conclude that the broadest spectrum of states of Si atoms is just characteristic of the interface and the adjacent layer of the film. Silicon atoms occurring in the film layers distant from the interface occupy more or less equivalent positions.

The spectra presented in Fig. 1a show that the intensity of signals from Si atoms dissolved in the metal film decreases with increasing film thickness. This behavior indicates that the concentration of such atoms decreases with increasing distance from the interface.

Conclusions derived from analysis of the photoelectron spectra of the Si 2*p* core levels are generally confirmed by the valence-band spectra of silicon and the spectra of the Eu 4*f* level, which are presented in Fig. 1b. The spectrum of the clean surface of silicon coincides with that reported in [3] for the same photon energy. Deposition of even the first doses of Eu atoms leads to vanishing of the S_1 feature (spectral features of the clean silicon surface are denoted as in [3]) attributed to the surface dimers. As the Eu coverage increases in the interval 1 ML < θ < 6.5 ML, the main maximum B_1 shifts toward lower E_B values. At θ ≥ 6.5 ML, this maximum is observed at E_B = 2.1 eV, which coincides with the value obtained [4–7] for metallic europium. In addition, the entire part of the spectrum within E_B = 0–4 eV for these coverages coincides with the spectra reported in [4–7]. This is valid, in particular, for a feature (depicted on a greater scale in the inset to Fig. 1b) crossing the Fermi level. This result indicates that occupied states at the Fermi level appear only at θ ≥ 6.5 ML. All these facts indicate the following: First, the photoelectron spectra presented in Fig. 1b for θ ≥ 6.5 ML represent in the $0 < E_B < 0$–4 eV interval the spectra of the Eu 4*f* level. From this we infer that, in the given range of coverages, this signal of the 4Eu *f* level exceeds the signal from silicon. Second, the obtained results indicate that the deposited Eu film acquired metallic character only for θ ≥ 6.5 ML.

The spectra presented in Fig. 1b also exhibit certain evolution in the regions of E_B = 4–11 and 15–30 eV. In the first of these regions, two peaks with the maxima at 5.1 and 9.1 eV begin to grow with increasing coverage for θ ≥ 4 and then decrease. Since the work function of europium films deposited at 300 K is about 2.9 eV, the binding energies of these peaks relative to the vacuum level are approximately 8.1 and 12.1 eV. These values are close to the binding energies of electrons populating the 3*p* and 3*s* levels of free Si atoms (8.15 and 13.46 eV, respectively [8]). This, together with the character of variation of the peak amplitudes with increasing coverage, allow us to suggest that (i) these signals reflect the photoionization of 3*p* and 3*s* levels of Si atoms dissolved in the metal film and (ii) no silicide formation takes pace. The difference between the binding energies of electrons populating the 3*p* and 3*s* levels of dissolved and free Si atoms is related to the charge transfer from Eu to Si atoms in the films.

Slow decay of the intensity of peaks at E_B = 5.1 and 9.1 eV with increasing θ in the region of large coverages is probably related to the fact that the mean free path λ of electrons with a kinetic energy of E_k = 130 eV in metallic europium is very large and exceeds the value according to the universal dependence of λ on E_k. This conclusion is apparently at variance with the behavior of Si 2*p* spectra. Indeed, these spectra measured at θ = 20 ML (as well as the corresponding spectra in Fig. 1b) exhibit maxima corresponding to Si atoms dissolved in europium. However, the heights of these peaks are much smaller as compared to those caused by photoionization of the Si 2*s* and 2*p* levels, despite the fact that the photoionization cross section for the Si 2*p* is approximately 50 times the values for the two other levels [9]. The discrepancy is removed if we assume that (in contrast to the universal $\lambda(E_k)$ function) the electron mean free path at E_k = 30 eV (for which the Si 2*p* spectra of dissolved Si atoms are measured) is significantly shorter than that for E_k = 130 eV. This assumption, as well as the expected very large value of λ at E_k = 130 eV are confirmed by the data of Gerken *et al.* [10], according to which λ(130 eV) equals to approximately five thicknesses *a* of the europium film. This yields λ(130 eV) ≅ 20 Å for the atomic radius of Eu in the metallic state *r* = 2.20 Å [11]; at the same time, the electron mean free path at E_k = 30 eV is λ(30 eV) = 2.5*a* ≅ 10 Å.

In the region of binding energies from 15 to 30 eV, the spectra observed for θ ≥ 1 ML exhibit two peaks with E_B = 18.7 and 24.5 eV. These values agree well with analogous data reported by Riviere *et al.* [12] for the $5p_{3/2}$ (18.9 eV) and $5p_{1/2}$ (24.5 eV) levels of Eu in the metallic state. This coincidence provides additional evidence for the absence of silicide formation at *T* = 300 K, that is, for the formation of a metallic film under the europium deposition conditions studied.

To summarize, the results of our investigation show that adsorption of even a small amount of metal (θ = 0.2 ML) leads to destruction of the asymmetric surface dimers existing on the initial (2 × 1)-reconstructed Si(100) surface. The results of PES measurements, together with the structural data, indicate that deposition of europium is accompanied by the formation of a disordered metal film containing dissolved Si atoms. The concentration of silicon in the film decreases with the distance from the Eu–Si interface. Photoelectron spectra of the Si 2*p* core level of dissolved Si atoms are shifted toward lower binding energies as compared to the analogous spectra of the clean silicon surface. This

shift is due to the charge transfer from electropositive Eu atoms to electronegative Si atoms.

Acknowledgments. The work was supported by the Ministry of Industry, Science, and Technology of the Russian Federation (project no. 40.012.1.1.1152) and by the Russian–German Laboratory at BESSY II (Berlin, Germany).

REFERENCES

1. C.-P. Cheng, I.-H. Hong, and T.-W. Pi, Phys. Rev. B **58**, 4066 (1998).
2. K. Nakamura, H. W. Yeom, H. Koh, *et al.*, Phys. Rev. B **65**, 165332 (2002).
3. J. M. Gallego, J. M. Garcia, J. Alvares, and R. Miranda, Phys. Rev. B **46**, 13339 (1992).
4. R. Kammerer, J. Barth, F. Gerken, *et al.*, Solid State Commun. **41**, 435 (1982).
5. F. Gerken, A. S. Flodström, J. Barth, *et al.*, Phys. Scr. **32**, 43 (1985).
6. C. G. Olson, X. Wu, Z. L. Chen, *et al.*, Phys. Rev. Lett. **74**, 992 (1995).
7. R. Wahl, W. Schneider, S. L. Molodtsov, *et al.*, Phys. Rev. Lett. **82**, 670 (1999).
8. T. A. Carlson, *Photoelectron and Auger Spectroscopy* (Plenum Press, New York, 1975; Mashinostroenie, Leningrad, 1981).
9. J. J. Yeh and I. Lindau, At. Data Nucl. Data Tables **32**, 1 (1985).
10. F. Gerken, J. Barth, R. Kammerer, *et al.*, Surf. Sci. **117**, 468 (1982).
11. *Properties of Elements*, Part 1: *Physical Properties*, Ed. by G. V. Samsonov (Metallurgiya, Moscow, 1976) [in Russian].
12. J. C. Riviere, F. P. Netzer, G. Rosina, *et al.*, J. Electron Spectrosc. Relat. Phenom. **36**, 331 (1985).

Translated by P. Pozdeev

Technical Physics Letters, Vol. 31, No. 1, 2005, pp. 55–57. Translated from Pis'ma v Zhurnal Tekhnicheskoĭ Fiziki, Vol. 31, No. 2, 2005, pp. 22–26.

The Current of an Annular Electron Beam Behind Virtual Cathode

S. Ya. Belomyttsev, A. A. Grishkov, S. A. Kitsanov, S. D. Korovin, S. D. Polevin, and V. V. Ryzhov*

Institute of High-Current Electronics, Siberian Division, Russian Academy of Sciences, Tomsk, Russia

** e-mail: ryzhov@to.hcei.tsc.ru*

Received August 13, 2004

Abstract—The output current I_{out} of a magnetized annular electron beam transported in a homogeneous drift tube of a SINUS-7 setup has been studied as a function of the injected beam current I_{inj}. The electron beam was injected via an anode inset of smaller radius and had a current above the Fedosov limit for the given drift tube ($I_{inj} \geq I_F$). It is established that, to within the experimental uncertainty, a virtual cathode (VC) is formed when the injected beam current exceeds the corresponding limiting I_{lim}. In this state, the current transmitted behind VC is approximately equal to the limiting value ($I_{out} \approx I_{lim}$). © *2005 Pleiades Publishing, Inc.*

It is well known that, when an electron beam is transported via a planar gap and the injected beam current (I_{inj}) exceeds the second critical level ($I_{inj} = I_{lim} = I_{2crit}$), a virtual cathode (VC) is formed in the gap, after which the output current behind the VC exhibits a jumplike decrease. Thus, the output current of an electron beam transported via a flat gap in the presence of a VC is always smaller than the limiting value: $I_{out} < I_{lim}$.

It was ascertained [1, 2] that an analogous situation must take place when a magnetized annular electron beam is transported in a cylindrical drift tube. At the same time, copious data obtained by numerical modeling of electron beams transported in composite drift tubes and the results of theoretical investigations reject this analogy [3–5]. In order to elucidate this question, we have performed experiments and measured of the current behind the VC for an annular electron beam transported in a cylindrical drift tube. The aim of these measurements was to compare relative variations of the electron beam current in the drift tube in the presence of a VC and in the regime of total current transmission.

The experiments were performed on a high-current electron accelerator SINUS-7 [6] with a cathode voltage of up to 2 MV, a diode current of up to 20 kA, and a current pulse duration of 50 ns. The experimental geometry is depicted in Fig. 1. The electron beam was generated in a coaxial vacuum diode with magnetic isolation and injected via an anode insert into the drift tube. Electrons were emitted from a cylindrical graphite explosive-emission cathode with a radius of $R_C \approx 8.5$ mm and a ridge width of 0.5 mm. In order to provide the formation of a thin-walled annular electron beam, the strength of a homogeneous longitudinal magnetic field in the region of beam formation and in the drift tube had to be sufficiently high (~15 kOe). The anode insert had a length of 55 mm and a channel radius of 12 mm.

The length of the drift tube in our experiments was fixed at $L_{dr} \approx 250$ mm and significantly exceeded the tube radius $R_A \approx 43$ mm. The anode radius in the coaxial vacuum diode was also 43 mm. The diode current was controlled by varying the distance from the cathode to the anode insert ($L_{A–C}$), while the cathode voltage was maintained at a constant level. The beam current in the diode and in the drift space was measured using low-inductance ohmic shunts.

Figure 2 shows the typical oscillograms of the cathode voltage and the beam current in the drift tube. As can be seen, variation of both the cathode voltage and the beam current during the pulse are rather insignificant.

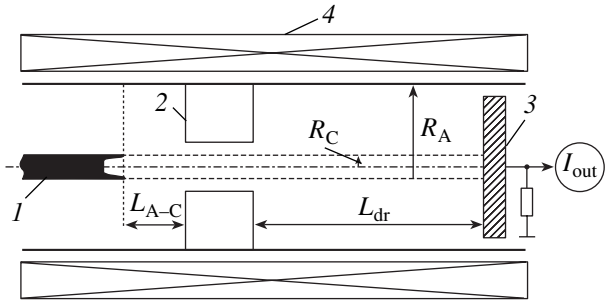

Fig. 1. Schematic diagram of experimental geometry: (*1*) cathode; (*2*) anode insert; (*3*) collector; (*4*) solenoid.

1063-7850/05/3101-0055$26.00 © 2005 Pleiades Publishing, Inc.

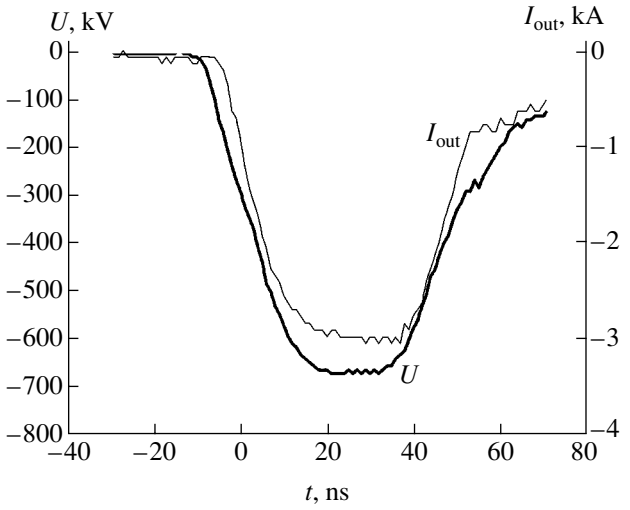

Fig. 2. The typical oscillograms of the cathode voltage and the beam current in the drift tube.

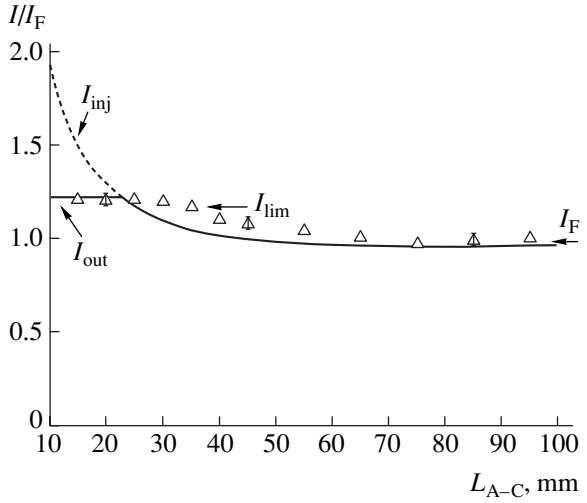

Fig. 3. Plot of the relative current I/I_F in the drift space versus anode–cathode distance $L_{A–C}$: solid curve presents the results of numerical simulation performed using the PIC code KARAT; dashed curve shows the calculated injected current; symbols show the results of experiments on the SINUS-7 setup.

Figure 3 presents an experimental plot of the relative current in the drift space versus anode–cathode distance $L_{A–C}$ measured at a cathode voltage of about 700 kV. For comparison, Fig. 3 also shows the results of numerical simulation performed using the PIC code KARAT [7] for the coaxial vacuum diode and the drift tube geometry analogous to that used in our experiments.

For large anode–cathode distances ($L_{A–C}$ > 60–70 mm), the beam current I_{out} behind the VC was equal to the injected current and could be determined using a formula of the Fedosov current

$$I_F = \frac{I_0}{2\ln(R_C/R_A)}\frac{(\Gamma-\gamma_F)\sqrt{\gamma_F^2-1}}{\gamma_F}, \qquad (1)$$

where $I_0 = mc^3/e$, $\Gamma = 1 + eU/mc^2$, m is the electron mass, e is the electron charge, c is the velocity of light in vacuum, U is the electrostatic potential of the anode tube, and $\gamma_F = -0.5 + \sqrt{2\Gamma + 0.25}$ is the relativistic factor for a beam with the Fedosov current, which was determined for a thin-walled beam in coaxial vacuum diode with magnetic isolation [8].

As the gap width $L_{A–C}$ decreases, the beam current smoothly grows to the limiting value

$$I_{lim} = \frac{I_0}{2\ln(R_C/R_A)}(\Gamma^{2/3}-1)^{3/2} \qquad (2)$$

and then (after VC formation) remains constant.

In the experiment, the VC formation was manifested by high-frequency oscillations observed in oscillograms of the cathode voltage and the beam current in the drift tube. The spectrum of these oscillations was rather broad, extending from 1 to 3 GHz. The time interval of averaging was about 3 ns. The ratio of the limiting current to the Fedosov current obtained in our experiments was $I_{lim}/I_F \approx 1.23$. The values of these currents calculated for an electron energy of 700 keV in an infinitely long drift tube are $I_{lim} \approx 3.7$ kA and $I_F \approx 2.9$ kA, which yields ≈1.28.

It should be noted that, according to the results of numerical simulation, the VC is formed at $L^{cr}_{A–C} \approx 20$ mm. In our experiments, this critical distance was $L^{cr}_{A–C} \approx 30$ mm. The difference can be explained by a decrease in the effective gap width as a result of the motion of a cathode plasma along the magnetic field, which was not taken into account in the numerical simulation. Experiments [9] showed that the velocity of motion of the cathode plasma boundary at a megavolt cathode voltage may reach $(2–3) \times 10^7$ cm/s. Under our experimental conditions, a decrease in the effective gap width $L_{A–C}$ during the current pulse may reach ~1 cm.

The results of our experiments showed that the annular electron beam in a cylindrical drift tube may occur in two states, with and without VC. In the state without VC, the transmitted current is equal to the injected current and smoothly varies from I_F to the limiting transport current I_{lim}, after which a VC is formed. When the injected beam current is increased further, the transmitted current is approximately equal to the limiting value ($I_{out} \approx I_{lim}$).

Acknowledgments. This study was supported by the Russian Foundation for Basic Research (project no. 04-02-16527a).

REFERENCES

1. N. F. Kovalev and M. I. Fuks, Preprint No. 13 (Institute of Applied Physics, Gorki, 1980).
2. N. F. Kovalev, Zh. Tekh. Fiz. **72** (7), 113 (2002) [Tech. Phys. **47**, 906 (2002)].
3. A. E. Dubinov and I. E. Efimova, Zh. Tekh. Fiz. **71** (6), 80 (2001) [Tech. Phys. **46**, 723 (2001)].
4. A. M. Ignatov and V. P. Tarakanov, Phys. Plasmas **1**, 741 (1994).
5. S. Ya. Belomyttsev, A. A. Grishkov, S. D. Korovin, and V. V. Ryzhov, Pis'ma Zh. Tekh. Fiz. **29** (16), 16 (2003) [Tech. Phys. Lett. **29**, 944 (2003)].
6. S. D. Korovin and V. V. Rostov, Izv. Vyssh. Uchebn. Zaved., Fiz., No. 12, 21 (1996).
7. V. P. Tarakanov, *User's Manual for Code KARAT* (Berkley, Springfield, 1992).
8. A. I. Fedosov, E. A. Litvinov, S. Ya. Belomyttsev, and S. P. Bugaev, Izv. Vyssh. Uchebn. Zaved., Fiz., No. 10, 134 (1977).
9. S. P. Bugaev, N. I. Zaitsev, A. A. Kim, *et al.*, in *Relativistic Microwave Electronics (Proceedings of the 2nd All-Union Seminar)* (IPM, Gorki, 1981), pp. 36–61.

Translated by P. Pozdeev

Technical Physics Letters, Vol. 31, No. 1, 2005, pp. 58–60. Translated from Pis'ma v Zhurnal Tekhnicheskoĭ Fiziki, Vol. 31, No. 2, 2005, pp. 27–33.

Interface Characteristics and Mechanisms of Current Transfer in Metal–Tunnel-Thin Rare Earth Fluoride–Silicon Structures

M. B. Shalimova* and N. V. Shcherbakova

Samara State University, Samara, Russia

** e-mail: rozhkov@ssu.samara.ru*

Received July 1, 2004

Abstract—We have studied the electrical properties of metal–tunnel-thin insulator–silicon (MIS) structures with dysprosium, cerium and neodymium fluorides as insulating layers. The characteristics of interfaces (energy distributions of the density of surface states, surface potential) were determined and mechanisms of the current transfer in these MIS structures were studied. *© 2005 Pleiades Publishing, Inc.*

The need for new insulating materials exhibiting high permittivity stimulates the search for and characterization of promising dielectric compounds possessing various useful properties. Promising compounds suitable for the formation of insulating layers are offered by the class of rare earth (RE) fluorides, which are characterized by sufficiently high permittivities (ε_D = 8–14) and resistivities ($\rho = 10^{12}$–10^{13} Ω cm), exhibit high chemical and thermal stability, and are resistant to radiation.

This Letter presents the results of investigation of the characteristics of interfaces in metal–insulator–silicon (MIS) structures involving tunnel-thin layers of RE fluorides (RE = Ce, Dy, Nd) and the mechanisms of current transfer in MIS diodes based on such structures.

MIS diodes were obtained by means of electric modification of the initial MIS structures with thin insulating layers. The method of electric modification is based on the phenomenon of conductivity switching in RE fluorides under the action of a strong electric field [1]. As a result of this treatment, a local inhomogeneous region with high conductivity and an area of $A \sim 3$–80 μm^2 is created in the insulating layer.

The samples were prepared by vacuum deposition of a layer of RE fluoride (RE = Ce, Dy, Nd) with a thickness of 0.3–0.4 μm onto *n*- or *p*-type single crystal silicon substrates (with a resistivity of 5 or 4.5 Ω cm, respectively). Then, metal electrodes with a diameter of 0.5–0.7 mm were formed by vacuum deposition of aluminum onto RE fluoride films. Application of an electric field with a strength of ~10^8 V/m leads to the formation of a local conducting channel in the initial RE fluoride film. It was found that this channel consists predominantly of a metal phase. In the region of this channel, a tunnel-thin insulating layer with a thickness of d_t = 1–3 nm is also formed, provided that a sufficiently large load resistor (R > 1.5 kΩ) is connected in series with the sample structure. Using this method, we obtained Al–CeF_3–Si, Al–DyF_3, and Al–NdF_3–Si structures with tunnel-thin insulating RE fluoride layers.

Our investigations showed that, in the absence of applied voltage, the semiconductor surface in all MIS structures occurs in a state depleted of the majority charge carriers. The forward-bias dc current–voltage characteristics of the samples exhibit three characteristic regions:

(i) The region of semiconductor-limited current (region I), which corresponds to bias voltages $U < \varphi_{s0}$. In this region, the current J through the structure is determined by the overbarrier injection of majority carriers from semiconductor to metal and obeys exponential dependence on the applied bias voltage,

$$J = \overline{D_{n,p}} A^* T^2 A \exp\left(-\frac{q\Phi_b}{kT}\right)\exp\left(\frac{qU}{nkT}\right), \qquad (1)$$

where $\Phi_b = \varphi_{s0} + (E_c - F)$ for the *n*-type semiconductor, $\overline{D_{n,p}}$ is the tunnel transmission coefficient for electrons (holes), A^* is the Richardson constant, A is the junction area, n is the nonideality factor, k is the Boltzmann constant, T is the absolute temperature, q is the electron charge, E_c is the conduction band bottom, and F is the Fermi level. In this study, we assumed that the tunnel transmission coefficient is constant in the range of bias voltages studied.

Figure 1 shows the experimental current–voltage (J–U) characteristics of forward-biased MIS structures, which are well approximated by exponents in region I.

(ii) The region of currents limited by the tunneling conductivity of the insulator (region II), which corresponds to bias voltages $\varphi_{s0} < U < 1.2$ V. In this region, the current in the forward-biased MIS structure is deter-

mined by the tunneling of majority carriers from semiconductor to metal and obeys the relation,

$$J \cong B(U - \varphi_{s0})^2, \tag{2}$$

where B is a constant factor. The observed quadratic dependence of the current on U–φ_{s0} is related to the fact that the density of the tunneling current from the metal to the conduction band of the semiconductor can be described in the approximation of noninteracting electrons as [2]

$$j_{nT} = \frac{1}{4} q V_n \overline{D}_n N_c [F_1(y_g - y_s) - F_1(-y_s)]. \tag{3}$$

Here, $y_g = qU/kT$ is the dimensionless voltage across the gate, $y_s = qU_s/kT$ is the surface potential, V_n is the average thermal velocity of electrons, N_c is the effective density of states in the conduction band of the semiconductor, and $F_1(y)$ is the Fermi integral. In the region of bias voltages such that $|y_g - y_s| > 3$, the integrals in expression (3) can be replaced by polynomials [3], which yields

$$j_{nT} = \frac{1}{4} q V_n \overline{D}_n N_c \frac{(y_g - y_s)^2}{2}. \tag{4}$$

Expressions (3) and (4) are valid when tunneling is the dominant mechanism of current transfer in the MIS structure for both electrons and holes.

In Fig. 1, the current–voltage characteristics are also plotted in the coordinates of $\sqrt{J}$ versus U. In region II, the experimental data are well approximated by straight lines; extrapolation of these lines to zero current gives the values of φ_{s0}.

(iii) For the bias voltages $U > 1.2$ V (region III), the forward current is limited predominantly by the spreading resistance of the semiconductor substrate.

The surface potential as a function of the bias voltage for $U \le U_0 - 2kT/q$ (where U_0 is the flat band potential) was calculated using the formula

$$\varphi_s(U) = \frac{kT}{q} \ln\left[\frac{A^* A T^2}{J(U)}\right] - \frac{E_c - F}{q}. \tag{5}$$

The results of calculations showed that φ_s in most MIS diodes studied is proportional to U and can described by the relation [4]

$$|\varphi_s(U)| \cong \frac{U_0 - U}{b} = |\varphi_{s0}| - \frac{U}{b}, \tag{6}$$

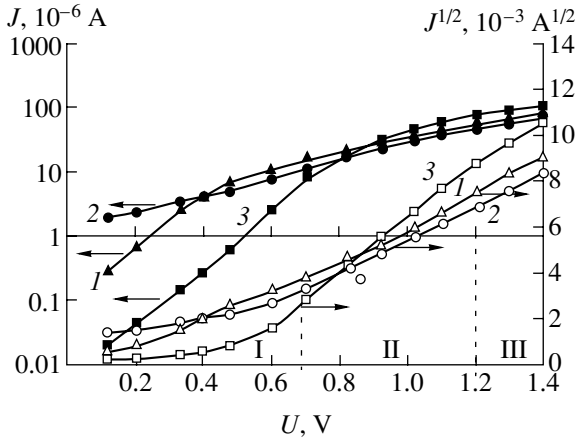

Fig. 1. The capacitance–voltage characteristics of various structures approximated by exponential and quadratic curves: (*1*) Al–DyF_3–*n*-Si; (*2*) Al–NdF_3–*n*-Si; (*3*) Al–CeF_3–*n*-Si. Dashed vertical lines approximately indicate the boundaries of characteristic regions I–III for the structure with CeF_3 layer.

where

$$b = 1 + \frac{q^2 N_t^2}{C_D}, \tag{7}$$

N_t is the density of singly charged surface states, and $C_D = \varepsilon_0 \varepsilon_D / d$ is the insulator capacitance per unit area. In our case, the linear relationship is valid under the condition that $N_t = N_t^0 = \text{const}$, which implies that the surface states are distributed at a constant density in the given energy interval.

Relation (6) shows that, by extrapolating the straight lines to $U = 0$, we can determine the surface potential φ_{s0}. A comparison of these φ_{s0} values to those determined using formula (2) showed that both methods give values coinciding to within the experimental error. These φ_{s0} values are given in the table.

The current–voltage characteristics of some MIS diodes exhibited regions where $\ln J$ and, hence, φ_{s0} were nonlinear functions of U. In such cases, Eq. (6) is valid only in a narrow interval of bias voltages, where the

Some characteristics of MIS diodes with various RE fluorides as insulators

MIS structure	N_t, 10^{11} eV^{-1} cm^{-2}	φ_{s0}, V
Al–NdF_3–*n*Si	1.14 ± 0.35	0.31 ± 0.03
Al–NdF_3–*p*Si	1.84 ± 0.50	0.35 ± 0.01
Al–CeF_3–*n*Si	2.25 ± 0.64	0.43 ± 0.05
Al–CeF_3–*p*Si	10.7 ± 0.26	0.29 ± 0.05
Al–DyF_3–*n*Si	21.4 ± 1.56	0.11 ± 0.05
Al–DyF_3–*p*Si	2.78 ± 0.67	0.37 ± 0.01

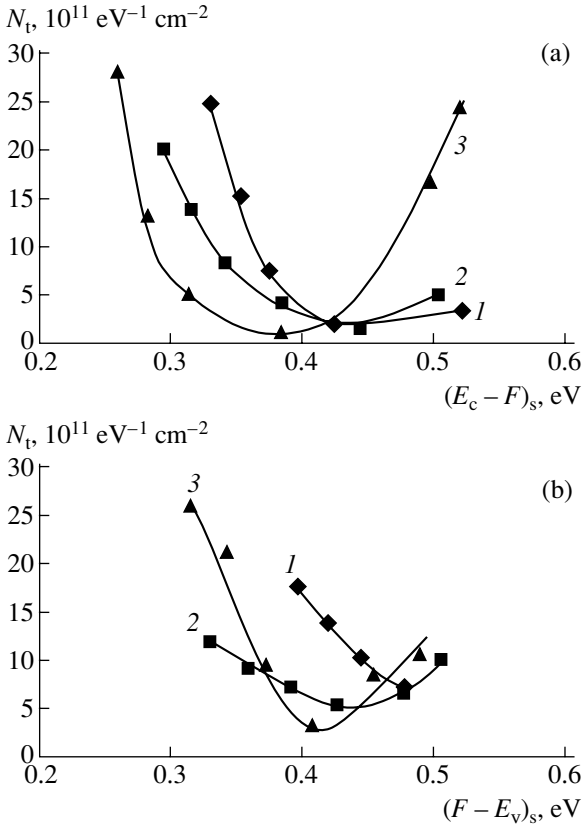

Fig. 2. Energy distributions of the density of surface states in the bandgap of (a) *n*-type and (b) *p*-type silicon substrates covered with layers of various RE fluorides: (*1*) DyF_3; (*2*) NdF_3; (*3*) CeF_3.

Fermi level at the semiconductor surface crosses the levels of surface states distributed with a constant density.

According to Eq. (6),

$$\frac{d\varphi_s}{dU} = -b^{-1}. \qquad (8)$$

Using this relation and taking into account formula (7), we obtain

$$N_t = \frac{\varepsilon_0\varepsilon_D}{q^2 d}\left\{\frac{q}{kT}\left[\frac{d(\ln J)}{dU}\right]^{-1} - 1\right\}. \qquad (9)$$

The values of the constant density N_t of surface states calculated using formula (9) are presented in the table.

Figure 2 shows the energy distributions of the density of surface states in the semiconductor bandgap calculated using formula (9). The energy distribution of N_t on the surface of silicon in contact with a layer of RE fluoride exhibits a minimum at the middle of the bandgap. The minimum density of surface states was observed for the silicon surface covered with neodymium fluoride. This result agrees with our data previously reported in [5], where it was found that neodymium fluoride films produce a passivating effect on the silicon surface.

The results of our investigation show the possibility of obtaining and studying thick and tunnel-thin insulating layers of RE fluorides deposited in a single technological cycle on the same substrate. The insulator–semiconductor interface can be characterized by the energy distribution of the density of surface states and by the surface potential. A small density of surface states (~10^{11} eV^{-1} cm^{-2}) makes it possible to use such RE fluoride layers for passivating the surface of silicon.

REFERENCES

1. V. A. Rozhkov and M. B. Shalimova, Fiz. Tekh. Poluprovodn. (St. Petersburg) **32**, 1349 (1998) [Semiconductors **32**, 1201 (1998)].
2. *Tunneling Phenomena in Solids*, Ed. by E. Burstein and S. Lundqvist (Plenum, New York, 1969).
3. J. S. Blakemore, *Semiconductor Statistics* (Pergamon Press, Oxford, 1962).
4. V. I. Gaman, *Physics of Semiconductors* (Izd. NTL, Tomsk, 2000) [in Russian].
5. V. A. Rozhkov, A. I. Petrov, and M. B. Shalimova, Pis'ma Zh. Tekh. Fiz. **19** (19), 10 (1993) [Tech. Phys. Lett. **19**, 606 (1993)].

Translated by P. Pozdeev

Technical Physics Letters, Vol. 31, No. 1, 2005, pp. 61–63. Translated from Pis'ma v Zhurnal Tekhnicheskoĭ Fiziki, Vol. 31, No. 2, 2005, pp. 34–40.

The Effect of Adsorbed Oxygen on the Conductivity of Perylenetetracarboxylic Acid *N*,*N*-Dimethyldiimide Films

A. E. Pochtenny* and A. N. Lappo

Belarussian State Technological University, Minsk, Belarus

** e-mail: pae@tut.by*

Received July 16, 2004

Abstract—The effect of adsorbed oxygen on the conductivity of vacuum-deposited perylenetetracarboxylic acid *N*,*N*-dimethyldiimide films with variable surface topography was studied using the method of cyclic thermodesorption. The results are interpreted in terms of a two-level hopping conductivity model. Microscopic parameters of the electron hopping transport (the radius of electron localization in the intrinsic and impurity states and the concentration of localization centers) are evaluated. The regions of oxygen concentrations in which the electron transport proceeds by hopping via intrinsic states, or impurity localized electron states, or a combined system involving the states of both types are determined. © *2005 Pleiades Publishing, Inc.*

Organic semiconductor electronic devices such as light-emitting diodes, solar cells, field-effect transistors, and gas sensors operate in contact with the ambient gas medium. It is well known [1] that oxygen adsorbed from the atmosphere significantly influences the electron properties of organic materials. Detailed knowledge about the mechanism of this influence is therefore necessary for the prediction and optimization of the properties of electronic devices employing such materials.

Previously [2], it was suggested to use the methods of cyclic thermodesorption in combination with a model of two-level electron hopping transport for the investigation of electrical properties of organic films in the presence of atmospheric oxygen. In particular, it was demonstrated that a decrease in the concentration of oxygen adsorbed on laser-deposited films of lead phthalocyanine (PbPc) leads to a transition from intrinsic to impurity-mediated hopping conductivity in these films. It was found impossible to reduce the concentration of oxygen adsorbed on PbPc films down to a level where the conductivity type would change from impurity to back intrinsic, and it was suggested that such a transition can be probably observed in the films of perylene pigments.

In this context, the aim of this study was to elucidate the mechanism through which adsorbed oxygen influences the conductivity of perylenetetracarboxylic acid *N*,*N*-dimethyldiimide (PTCDI) films. The films of compounds belonging to perylene series are widely used in organic optoelectronics [3, 4]. From the standpoint of our investigation, it was especially interesting to study PTCDI films because their surface morphology significantly depends on the sample preparation conditions.

The experiments were performed with 100-nm-thick PTCDI films prepared in vacuum (10^{-2} Pa) by laser sputtering of a powder target followed by deposition of the sputtered products onto polycor (ceramic composite) substrates bearing a preliminarily formed interdigital system of electrodes. In one series of samples, PTCDI films were deposited on substrates at 20°C, while in the other series, the substrates were heated to 150°C during the deposition process. Recently [5], we have studied PTCDI films by methods of atomic force microscopy and scanning electron microscopy and established that the films possess a granular structure and that deposits formed at a substrate temperature of 150°C are characterized by higher surface roughness and greater intergranular spacings as compared to those in the deposits obtained on the same substrates at 20°C. These differences in the film topography suggest that the PTCDI films deposited at 150°C probably possess a higher adsorption capacity.

The dc conductivity of PTCDI films was measured in a vacuum of 10^{-2} Pa with the aid of a V7E-42 electrometer (Belvar company, Belarus). The investigation was performed by the method of cyclic thermodesorption [6]. According to this technique, a sample is heated to a certain preset temperature and then allowed to cool. In the course of cooling, the specific conductivity of the sample σ is measured as a function of the absolute temperature T and described in terms of the equation

$$\sigma = \sigma_0 \exp\left(-\frac{E_a}{kT}\right), \quad (1)$$

were σ_0 is the preexponential (tunneling) factor, E_a is the conductivity activation energy, and k is the Boltzmann constant. Variation of the oxygen concentration

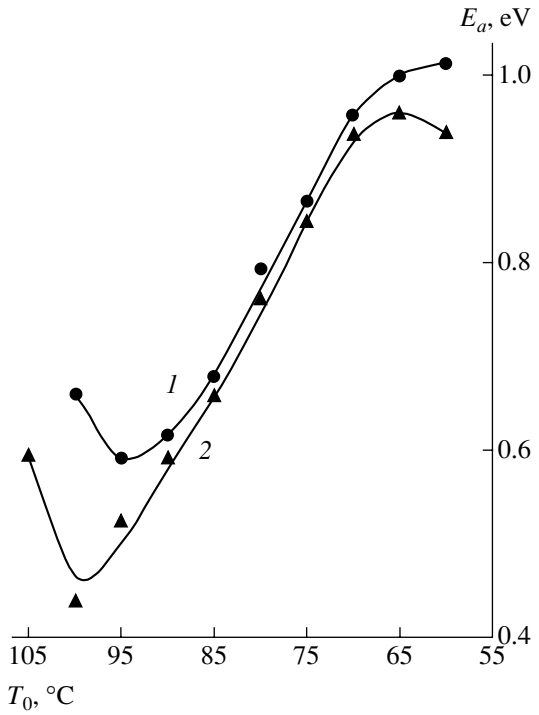

Fig. 1. Plots of the conductivity activation energy E_a versus temperature T_0 of the onset of cooling for PTCDI films deposited at a substrate temperature of (*1*) 20°C and (*2*) 150°C.

in the course of cooling was ignored because these measurements were performed in vacuum.

The experiment consisted in a sequence of cycles, whereby the sample was heated to a stepwise increased temperature T_0, which corresponded to a gradually decreased concentration of adsorbed oxygen. By measuring the temperature variation of conductivity in the course of cooling the sample from this temperature in vacuum, we obtained a family of curves corresponding to various concentrations of adsorbed oxygen on the same sample. Using this set of temperature dependences, we determined the corresponding room-temperature conductivities σ and the parameters σ_0 and E_a corresponding to various concentrations of adsorbed oxygen.

Figure 1 shows the experimental curves obtained as described above using thermal cycles with the temperature T_0 gradually increased from 60 to 110°C. Qualitatively, these curves reflect the dependence of the conductivity activation energy on the concentration of adsorbed oxygen (which decreases with increasing T_0). As can be seen from Fig. 1, there are regions in which the activation energy exhibits both increase and decrease. This behavior can be explained in terms of a two-level hopping conductivity model [2], according to which the charge transport proceeds via two parallel channels involving intrinsic and impurity electron states.

In terms of the adopted model, the specific conductivity is expressed as

$$\sigma = (\sigma_{03})_1 \exp\left(-\frac{\alpha}{a_1 n_1^{1/3}} - \frac{E_{a1}}{kT}\right) + (\sigma_{03})_2 \exp\left(-\frac{\alpha}{a_2 n_2^{1/3}} - \frac{E_{a2}}{kT}\right), \quad (2)$$

where $(\sigma_{03})_1$ and $(\sigma_{03})_2$ are constants depending on the electron localization radius; $\alpha = 1.73$ is the percolation constant [7]; n_1 and n_2 are the concentrations of localization centers corresponding to the intrinsic and impurity states, respectively; and E_{a1} and E_{a2} are the activation energies of conductivity via the intrinsic and impurity states, respectively. The latter quantities are determined by the formulas [8]

$$E_{a1} = \frac{0.99e^2 n_1^{1/3}}{4\pi\varepsilon_0\varepsilon}, \quad E_{a2} = \frac{0.99e^2 n_2^{1/3}}{4\pi\varepsilon_0\varepsilon}, \quad (3)$$

where ε_0 is the permittivity of vacuum and ε is the relative permittivity.

Since the impurity levels appear as a result of separation from the set of intrinsic levels, the concentration of the electron localization centers related to the intrinsic and impurity states must obey the condition

$$n_1 + n_2 = n = \text{const}. \quad (4)$$

The temperature dependence of the conductivity is described by Eq. (1), from which the conductivity activation energy can be experimentally determined as

$$E_a = -\frac{\partial(\ln\sigma)}{\partial(1/kT)}. \quad (5)$$

The results of calculation of the conductivity activation energy using Eqs. (1)–(5) are represented by the solid curve in Fig. 2, where the relative concentration of adsorbed oxygen is defined as $x = n_2/n$. The best agreement between the calculated curve and experiment was observed for the parameters $a_1 = 87.5$ pm, $a_2 = 90$ pm, and $n = 3.3 \times 10^{27}$ m^{-3}, which were the same for the PTCDI films with the surface topography of both types.

As can be seen from Fig. 2, the conductivity and its activation energy at high initial concentrations of adsorbed oxygen ($x > 0.5$) are determined by the electron transport via intrinsic states. As oxygen is desorbed, the amount of impurity states decreases, while that of the intrinsic states accordingly increases. This leads to an increase in the conductivity activation energy in accordance with formulas (3). Note that this region corresponds to the experimental data obtained only for the samples of PTCDI films deposited at 150°C. This result confirms the assumption that such samples are characterized by a higher adsorption

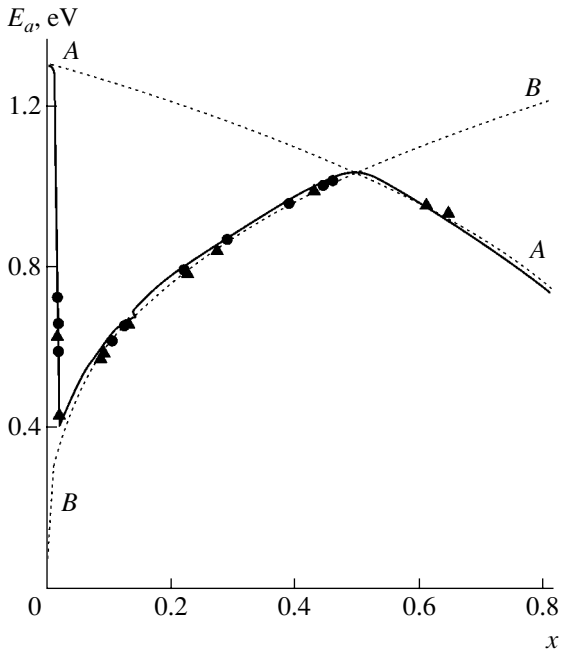

Fig. 2. Relation between the conductivity activation energy E_a and relative concentration x of oxygen adsorbed on a PTCDI film. Symbols represent the experimental data for the films deposited at a substrate temperature of 20°C (circles) and 150°C (triangles); dotted curves show the results of calculations taking into account only intrinsic (*A–A)* or impurity (*B–B*) states, and solid curve shows the results of calculations using a two-level hopping conductivity model.

capacity. For $x < 0.5$, the Fermi level is trapped at the impurity states and the electron transport via these states dominates in the conductivity of PTCDI films with further decrease in the concentration of adsorbed oxygen down to $x = 0.02$. Then, the system again exhibits the transition from impurity to intrinsic conductivity and the experimental points correspond to a situation where the conductivity is provided by the electron transport via a combined system of intrinsic and impurity electron states.

Thus, by comparing the experimental data obtained using the method of cyclic thermodesorption with the results of calculations performed within the framework of a two-level hopping conductivity model, we have evaluated the radii of electron localization in the intrinsic and impurity states and the concentration of the localization centers in PTCDI films. It was established that, depending on the concentration of adsorbed oxygen, the conductivity of these films can be provided either separately by the intrinsic or the impurity localized electron states, or by a combined system of intrinsic and impurity electron states. It was found that the surface topography does not influence the microscopic parameters of charge transport and the difference between electrical properties of PTCDI films with different topography is related to a difference in the adsorption capacity and, hence, in the concentration of adsorbed oxygen.

Acknowledgments. this study was supported by the programs “Nanostructural Materials and Nanotechnology” (project GB21-066) and “Electronics” (project GB23-119).

REFERENCES

1. J. Simon and J.-J. Andre, *Molecular Semiconductors* (Springer-Verlag, Berlin, 1985).
2. A. E. Pochtennyĭ and A. V. Misevich, Pis’ma Zh. Tekh. Fiz. **29** (1), 56 (2003) [Tech. Phys. Lett. **29**, 26 (2003)].
3. S. R. Forrest, Chem. Rev. **97**, 1793 (1997).
4. P. Peumans, S. Uchida, and S. R. Forrest, Nature **425**, 158 (2003).
5. A. N. Lappo, A. V. Misevich, A. E. Pochtenny, *et al.*, *Physics, Chemistry, and Application of Nanostructures* (World Scientific, Singapore, 2003), pp. 96–100.
6. A. E. Pochtennyĭ, D. I. Sagaĭdak, G. G. Fedoruk, *et al.*, Fiz. Tverd. Tela (St. Petersburg) **38**, 2592 (1996) [Phys. Solid State **38**, 1422 (1996)].
7. B. I. Shklovskii and A. L. Efros, *Electronic Properties of Doped Semiconductors* (Nauka, Moscow, 1979; Springer-Verlag, New York, 1984).
8. B. I. Shklovskiĭ, A. L. Efros, and I. Ya. Yanchev, Pis’ma Zh. Éksp. Teor. Fiz. **14**, 348 (1971) [JETP Lett. **14**, 269 (1971)].

Translated by P. Pozdeev

Technical Physics Letters, Vol. 31, No. 1, 2005, pp. 64–67. Translated from Pis'ma v Zhurnal Tekhnicheskoĭ Fiziki, Vol. 31, No. 2, 2005, pp. 41–48.

Recovery of Equations of Coupled Time-Delay Systems from Time Series

V. I. Ponomarenko and M. D. Prokhorov

Saratov Branch, Institute of Radio Engineering and Electronics, Russian Academy of Sciences, Saratov, Russia

e-mail: sbire@sgu.ru

Received July 29, 2004

Abstract—A method is described for reconstructing the model differential equations with a delayed argument from time series of coupled systems with time-delay feedback. Using this method, it is also possible to establish the presence of coupling between time-delay systems and to determine the type, direction, and magnitude of coupling. The performance of the proposed method is illustrated by application to the experimental time series of coupled oscillators with time-delay feedback. © *2005 Pleiades Publishing, Inc.*

Introduction. In recent years, the problem of reconstruction of the equations of nonlinear dynamical systems with time-delay feedback (time-delay systems) from their time series has received much attention [1–7]. The importance of this problem is related to the fact that time-delay systems are frequently encountered in nature [8]. The behavior of such systems is not entirely determined by the present state, but depends on the preceding states as well. Accordingly, the time-delay systems are usually described in terms of differential equations with a delayed argument. Such models are successfully used in various fields of physics, biology, physiology, and chemistry.

In some practically important cases, we are dealing with time-delay systems interacting with one another. In particular, such coupled systems are used in description of the dynamics of interacting populations [9–11] and in simulations of processes occurring in the human cardiovascular system [12, 13]. There are good prospects for using such models in the analysis of communication systems for secure data transmission [14], including those based on optical-feedback lasers [15–17]. However, the problem of reconstruction of the model equations of coupled time-delay system from their time series remains practically unstudied, although this situation is encountered in solving many important practical problems.

In this Letter, we describe a method capable of reconstructing the equations of coupled systems from their chaotic time series, determining the character of coupling (not known a priori), and finding the coupling coefficients.

Description of coupled systems. Consider two time-delay systems, X_1 and X_2, described in the absence of coupling by first-order differential equations with delayed argument of the following general type:

$$\varepsilon_{1,2}\dot{x}_{1,2}(t) = -x_{1,2}(t) + f_{1,2}(x_{1,2}(t-\tau_{1,2})), \quad (1)$$

where $x_{1,2}$ are the dynamical variables at the time t, $\tau_{1,2}$ are the delay times, $f_{1,2}$ are nonlinear functions, $\varepsilon_{1,2}$ are the parameters characterizing the inertial properties of the systems (subscripts 1 and 2 assign the variables and parameters to the systems X_1 and X_2, respectively). In the general case, Eq. (1) represents the mathematical model of an oscillatory system known in radio engineering as a delay-feedback oscillator [18], comprising a circuit with three ideal elements: nonlinear device, inertial element, and delay line. Below, these elements will be denoted by f, ε, and τ, respectively.

The time-delay systems X_1 and X_2 can be coupled in different ways. We will distinguish three types of coupling, by which the variable $x_1(t)$ of system X_1 is introduced with a certain coefficient k_1 into various points of circuit X_2 denoted by Arabic numerals *1–3* in Fig. 1. By the same token, the variable $x_2(t)$ of system X_2 can be introduced with the coefficient k_2 into various points of circuit X_1 denoted by Roman numerals I–III in Fig. 1. In the case when the types of coupling X_1 to X_2 and X_2 to X_1 are the same, the dynamics of these coupled systems is described by one of the following equations:

$$\varepsilon_{1,2}\dot{x}_{1,2}(t) = -x_{1,2}(t) + f_{1,2}(x_{1,2}(t-\tau_{1,2}) + k_{2,1}x_{2,1}(t-\tau_{1,2})), \quad (2)$$

$$\varepsilon_{1,2}\dot{x}_{1,2}(t) = -x_{1,2}(t) + f_{1,2}(x_{1,2}(t-\tau_{1,2}) + k_{2,1}x_{2,1}(t)), \quad (3)$$

$$\varepsilon_{1,2}\dot{x}_{1,2}(t) = -x_{1,2}(t) + f_{1,2}(x_{1,2}(t-\tau_{1,2})) + k_{2,1}x_{2,1}(t), \quad (4)$$

where $k_{1,2}$ are the coupling coefficients. Here, Eq. (2) describes the type of coupling referred to below as *1*/I, whereby the first time-delay system acts upon the sec-

1063-7850/05/3101-0064$26.00 © 2005 Pleiades Publishing, Inc.

ond system at point *1* and the second time-delay system acts upon the first system at point I. By the same token, Eqs. (3) and (4) describe the mutually interacting systems coupled to each other at points *2*/II and *3*/III, respectively. If the types of mutual coupling of systems X_1 and X_2 are different, the common system will be described by the equations of different types. For example, the type of coupling denoted *1*/II implies that system X_1 is described by Eq. (3), while system X_2 is described by Eq. (2).

Description of the method. First, let us reconstruct the equation of system X_1, that is, determine the parameters τ_1, ε_1, and k_2 and find the function f_1 from the available time series. In order to determine the delay time τ_1 from the observed time series $x_1(t)$, we use the method developed in [5], where it was demonstrated that time series of the systems of type (1) contain virtually no extrema spaced from each other by τ_1. In order to find τ_1, we have to indicate extrema in the initial time series, determine the numbers N of the pairs of extrema in this series spaced by various times τ, and construct the $N(\tau)$ function. Then, the delay time τ_1 is determined by the position of the absolute minimum of the $N(\tau)$ function. The results of our investigations showed that this approach can be also successfully used in cases when system X_1 occurs under the action of another system X_2, provided that this external action does not lead to the appearance of a large number of additional extrema in the time realizations of oscillations in system X_1.

For determining the parameter ε_1 and the function f_1 of system X_1, as well as the coupling coefficient k_2, we propose a method based on an analysis of the time series of both observables $x_1(t)$ and $x_2(t)$. First, let us assume that the type of action of system X_2 upon system X_1 (i.e., the structure of equation describing dynamics of the time-delay system X_1 under the external action) is known. For example, consider the coupling type described by Eq. (2), whereby the variable of system X_2 is introduced into the feedback circuit of X_1 before the delay element (i.e., at point I in Fig. 1). In this case, Eq. (2) for system X_1 can be written as

$$\varepsilon_1\dot{x}_1(t) + x_1(t) = f_1(x_1(t-\tau_1) + k_2x_2(t-\tau_1)). \quad (5)$$

As can be seen from Eq. (5), a set of points with the coordinates $(x_1(t-\tau_1) + k_2x_2(t-\tau_1), \varepsilon_1\dot{x}_1(t) + x_1(t))$ plotted on the plane will reproduce the function f_1. Since the quantities ε_1 and k_2 are not known a priori, we have to plot $\varepsilon\dot{x}_1(t) + x_1(t)$ versus $x_1(t-\tau_1) + kx_2(t-\tau_1)$ for various ε and k in search for the single-valued relationship that is possible only for $\varepsilon = \varepsilon_1$ and $k = k_2$. As a quantitative criterion of such a unique relationship in the search for ε_1 and k_2, we can use the minimum length of a segment $L(\varepsilon, k)$ connecting points (ordered with respect to the abscissa) on the above plane. A minimum

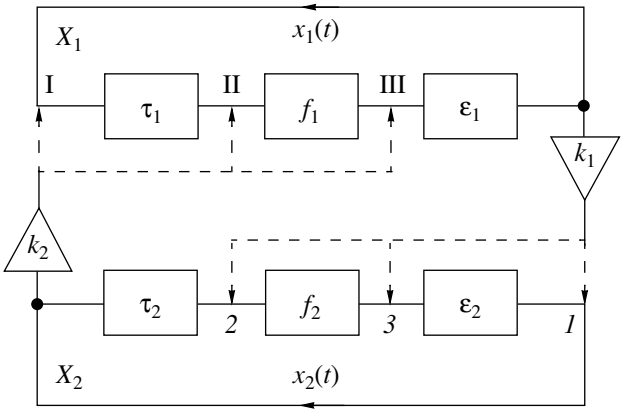

Fig. 1. Schematic diagram of coupled time-delay systems X_1 and X_2. Elements denoted by $\tau_{1,2}$, $f_{1,2}$, and $\varepsilon_{1,2}$ represent the delay line, nonlinear device, and inertial transformation of oscillations, respectively; elements $k_{1,2}$ determine the mutual coupling of systems X_1 and X_2. Points *1–3* (I–III) represent various types of introduction of the action of system X_1 into system X_2 (X_2 into system X_1).

of $L(\varepsilon, k)$ ($L_{\min}(\varepsilon, k)$) will correspond to $\varepsilon = \varepsilon_1$ and $k = k_2$, while the dependence of $\varepsilon_1\dot{x}_1(t) + x_1(t)$ on $x_1(t-\tau_1) + k_2x_2(t-\tau_1)$ constructed for these parameters will reproduce a certain nonlinear function that can be (if necessary) approximated. The proposed approach employs all points of the time series, which allows short time series to be used for reconstruction of the system parameters ε_1 and k_2 and the nonlinear function f_1.

The same method can be used for reconstructing the nonlinear function f_1 and the parameters ε_1 and k_2 in the situations described by Eqs. (3) and (4), by plotting $\varepsilon\dot{x}_1(t) + x_1(t)$ versus $x_1(t-\tau_1) + kx_2(t)$ and $\varepsilon\dot{x}_1(t) + x_1(t) - kx_2(t)$ versus $x_1(t-\tau_1)$, respectively, for various ε and k. If the point (I, II, or III) at which system X_2 acts upon system X_1 is not known a priori, it is necessary to perform reconstruction for each of the three model equations (2)–(4) for system X_1 and determine the corresponding values of $L_{\min}(\varepsilon, k)$. The only correct structure of the model equation will be indicated by single-valued form of the reconstructed function and, accordingly, by the lowest of the three values of $L_{\min}(\varepsilon, k)$. Thus, the proposed method allows both the parameters of mutually coupled time-delay systems and the type of this action (i.e., the form of the model equation) to be reconstructed from the observed time series.

The same procedures are used to reconstruct the time-delay system X_2 from the available time series of variables $x_2(t)$ and $x_1(t)$. These procedures yield the parameters τ_2 and ε_2, define the form of the nonlinear function f_2 for system X_2, and determine the coupling coefficient k_1 and the type of action of system X_1 upon system X_2.

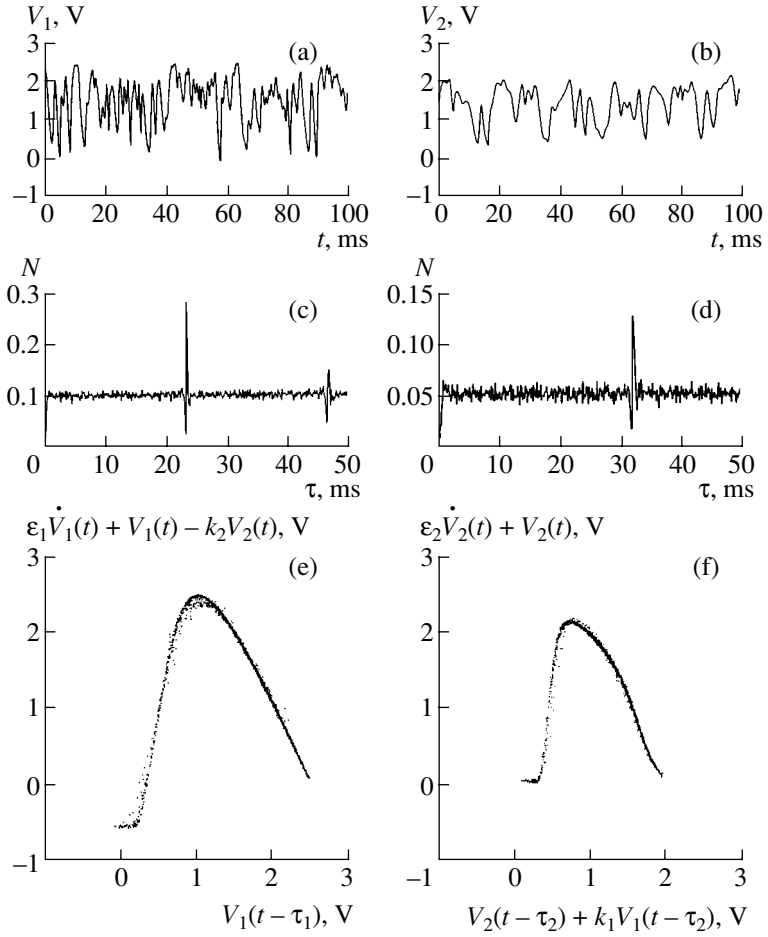

Fig. 2. Reconstruction of the system of two delay-feedback oscillators coupled in the *1*/III type: (a, b) typical experimental time series of systems X_1 and X_2, respectively; (c, d) plots of the number N of the pairs of extrema in a time series of X_1 and X_2, respectively, spaced by various times τ, normalized to the total number of such extrema; (e) reconstruction of the nonlinear function f_1 (for τ_1 = 23.0 ms, ε_1 = 0.46 ms, and k_2 = 0.10); (f) reconstruction of the nonlinear function f_2 (for τ_2 = 31.7 ms, ε_2 = 1.06 ms, and k_1 = –0.10).

Verification of the method. We have verified the proposed reconstruction method by applying the procedure outlined above to the experimental time series of two coupled delay-feedback oscillators. When such coupled oscillators are schematically depicted as in Fig. 1, the delay of signal $x_1(t)$ by the time τ_1 and the delay of signal $x_2(t)$ by the time τ_2 are provided by the corresponding delay line; the role of a nonlinear element in each oscillator is played by an amplifier with a transmission function f_1 or f_2; the inertial properties are determined by a filter, the parameters of which define ε_1 or ε_2; and the coupling is effected by adding amplifiers ensuring the transmission coefficients k_1 or k_2. In the example under consideration, the coupling type according to our classification corresponded to *1*/III. In the case when the inertial element is a first-order low-frequency *RC* filter, such oscillators in the absence of coupling are described by the equation

$$R_{1,2}C_{1,2}\dot{V}_{1,2}(t) = -V_{1,2}(t) + f_{1,2}(V_{1,2}(t-\tau_{1,2})), \quad (6)$$

where $V_{1,2}(t)$ and $V_{1,2}(t-\tau_{1,2})$ are the voltages at the input and output of the corresponding delay line; and $R_{1,2}$ and $C_{1,2}$ are the resistances and capacitances in the filters of the corresponding oscillator, respectively. Equation (6) has the form of Eq. (1) with $\varepsilon_{1,2} = R_{1,2}C_{1,2}$.

The signals $V_1(t)$ and $V_2(t)$ at the input of the corresponding delay line were recorded and digitized using an analog-to-digital converter at sampling rate of 10 kHz for the following parameters of coupled oscillators: τ_1 = 23 ms; τ_2 = 31.7 ms; R_1C_1 = 0.48 ms; R_2C_2 = 1.01 ms; k_1 = –0.1; k_2 = 0.1. Fragments of the corresponding time series are presented in Figs. 2a and 2b. Upon counting the number of situations where the signals $\dot{V}_1(t)$ and $\dot{V}_1(t-\tau)$ simultaneously vanish for various τ (tried at a step equal to the period of sampling T_s = 0.1 ms), we construct the function $N(\tau)$ (Fig. 2c). In order to evaluate the derivative $\dot{V}_1(t)$ from the time

series, we used a local parabolic approximation. The absolute minimum of $N(\tau)$ is observed for the first oscillator at $\tau = 23.0$ ms (Fig. 2c) and for the second oscillator at $\tau = 31.7$ ms (Fig. 2d).

During the reconstruction of oscillator X_1 in the form of Eq. (4), the curve of $L(\varepsilon, k)$, constructed using a 0.01 ms step in ε and a 0.01 step in k, exhibited a minimum at $\varepsilon = 0.46$ ms and $k = 0.10$ (which provides a quite close estimation of the ε_1 and k_2 values). The reconstructed nonlinear function (Fig. 2e) shows a good coincidence with the true transmission characteristic f_1 of the nonlinear element of the first oscillator.

A minimum of the curve of $L(\varepsilon, k)$ constructed for system X_2 represented by Eq, (2) was observed at $\varepsilon = 1.06$ ms and $k = -0.10$ (also sufficiently close to the true values of ε_2 and k_1). The reconstructed nonlinear function f_2 is depicted in Fig. 2f.

Conclusion. We proposed a method for reconstructing coupled time delay systems using the observable time series. This method allows the delay times, inertial parameters, nonlinear functions, and coupling coefficients for the two coupled time-delay systems to be determined, even when the type of coupling is a priori unknown. In the latter case, the reconstruction procedure makes it possible to establish the type of coupling between the time-delay systems. In contrast to other methods of determining the coupling between systems using their time series [19–21], the proposed procedure is capable of determining not only the direction of coupling, but its magnitude as well.

Acknowledgments. This study was supported by the Russian Foundation for Basic Research (project no. 03-02-17593), by the US Civilian Research and Development Foundation for Independent States of the Former Soviet Union (award no. REC-006), and by the INTAS Foundation (grant no. 03-55-920).

REFERENCES

1. M. J. Bünner, M. Popp, Th. Meyer, *et al.*, Phys. Rev. E **54**, 3082 (1996).
2. H. Voss and J. Kurths, Phys. Lett. A **234**, 336 (1997).
3. R. Hegger, M. J. Bünner, H. Kantz, and A. Giaquinta, Phys. Rev. Lett. **81**, 558 (1998).
4. M. J. Bünner, M. Ciofini, A. Giaquinta, *et al.*, Eur. Phys. J. D **10**, 165 (2000).
5. B. P. Bezruchko, A. S. Karavaev, V. I. Ponomarenko, and M. D. Prokhorov, Phys. Rev. E **64**, 056216 (2001).
6. V. I. Ponomarenko and M. D. Prokhorov, Pis'ma Zh. Tekh. Fiz. **28** (16), 37 (2002) [Tech. Phys. Lett. **28**, 680 (2002)].
7. V. S. Udaltsov, J.-P. Goedgebuer, L. Larger, *et al.*, Phys. Lett. A **308**, 54 (2003).
8. J. K. Hale and S. M. V. Lunel, *Introduction to Functional Differential Equations* (Springer, New York, 1993).
9. Y. Kuang, *Delay Differential Equations With Applications in Population Dynamics* (Academic Press, Boston, 1993).
10. G. A. Bocharov and F. A. Rihan, J. Comp. Appl. Math. **125**, 183 (2000).
11. Y. Song, M. Han, and Y. Peng, Chaos, Solitons and Fractals **22**, 1139 (2004).
12. H. Seidel and H. Herzel, Physica D **115**, 145 (1998).
13. K. Kotani, K. Takamasu, Y. Ashkenazy, *et al.*, Phys. Rev. E **65**, 051923 (2002).
14. B. Mensour and A. Longtin, Phys. Lett. A **244** (1–3), 59 (1998).
15. V. S. Udaltsov, J.-P. Goedgebuer, L. Larger, and W. T. Rhodes, Phys. Rev. Lett. **86**, 1892 (2001).
16. I. V. Koryukin and P. Mandel, Phys. Rev. E **65**, 026201 (2002).
17. E. M. Shahverdiev, S. Sivaprakasam, and K. A. Shore, Phys. Rev. E **66**, 017206 (2002).
18. A. S. Dmitriev and V. Ya. Kislov, *Stochastic Oscillations in Radio Physics and Electronics* (Nauka, Moscow, 1989) [in Russian].
19. M. G. Rosenblum and A. S. Pikovsky, Phys. Rev. E **64**, 045202 (2001).
20. M. G. Rosenblum, L. Cimponeriu, A. Bezerianos, *et al.*, Phys. Rev. E **65**, 041909 (2002).
21. D. A. Smirnov and B. P. Bezruchko, Phys. Rev. E **68**, 046209 (2003).

Translated by P. Pozdeev

Technical Physics Letters, Vol. 31, No. 1, 2005, pp. 68–71. Translated from Pis'ma v Zhurnal Tekhnicheskoĭ Fiziki, Vol. 31, No. 2, 2005, pp. 49–56.

Full-Wave Analysis of Fundamental Modes of a Multicoupled Strip Line with Ferroelectric Film

I. B. Vendik[a,*], O. G. Vendik[a,], M. S. Gashinova[a], and A. N. Deleniv[b,***]**

[a] *St. Petersburg State Electrotechnical University, St. Petersburg, 197376 Russia*

[b] *Chalmers University of Technology, SE-41296 Göteborg, Sweden*

*e-mail: *MWLab@eltech.ru; **Vendik@mail.eltech.ru; ***anatoli.deleniv@mc2.chalmers.se*

Received July 28, 2004

Abstract—The properties of a multicoupled microstrip line (MSL) with a thin control ferroelectric layer have been analyzed in terms of a full-wave model based on the method of moments in spectral domain. The *Q* values for all fundamental modes and their contributions to MSL losses are determined. It is established that various fundamental modes in multicoupled MSLs are characterized by significantly different *Q* values. The proposed method has been applied to the analysis of characteristics of an MSL-based ferroelectric microwave phase shifter. The figure of merit *F* of the phase shifter has been calculated for each fundamental mode. The results of analysis lead to a conclusion that, by exciting a fixed mode characterized by the maximum *Q* value, it is possible to obtain an MSL-based phase shifter possessing the optimum *F* at a minimum necessary level of the control voltage. © *2005 Pleiades Publishing, Inc.*

Ferroelectric phase shifters are usually based on coplanar transmission lines and provided with control elements in the form of a thin ferroelectric film with a permittivity determined by the applied voltage [1]. The narrower the slit width in the coplanar line, the lower the necessary level of control voltages. On the other hand, a decrease in this width leads to an increase in the ohmic losses in electrodes (characterized by a finite conductivity). Multicoupled microstrip lines (MSLs) can also be used as phase shifters. The equivalent circuit scheme of an MSL in the microwave field comprises serially connected slits, and in a dc field, the slits connected in parallel [2, 3]. In this case, it is possible to obtain the optimum combination of a low level of losses, caused by the finite conductivity of electrodes, with low values of the dc control voltage. In addition, MSLs make possible the suppression of nonlinear effects for increased microwave signal powers [4].

Formulation of the problem and description of the model. We analyze the properties of *N* orthogonal fundamental modes existing in an *N*-fold-coupled MSL. The aim is to establish which of these modes is characterized by the maximum figure of merit *F* defined as the ratio of the phase shift to the level of losses. The analysis is performed using the method of moments in the Fourier spectral domain [5, 6]. Using this approach, it is possible to determine the dispersion characteristics of the MSL in a multilayer medium, that is, the frequency-dependent complex propagation constants of the fundamental modes.

Method of calculation. Let us consider the model structure comprising an MSL in a three-layer medium (Fig. 1). The complex propagation constant is $k_z^{(n)}(\omega) = \beta^{(n)}(\omega) - i\alpha^{(n)}(\omega)$, where ω is the circular frequency, $\beta(n)$ is the phase constant, and $\alpha(n)$ is the decay constant of the *n*th mode propagating in the *z* direction. Each layer of the model structure is characterized by the complex permittivity

$$\varepsilon = \varepsilon_0\varepsilon_r(1 - j\tan\delta), \qquad (1)$$

where ε_r and ε_0 are the relative permittivity of the layer

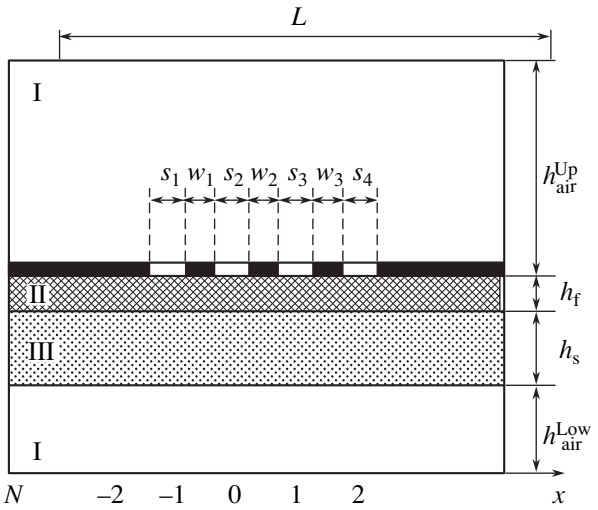

Fig. 1. Transverse section of the model symmetric four-slit line: (I) air; (II) ferroelectric layer; (III) alumina ceramic; *N* is electrode number. Substrate parameters: ε_f = 750 or 1500; ε_s = 9.8. Characteristic dimensions: h_{air}^{Up} = 7 mm; h_f = 1 μm; h_s = 0.5 mm; h_{air}^{Low} = 5 mm; *L* = 5 mm; w_k = 30 μm; s_p = 20 μm.

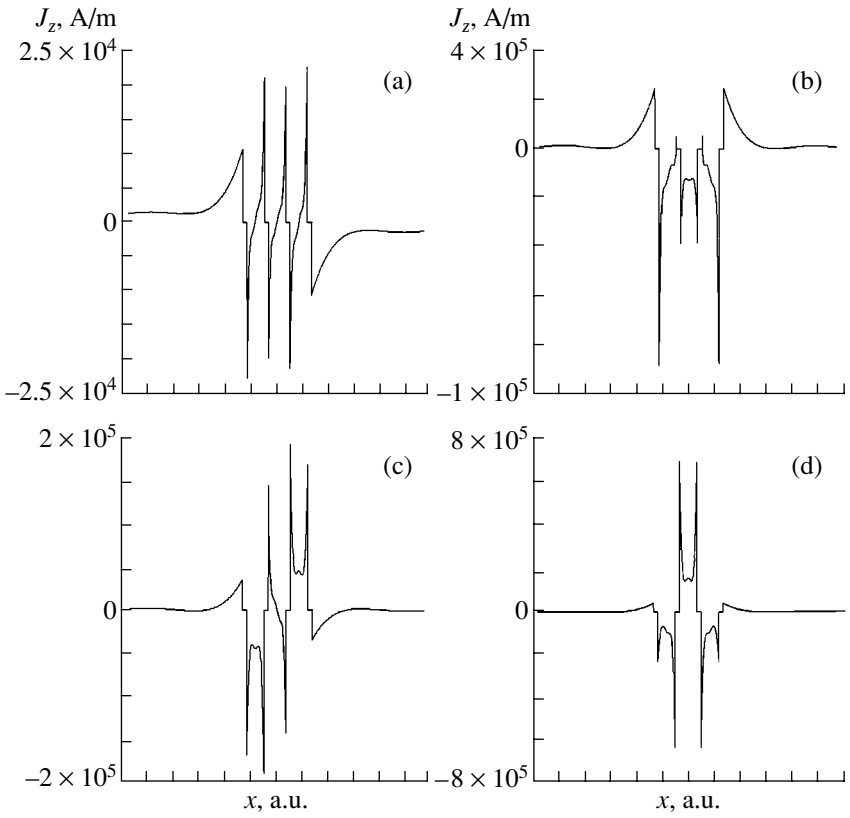

Fig. 2. Surface current density J_z distribution in the transverse section of a four-slit line with the parameters indicated in the legend to Fig. 1 (J_z is normalized to 1-A total current in the line). The scale of electrode and slit widths is changed for the sake of better illustration of the of the surface current density profile in the internal electrodes: (a) first mode; (b) second mode; (c) third mode; (d) fourth mode.

and the permittivity of vacuum, respectively, and $\tan\delta$ is the loss tangent.

The upper and lower walls of a metal box represent layers with the permittivity

$$\varepsilon = -\frac{j\sigma_c}{\omega}, \qquad (2)$$

where σ_c is the metal conductivity.

Once the parameters of layers in the model structure are determined, the energy dissipation losses in these layers are taken into account in the course of construction of the Green function. The procedure of determining the spectral image of the Green functions is based on the so-called immittance approach [7]. Losses in the conductors are described by introducing the surface impedance as

$$Z_{\text{sur}} = (1 + j)\sqrt{\frac{\omega\mu_0}{2\sigma}}.$$

Simulation is performed using the method of moments for two-dimensional integral relation between the electric field and current, assuming that the signal electrodes are negligibly thin. Finite thickness of the electrodes can be taken into account in terms of the equivalent surface impedance used in our calculations and described in detail elsewhere [6].

Following the calculation model developed in [5], we determine the propagation constants $k_z^{(n)}$ ($n = 1, \ldots, N$) for all N fundamental modes propagating in the MSL under consideration. The particular calculation was performed for $N = 4$ and a frequency of $f = 10$ GHz.

Figure 2 shows the distributions of the surface longitudinal current density in the MSL transverse section for each mode. By analyzing these profiles, it is possible to qualitatively estimate losses related to the energy transfer via each mode. Data on the corresponding distributions of the full current are presented in Table 1. These data demonstrate orthogonality of the fundamental modes.

The most interesting behavior is observed for the first mode, in which the total current in the inner MSL electrodes is zero. This provides for the minimum contribution of the finite conductivity of electrodes to the damping constant for this mode and accounts for the maximum Q value of this mode (in comparison to the other modes).

Table 1. Current distribution in the transverse section of an MSL with $N = 4$ (Fig. 1)

Mode number	Electrode number				
	–2	–1	0	1	2
1	+1	0	0	0	–1
2	+1/2	–1/3	–1/3	–1/3	+1/2
3	0	–1	0	+1	0
4	0	–1/2	+1	–1/2	0

Table 2. Propagation constants and the figure of merit of MSLs with various characters of losses

Case	Mode number	$\varepsilon_f = 750$		$\varepsilon_f = 1500$		F_c, deg/dB
		β_1	α_1	β_2	α_2	
A	1	571.42	2.01	715.38	2.69	403.563
	2	979.06	14.56	1291.38	19.287	121.795
	3	1171.24	26.35	1576.99	35.543	86.529
	4	1281.75	34.53	1738.7	46.862	74.105
	Mode number	$\varepsilon_f = 750$		$\varepsilon_f = 1500$		F_d, deg/dB
		β_1	α_1	β_2	α_2	
B	1	568.803	1.556	711.883	2.655	448.523
	2	960.62	3.544	1266.96	5.398	452.220
	3	1138.13	4.621	1532.56	6.878	452.944
	4	1238.72	5.204	1680.52	7.673	452.584
	Mode number	$\varepsilon_f = 750$		$\varepsilon_f = 1500$		F_{tot}, deg/dB
		β_1	α_1	β_2	α_2	
C	1	571.41	3.579	715.37	5.367	212.418
	2	979.01	18.176	1291.31	24.791	95.843
	3	1171.14	31.108	1576.84	42.622	72.632
	4	1281.61	39.919	1738.51	54.803	63.672

Figure of merit of an MSL-based ferroelectric microwave phase shifter. Let us consider a discrete phase shifter comprising a line segment of length l on a bilayer substrate involving a ferroelectric control layer with the permittivity switched between $\varepsilon_f^{(1)} = 750$ and $\varepsilon_f^{(2)} = 1500$. The phase shift over the line length is

$$\Delta\varphi^\circ = (\beta_2 - \beta_1) l \frac{180}{\pi}. \quad (3)$$

Average losses in decibels can be expressed as

$$a_{dB} = 8.68 \frac{\alpha_1 + \alpha_2}{2} l. \quad (4)$$

The figure of merit of the phase shifter is defined as

$$F = \frac{\Delta\varphi^\circ}{a_{dB}} = 13.2 \frac{\beta_2 - \beta_1}{\alpha_1 + \alpha_2}, \quad (5)$$

where the subscripts 1 and 2 refer to the corresponding states of the ferroelectric layer, determined by the permittivities $\varepsilon_f^{(1)}$ and $\varepsilon_f^{(2)}$.

We have calculated the propagation constants for each mode in three cases, taking into account (A) only the ohmic losses in metal electrodes ($\sigma_c = 6.0 \times 10^7\ \Omega^{-1}\ m^{-1}$), (B) only the dielectric losses in the ferroelectric layer ($\tan\delta_f = 0.01$), and (C) total losses ($\sigma_c = 6.0 \times 10^7\ \Omega^{-1}\ m^{-1}$ and $\tan\delta_f = 0.01$). This allows us to estimate the influence of losses of each type on the figure of merit for each mode. The results of calculations of the F values of different fundamental modes in the three cases are presented in Table 2. Here, F_c is the figure of merit calculated taking into account only the energy dissipation in conducting electrodes; F_d is calculated for the phase shifter with the ideal conductor and a dissipative medium; and F_{tot} is the figure of merit calculated taking into account the losses in both electrodes and the dielectric film.

Results and discussion. A comparative analysis of the data presented in Table 2 leads to the following conclusions.

(i) For the first mode, the contributions of ohmic and dielectric losses are comparable. This mode is characterized by the maximum Q value. For the modes from second to fourth, the ohmic contribution dominates over the dielectric contribution in the total losses.

(ii) The first mode provides for a maximum figure of merit of the MSL-based phase shifter, which may reach a level on the order of 200 deg/dB. It should be noted that experimental values of the figure of merit reported for some ferroelectric phase shifters fall within $F \sim 30$–90 deg/dB [8–10]. We suggest that, by exciting a fixed mode characterized by the maximum Q value and suppressing the other modes, it is possible to obtain a higher F of the MSL-based phase shifter. Use of an MSL as the base element of the phase shifter provides for a significant decrease in the level of introduced losses as compared to those in traditional devices employing coplanar lines [10], at a small level of the control voltage.

(iii) In the context of the problem under consideration, interesting experimental results have been recently reported for an MSL with a ferroelectric layer and internal electrodes possessing a rather large surface resistance [4]. The external electrodes were rather thick layers of copper and gold, while the internal electrodes were fabricated as indium tin oxide (ITO) films with a thickness of about 10 nm. The surface resistance of such films is $(2–3) \times 10^4\ \Omega$, which is six orders of magnitude greater than the resistance of copper. At the same

time, ITO electrodes allow a low-frequency control voltage to be applied to the ferroelectric field and introduce virtually no damping in the first microwave mode. These results agree with the estimates based on the results of our calculations. For the other modes considered above, the high surface resistance of ITO electrodes makes the propagation constants comparable with the phase constant. Therefore, modes from second to fourth practically cannot exist in an MSL with electrodes having such a high surface resistance.

Acknowledgments. This study was performed within the framework of the Federal Program "Research and Development in Preferred Directions of Science and Technology" (project no. 40.012.1.1.1355).

REFERENCES

1. S. S. Gevorgian, D. I. Kaparkov, and O. G. Vendik, IEE Proc. Microwave Ant. Propag. **141**, 501 (1994).
2. I. G. Mironenko and G. S. Khizha, in *Ferroelectrics in Microwave Technology*, Ed. by G. O. Vendik (Sov. Radio, Moscow, 1979), pp. 134–159.
3. I. G. Mironenko and A. A. Ivanov, Zh. Tekh. Fiz. **72** (2), 68 (2002) [Tech. Phys. **47**, 209 (2002)].
4. Y.-K. Yoon, D. Kim, H. G. Allen, *et al.*, IEEE Trans. Microwave Theor. Tech. **51**, 2568 (2003).
5. A. N. Deleniv, M. S. Gashinova, I. B. Vendik, and A. Eriksson, IEEE Trans. Microwave Theor. Tech. **50**, 2153 (2002).
6. A. N. Deleniv, M. S. Gashinova, and I. B. Vendik, IEEE Trans. Microwave Theor. Tech. **51**, 74 (2003).
7. *Numerical Techniques for Microwave and Millimeter-Wave Passive Structures*, Ed. by T. Itoh (Wiley, New York, 1989).
8. O. G. Vendik, S. P. Zubko, and M. A. Nikol'ski, Integr. Ferroelectr. **55**, 991 (2003).
9. C. L. Chen, J. Shen, S. Y. Chen, *et al.*, Appl. Phys. Lett. **78**, 652 (2001).
10. C. M. Krowne, M. Daniel, S. W. Kirchoefer, and J. M. Pond, IEEE Trans. Microwave Theor. Tech. **50**, 537 (2002).

Translated by P. Pozdeev

Technical Physics Letters, Vol. 31, No. 1, 2005, pp. 72–74. Translated from Pis'ma v Zhurnal Tekhnicheskoĭ Fiziki, Vol. 31, No. 2, 2005, pp. 57–62.

Noncoherent Radiation of Relativistic Electrons in Oriented Crystals

A. Kh. Khokonov and M. Kh. Khokonov

Kabardino-Balkarian State University, Nalchik, Kabardino-Balkaria, Russia

e-mail: khokon6@mail.ru

Received July 29, 2004

Abstract—The yield of noncoherent bremsstrahlung radiation (BR) generated by ultrarelativistic electrons moving near atomic chains in a crystal has been studied. A simple model quantitatively describing an increase in the BR yield as a result of the spatial redistribution of channeled electrons is constructed. The BR enhancement factor in thick crystals is proportional to $\ln z/z$, where z is the crystal thickness. *© 2005 Pleiades Publishing, Inc.*

Investigations of the bremsstrahlung radiation (BR) of relativistic electrons for certain target atoms in oriented crystals were performed almost simultaneously with the first experiments devoted to the phenomenon of radiation channeling [1]. Bochek *et al.* [2] experimentally observed an increase in the yield of noncoherent BR for the 1.2-GeV electrons moving at small angles ($\theta \sim \theta_L$, θ_L being the Lindhard angle [3]) relative to the $\langle 110 \rangle$ crystallographic axis in a silicon crystal. It was also established that an increase in the BR yield from oriented crystals is related to the phenomenon of spatial redistribution of the flux of channeled electrons in the field of a continuous potential of an atomic chain [4, 5]. Somewhat later, Endo *et al.* [6] experimentally demonstrated that the BR yield increases even for a relatively large angular divergence of the input electron beam ($\Delta \sim \pm 1.5\theta_L$) and studied the dependence of this effect on the orientation.

Theoretical investigations [7, 8] led to an important conclusion that the BR cross section σ in an oriented crystal can be expressed via a corresponding quantity for an amorphous medium σ_0 and represented as $\sigma = \sigma_0 P(r)$, where $P(r)$ is a function (normalized to unity and independent of the photon frequency) determining the dependence of the cross section on the distance r from electron to the atomic chain. However, it is still unclear whether the BR yield from an oriented crystal depends on the sample thickness, and there is no theoretical description of the orientation effects. The present study is devoted to these very problems.

For our purposes, it is sufficient to assume that the function $P(r)$ describing the dependence of the BR yield on the distance from the atomic chain in a crystal has a Gaussian character with a mean-square deviation equal to the amplitude of thermal oscillations of atoms in the crystal. The validity of this assumption has been analyzed in much detail by Nitta *et al.* in [7], where the dependence of the BR cross section for the axial channeling on the impact parameter was strictly described using the method of virtual photons and compared to the results of other researchers.

The assumptions about the Gaussian character of the $P(r)$ function and about uniform spatial distribution of electrons in the accessible transverse region [4] essentially imply that the cross section for the noncoherent BR of a channeled electron possessing the transverse energy ε can be expressed as $\sigma = \sigma_0 S_0/S(\varepsilon)$, where $S_0 = 1/Nd$ is the transverse area per atomic chain, d is the distance between neighboring atoms in the chain along the given direction, and $S(\varepsilon)$ is the transverse area accessible for the electron.

Passing from the cross section σ to the quantity $\nu = N\sigma$, which has the meaning of the probability of radiation per unit length, we can write an expression for the cross section of noncoherent BR per unit length for an electron with the transverse energy ε as

$$\nu(\varepsilon) = \frac{S_0}{S(\varepsilon)}\nu_0, \qquad (1)$$

where $\nu_0 = N\sigma_0$ and σ_0 is the BR cross section in an amorphous substance. According to this expression, an increase in the BR yield from an oriented crystal as compared to the amorphous medium is related to the fact that an electron with the transverse energy ε exhibits an $S_0/S(\varepsilon)$ times greater number of individual collisions with atoms of the crystal than does an electron with the same energy in the amorphous medium. This ratio strongly depends on the transverse energy and approximately amounts to 30–40 for $\varepsilon \sim -0.5U$, where U is the absolute value of the potential barrier for the axial channel in the crystal.

1063-7850/05/3101-0072$26.00 © 2005 Pleiades Publishing, Inc.

The cross section (1) should be averaged over the distribution function $F(\varepsilon, z)$ with respect to transverse energies at a given depth z:

$$\nu(z) = \nu_0 S_0 \int_{-U}^{\infty} \frac{F(\varepsilon, z)}{S(\varepsilon)} d\varepsilon. \quad (2)$$

Electrons with negative values of the transverse energy, $-U < \varepsilon < 0$, are channeled, which implies that their transverse trajectories are finite. The number of such channeled electrons at a depth z is

$$N_c(z) = \int_{-U}^{0} F(\varepsilon, z) d\varepsilon, \quad (3)$$

while the fraction of channeled electrons with $\varepsilon > 0$ is $N_q = 1 - N_c$. The distribution function $F(\varepsilon, z)$ is normalized to unity in the interval $-U < \varepsilon < \infty$.

An increase in the photon yield from an oriented crystal as compared to the amorphous substance is characterized by the ratio ν/ν_0.Using relation (2), we can express this ratio at a fixed depth z in the crystal as

$$\frac{\nu(z)}{\nu_0} = S_0 \int_{-U}^{0} \frac{F(\varepsilon, z)}{S(\varepsilon)} d\varepsilon + N_q(z), \quad (4)$$

where we have taken into account that unchanneled electrons have access to the entire transverse plane: $S(\varepsilon) = S_0$ ($\varepsilon > 0$).

Under the conditions of statistical equilibrium in the transverse phase space, the distribution function $F(\varepsilon, z)$ with respect to transverse energies is related to the distribution function $f(\mathbf{r}, \mathbf{p}, z)$ in the phase space as (see, e.g., [9])

$$df(\mathbf{r}, \mathbf{p}, z) = \frac{F[\varepsilon(\mathbf{r}, \mathbf{p}), z]}{2\pi m S[\varepsilon(\mathbf{r}, \mathbf{p})]} d\mathbf{r} d\mathbf{p}, \quad (5)$$

where $\varepsilon(\mathbf{r}, \mathbf{p}) = \mathbf{p}^2/2m + U(\mathbf{r})$; $\mathbf{r}$ and $\mathbf{p}$ are the transverse coordinate and momentum of electron; $m = m_0\gamma$; $\gamma = E/m_0c^2$ is the Lorentz factor of an electron with energy E; m_0 is the rest mass of an electron; and $U(\mathbf{r})$ is the continuous potential of an atomic chain.

For the following consideration, it is important to note that the distribution function $f(\varepsilon, z)$ has a relatively simple form. Indeed, to the first approximation, we may assume that electrons are uniformly distributed with respect to the transverse energy in the phase space [10], that is, $f(\varepsilon, z) = \alpha(z)$ for $\varepsilon < \varepsilon_m(z)$. The maximum value of the transverse energy, $\varepsilon_m(z)$, is determined by the multiple scattering of electrons on atoms and by the conditions on entrance into the crystal. Using relation (5), we obtain $F(\varepsilon, z) = 2\pi m\alpha(z)S(\varepsilon)$. Accordingly, the number of electrons in the channel is $N_c(z) = 2\pi m\alpha(z)\varepsilon_0 S_0$, where ε_0 is certain characteristic transverse energy of electrons in the channel, defined as

$$\varepsilon_0 = S_0^{-1} \int_{-U}^{0} S(\varepsilon) d\varepsilon. \quad (6)$$

Using the condition of normalization for $F(\varepsilon, z)$ on the interval $-U < \varepsilon < \varepsilon_m(z)$, we obtain an expression for the number of electrons at a depth z in the channel:

$$N_c(z) = \varepsilon_0/[\varepsilon_0 + \varepsilon_m(z)]. \quad (7)$$

If the axis of an electron beam with the angular divergence Δ is oriented along the crystal axis, then

$$\varepsilon_m(z) = \frac{E\Delta^2}{2} + \frac{E}{2}\left(\frac{\delta\theta^2}{\delta z}\right)_R z. \quad (8)$$

The second term in expression (8) reflects an increase in the transverse energy as a result of multiple scattering [5]. The factor $(\delta\theta^2/\delta z)_R$ determines the mean-square angle of multiple scattering in the amorphous medium (see, e.g., [5]). Expressions (7) and (8) differ from the corresponding formulas in [10] by taking into account the initial angular divergence of the electron beam at the entrance into the crystal.

The yield of radiation from a crystal of thickness z is given by an integral of expression (4) with respect to the thickness. Taking into account the above considerations, we eventually obtain the following expression for the factor determining an increase in the yield of noncoherent BR for an oriented crystal as compared to the amorphous substance:

$$\eta(z) = 1 + N_{eff}(z)(U/\varepsilon_0 - 1). \quad (9)$$

Here, $N_{eff}(z)$ is the effective number of electrons in the crystal of thickness z, defined as

$$N_{eff}(z) = \frac{1}{z}\int_0^z N_c(z')dz', \quad (10)$$

where the meaning of the integral consists in determining the characteristic channeling length $L_{eff}(z)$ [11] for electrons in the crystal.

Thus, the factor of increase $\eta(z)$ in the yield of noncoherent BR for an oriented crystal is determined by the effective number of electrons in the channel. This number, in turn, depends on the initial angle of entrance of electrons into the crystal and on their angular divergence. According to expressions (9) and (10), the value of $N_{eff}(z)$ at large z decreases slower than $1/z$. Indeed, $N_{eff}(z) \sim (\ln z)/z$ for $z \longrightarrow \infty$. Therefore, the phenomenon of BR yield enhancement in crystals may take

place even for very large thicknesses $z \gg z_c$, where $z_c = \theta_L^2/(\delta\theta^2/\delta z)_R$ is the characteristic dechanneling length.

The factor $U/\varepsilon_0 - 1$ in expression (9) weakly depends on the crystal type. In particular, it amounts to 11.6 for the ⟨110⟩ direction in silicon. For 1.2-GeV electrons in such a crystal with a thickness of 500 μm ($z_c \approx 53$ μm), the effective channeling length according to expressions (7) and (10) is $L_{eff} \approx 9$ μm and the effective number of electrons in the channel is $N_{eff} \approx 0.018$ (for an initial divergence of $\Delta = \pm 1.3\theta_L$). Under these conditions, the BR yield enhancement factor (9) is $\eta \approx 1.2$, which agrees perfectly with the experimental results [6].

Formulas (7), (9), and (10) can be readily generalized to provide for a more correct selection of the distribution function with respect to transverse energies in the phase space. In particular, it is possible to select a canonical distribution $f(\varepsilon, z) \sim \exp(-\beta\varepsilon)$. However, this does not offer many advantages from the standpoint of elucidation of the physics of events. It should be noted that formula (7) somewhat overstates the number of electrons in the channel for $z \ll z_c$ as compared to the results of numerical simulation [10] and, on the contrary, understates this number for $z \gg z_c$. Nevertheless, the proposed simple model ensures a quite satisfactory qualitative description of the character of the dependence of the noncoherent BR yield on the crystal thickness.

REFERENCES

1. M. A. Kumakhov, Phys. Lett. A **57**, 17 (1976).
2. G. L. Bochek, I. A. Grishaev, G. D. Kovalenko, *et al.*, Pis'ma Zh. Éksp. Teor. Fiz. **32**, 380 (1980) [JETP Lett. **32**, 355 (1980)].
3. J. Lindhard, Mat. Fys. Medd. K. Dan. Vidensk. Selsk. **34** (14), 1 (1965).
4. M. A. Kumakhov, Usp. Fiz. Nauk **115**, 427 (1975) [Sov. Phys. Usp. **18**, 203 (1975)].
5. V. V. Beloshitskiĭ and M. A. Kumakhov, Zh. Éksp. Teor. Fiz. **82**, 462 (1982) [Sov. Phys. JETP **55**, 265 (1982)].
6. I. Endo, T. Monaka, A. Sakaguchi, *et al.*, Phys. Lett. A **146**, 150 (1990).
7. H. Nitta, K. Shimizu, and Y. H. Ohtsuki, Radiat. Eff. Defects Solids **122**/**123**, 383 (1991).
8. A. Sorensen, in *Relativistic Channeling*, Ed. by R. A. Carrigan, Jr. and J. A. Ellison (Plenum, New York, 1987), pp. 331–337.
9. M. Kh. Khokonov, Zh. Éksp. Teor. Fiz. **103**, 1723 (1993) [JETP **76**, 849 (1993)].
10. M. Kh. Khokonov, Zh. Tekh. Fiz. **64**, 181 (1994) [Tech. Phys. **39**, 330 (1994)].
11. M. A. Kumakhov, Phys. Lett. A **145**, 195 (1990).

Translated by P. Pozdeev

Technical Physics Letters, Vol. 31, No. 1, 2005, pp. 75–76. Translated from Pis'ma v Zhurnal Tekhnicheskoĭ Fiziki, Vol. 31, No. 2, 2005, pp. 63–66.

Using Intrinsic Gallium Arsenide Oxide for Insulating Active Elements in GaAs-Based Integrated Circuits

N. G. Lezhava, A. P. Bibilashvili, and A. B. Gerasimov

Tbilisi State University, Tbilisi, Georgia

e-mail: amiranbib@yahoo.com

Received April 19, 2004

Abstract—A new method for insulating the active elements of GaAs-based integrated circuits (ICs) is proposed, which is based on the use of intrinsic gallium arsenide oxide formed by plasma anodizing assisted with UV irradiation. This insulation provides a significant decrease in the level of leak currents and the parasitic substrate feedback, ensures an increase in the thermal stability and breakdown field strength, and is adapted to planar IC technology. © *2005 Pleiades Publishing, Inc.*

A factor of key importance in GaAs-based VLSI technology is the high quality of insulation between active elements of integrated circuits (ICs). Otherwise, there frequently arises a parasitic substrate feedback control (SFC), whereby the current–voltage characteristic of a Schottky-gate field-effect transistor (SGFET) exhibits uncontrolled variations at a negative bias voltage applied to the insulated electrode on a semi-insulating substrate. For SGFETs operating in a depletion regime, an increase in the control voltage V_1 applied to the insulated drain electrode leads to a decrease in the drain current. The main SFC parameters are (i) the relative change $\Delta I/I_0$ in the drain current and (ii) the leak current I' between SGFET and the control electrode. The applied control voltage V_1 gives rise to a hysteresis in the current–voltage characteristic, a drift in the drain current, and a low-frequency noise, which are important characteristics of GaAs-based SGFETs [1].

The SFC mechanism is related to the formation of a space charge region at the channel–substrate interface, in which a negative charge is concentrated in the substrate, and a positive charge, in the *n*-type layer. Application of a negative voltage to the control electrode leads to the injection of electrons, which are accumulated at the SGFET source, thus adding a negative charge to that existing under the channel. As a result, the space charge region will intensively increase with the field, in proportion to the density of injected electrons. This, in turn, leads to a further growth of SFC and a decrease in the saturation current [2, 3].

Traditional methods of insulation adopted in GaAs-based IC technology, such as mesa etching and ion implantation, influence SFC only to a limited extent. This is related to a significant residual conductivity in mesa etched surfaces and insufficient penetration depth of implanted ions in the substrate. In both cases, the SFC amounts to ≈20% at a control voltage of –20 V [3].

This Letter reports on the results of SFC measurements in ICs with the active elements insulated using intrinsic gallium arsenide oxide formed by plasma anodizing assisted with UV irradiation [4].

The experiments were performed with epitaxial structures based on [100]-oriented *n*-GaAs doped with tellurium to $N_D = 2 \times 10^{17}$ cm^{-3}. The intrinsic gallium arsenide oxide comprises a mixture of Ga_2O_3 (64%) and As_2O_3 (36%). The oxide film thickness was about 1 μm. The process of plasma anodizing assisted with UV irradiation was performed in galvanostatic regime at a substrate temperature of 450 K. The UV photon energy was 5 eV and the intensity was limited so as to eliminate damage to the GaAs surface. The control electrode was spaced from the SBFET gate by 2.0 μm. The maximum control voltage amplitude was V_1 = 20 V. The SFC was evaluated in the dark and on exposure of the IC structure to white light.

As can be seen from the typical plots of the relative variation of the saturation drain current and the leak current from SGFET to control electrode versus control voltage (see figure) the SFC signal level in the dark reaches about 2% for the maximum V_1 value, while the leak current is two orders of magnitude lower than that in the IC structure insulated by fluorine implantation [3]. Exposure of the IC structure to white light increases both SFC and the leak current, but their relative values are still much lower than those obtained using other methods of insulation [1]. It should be also noted that the insulation of active elements using intrinsic gallium arsenide oxide is characterized by good thermal stability, ensures high breakdown field strength, and is adapted to planar IC technology, which ensures an increase in the degree of integration.

1063-7850/05/3101-0075$26.00 © 2005 Pleiades Publishing, Inc.

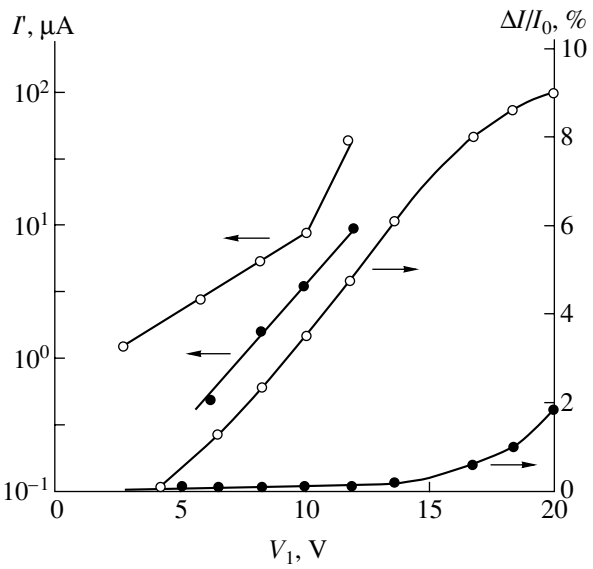

Typical plots of the relative variation of the saturation drain current $\Delta I/I$ and the leak current I' from SGFET to control electrode versus control voltage V_1 (●) in the dark and (○) under illumination with white light.

Advantages of insulation using intrinsic gallium arsenide oxide are explained both by a high resistivity of this oxide, which increases the insulating effect, and by the fact that a fixed negative space charge formed in this oxide leads to the formation of an electron-depleted region along the entire boundary with GaAs. This depletion additionally increases the resistance to electron current along the entire boundary, which sharply reduces the SFC level.

In conclusion, the insulation of active elements by intrinsic gallium arsenide oxide formed using plasma anodizing assisted with UV irradiation significantly decreases the SFC level and the leak currents, ensures good thermal stability and reproducibility of ICs, and eliminates the diffusion of gallium into dielectric films (the factor leading to breakdown). This method of insulation offers a promising direction in the development of GaAs-based ICs.

REFERENCES

1. L. V. Khvedelidze and N. P. Khuchua, Zarubezhn. Élektron. Tekh., No. 9, 69 (1987).
2. S. Spiram and M. B. Das, Solid-State Electron. **28**, 979 (1985).
3. E. Y. Chang, C. S. Fuh, C. C. Meng, *et al.*, IEEE Trans. Electron Devices **37**, 1134 (2000).
4. S. V. Baras'ev, A. P. Bibilashvili, and A. B. Gerasimov, USSR Inventor's Certificate No. 1172412, HO1 L24 (1985).

Translated by P. Pozdeev

Technical Physics Letters, Vol. 31, No. 1, 2005, pp. 77–78. Translated from Pis'ma v Zhurnal Tekhnicheskoĭ Fiziki, Vol. 31, No. 2, 2005, pp. 67–71.

Antireflection Properties of Erbium Oxide Films

V. A. Rozhkov* and M. A. Rodionov

Samara State University, Samara, Russia

** e-mail: rozhkov@ssu.samara.ru*

Received July 9, 2004

Abstract—We have studied the optical transmission spectrum of a surface film of erbium oxide and evaluated the effect of clarification for the surface of a silicon-based photovoltaic converter with an antireflection coating of this material. It is established that erbium oxide films are highly transparent in a broad wavelength range from 250 to 1050 nm and ensure a decrease in the coefficient of reflection of a silicon surface down to 1–4.5%. The antireflection coating of erbium oxide increases the short-circuit photocurrent of the silicon-based photovoltaic converter by more than 38%. © *2005 Pleiades Publishing, Inc.*

A large coefficient of light reflection (35–40%) from the surface of silicon in the effective spectral range of photovoltaic devices (400–1100 nm) makes it necessary to apply clarification (antireflection) coatings on the working surfaces of silicon-based photovoltaic converters [1]. Promising dielectric materials suitable for the formation of such antireflection coatings on silicon-based devices are offered by rare earth (RE) oxides. The RE oxides are advantageous to other candidate materials by being highly transparent in the working spectral range, showing high chemical and thermal stability, and possessing an optimum index of refraction for these applications [2]. However, the optical and antireflection properties of RE oxides in the form of thin films are still insufficiently studied.

This Letter presents the results of investigation of the optical characteristics of erbium oxide films and evaluation of the clarification effect achieved using antireflection coatings of this material on the surface of silicon and related photovoltaic converters.

Films of erbium oxide were prepared on the surfaces of polished silicon and quartz plates preliminary coated by erbium and then subjected to thermal oxidation in air at 600°C. The initial films were deposited in a VUP-5 vacuum system by thermal evaporation of the RE metal from a molybdenum boat at a residual pressure of $(2–3) \times 10^{-5}$ Torr. The effect of clarification of a silicon surface was studied for the erbium oxide films formed on n^+–p–p^+-Si structures with an n^+-type layer having a thickness of 0.2–0.5 μm. The resistivity of the p-type base region was 10 Ω cm. The p^+-type was boron-doped to an impurity concentration of 8×10^{19} cm^{-3} by means of implantation with 30-keV boron ions at a beam current density of 2 mC/(s cm^2). The n^+-type region was created by phosphorus diffusion from PCl_3 at 860–900°C. The donor concentration on the n^+-type layer surface was 6×10^{19} cm^{-3}. The current-collector stripe contacts on this layer were prepared by vacuum deposition of aluminum via a mask.

The optical transmission spectra of erbium oxide films were measured using an SF-26 spectrophotometer, and the reflection spectrum was studied with the aid of an FO-1 reflection photometer. The clarification effect of an erbium oxide film on the silicon surface was evaluated by measuring the short-circuit photocurrent of the n^+–p–p^+-Si structure.

Films of erbium oxide exhibit high mechanical strength, good adhesion to the surfaces of both quartz and silicon, and substantial hardness (not scratched by a steel needle). The results of X-ray and electron diffraction measurements showed that the oxide films obtained by thermal oxidation of preliminary deposited RE metal layers possess a fine-grained structure with an average grain size of 10^{-7} cm. Heat treatment of the vacuum-deposited metal film in oxygen or in air leads to the formation of an RE sesquioxide with a structure generally coinciding with that of a powdered compound [2].

Figure1 shows the spectrum of transmission T of an erbium oxide film prepared on a quartz substrate and the spectra of reflection coefficient R for a silicon surface and an erbium oxide film–silicon structure. In order to compensate for distortions related to the light absorption and reflection from the rear side of the quartz substrate, the intensity of light transmitted through the uncoated substrate was considered as corresponding to a 100% level. As can be seen from Fig. 1, the erbium oxide film on quartz is highly transparent in the wavelength range from 250 to 1050 nm, the maximum transmission coefficient exceeding 94%. The observed variation in the transmission coefficient depending on the wavelength is related to the interference phenomena in the film. Strong absorption in the range of photon energies above 5.2 eV is due to the fundamental absorption corresponding to interband transitions. The high transparency of the erbium oxide film in

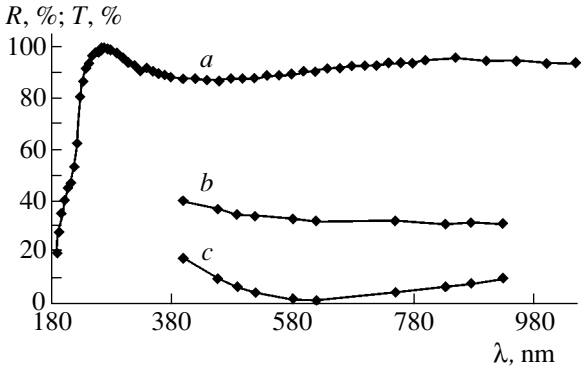

Fig. 1. The spectra of (*a*) the optical transmission *T* of an erbium oxide film on a quartz substrate and (*b*, *c*) the reflection coefficient *R* of a silicon substrate surface an erbium oxide film on this surface, respectively.

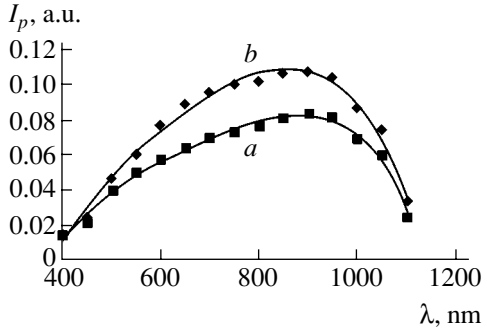

Fig. 2. The spectra of short-circuit photocurrent (normalized with respect to the incident radiation power) measured for n^+–p–p^+-Si structures (*a*) without and (*b*) with an antireflection coating of erbium oxide.

the visible spectral range and a sharp fundamental absorption edge indicate that the film composition is close to stoichiometric.

The data in Fig. 1 show that an antireflection coating of erbium oxide formed on the surface of silicon decreases in the coefficient of reflection of a monochromatic light from 32–34% (for the uncoated surface) down to 1–4.5% and nearly eliminates reflection from the semiconductor surface. An analysis showed that the integral coefficient of light reflection from the surface of silicon clarified by an erbium oxide film in the range of wavelength from 400 to 927 nm decreases from 34 to 7%.

Figure 2 presents the spectra of short-circuit photocurrent measured for n^+–p–p^+-Si structures without and with an antireflection coating of erbium oxide, normalized with respect to the incident radiation power. Using these experimental data, the relative increase in the short-circuit photocurrent was calculated by the formula

$$K = \frac{I_p - I_p^*}{I_p^*} \times 100\%,$$

where I_p and I_p^* are the short-circuit photocurrents measured for the n^+–p–p^+-Si structure with and without the antireflection coating, respectively. The results of such calculations showed that use of the erbium oxide films increases the spectral photocurrent response of the silicon-based photovoltaic converter by more than 38% at a wavelength of 650 nm. On the whole, application of an antireflection coating of erbium oxide increased the integral responsivity of this converter in the 400–1100 nm spectral range by 30–32%.

Thus, the results of our investigation show good prospects for using erbium oxide films as antireflection coatings on silicon-based photovoltaic devices.

REFERENCES

1. M. M. Koltun, *Solar Cells* (Nauka, Moscow, 1987) [in Russian].
2. O. S. Vdovin, Z. I. Kir'yashkina, V. N. Kotelkov, *et al.*, *Rare Earth Oxide Films in MIM- and MIS-Structures* (Saratov State University, Saratov, 1983) [in Russian].

Translated by P. Pozdeev

Technical Physics Letters, Vol. 31, No. 1, 2005, pp. 79–80. Translated from Pis'ma v Zhurnal Tekhnicheskoĭ Fiziki, Vol. 31, No. 2, 2005, pp. 72–76.

A Specific Feature of Unipolar Rotation

S. A. Gerasimov, S. L. Gorokhovikov, and M. A. Grigoryan

Rostov State University, Rostov-on-Don, Russia

e-mail: GSIM1953@mail.ru

Received July 6, 2004

Abstract—It has been experimentally demonstrated that the moment of forces inherent in unipolar rotation is independent of the form of the mobile and external circuits. The torque of unipolar rotation depends only on the current, the properties of the magnetic field source, and the distance from the points of current supply to the mobile electrode to the magnetic field source. © *2005 Pleiades Publishing, Inc.*

Rotation of a cylindrical magnet, in which a dc current flows from the center to the edge, is called unipolar [1]. It is believed that a specific feature of this motion is violation of the principle of equality between action and counteraction in magnetostatics [2, 3]. Experimental investigations of this phenomenon [4] revealed extremely small values of the torque (or the moment of forces) acting upon the system. Apparently, this factor accounts for a rather scornful treatment of not only the hypothesis, but of the phenomenon as a whole. However, these are the only well-known experimental data, which can be compared to theoretical notions [3]. Other results [5] refer, as a rule, to particular technical solutions and do not allow the most general features of this type of motion, possessing both applied and basic significance, to be elucidated.

Apparently, the adopted scheme of the experiment is rather unfavorable. The traditional construction [1–4] is not suited for investigations of the relationship between the rotational moment and the distance between a magnetized cylindrical body and a disk in which the dc current is flowing. We believe that, in the experimental study of unipolar rotation, it would be expedient to set constant the distance from the magnetic field source to all parts of the external circuit, for example, as in the scheme presented in Fig. 1.

The experimental setup comprises a mobile electrode, a circular magnet *M*, and a cell *V* with electrically conducting liquid. The mobile electrode consists of a thin-walled cylindrical copper electrode *E* with a radius of 65 mm and a height of 110 mm, a central copper electrode *C* with a diameter of 7 mm, and an aluminum disk electrode *D* with a thickness of 8 mm. The dimensions of the disk electrode are selected so as to ensure electric contact between the cylindrical electrode and the central electrode irrespective of the variable distance δ from the upper surface of magnet *M* to the lower surface of disk *D*. A circular magnet with a height of 25 mm, an internal diameter of 38 mm, an external diameter of 110 mm, and a magnetization of 2×10^5 A/m, is mounted on a plastic substrate *P* rigidly connected to the cylindrical electrode. The mobile electrode is suspended by thread *T*. This is done only in order to reduce the friction that was an interfering factor in the preceding measurements [2, 4]. The lower bases of the cylindrical and central electrodes are immersed into an electrically conducting liquid (a 5% solution of $CuSO_4 \cdot 5H_2O$) filling two cylindrical compartments (L_+ and L_-, separated by a spacer) in cell *V*. The depth of immersion is about 5 mm. Copper disk (S_+) and ring (S_-) placed on the cell bottom are used to supply a dc electric current from an external source to the electrically conducting liquid.

This variant of the experimental exhibits a rather large torque *N*. For example, for a current of 1 A and a distance of δ = 1 cm, the torque exceeds 500 (g cm^2)/s^2. The whole array of experimental data, representing the torque measured as a function of the current *I* for various values of δ, is presented in Fig. 2. The torque was measured using the torsional pendulum technique. The calculated moment of inertia and the measured period

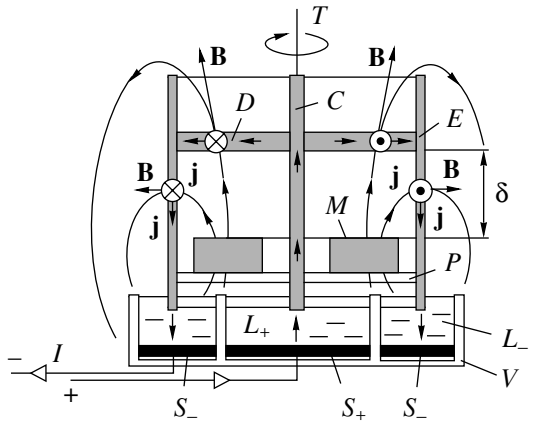

Fig. 1. Schematic diagram of the experimental setup: arrows ↑ and ↓ indicate the directions of electric current flow; symbols ⊗ and ⊙ indicate the directions of forces acting upon various parts of the mobile electrode (see the text for explanations).

1063-7850/05/3101-0079$26.00 © 2005 Pleiades Publishing, Inc.

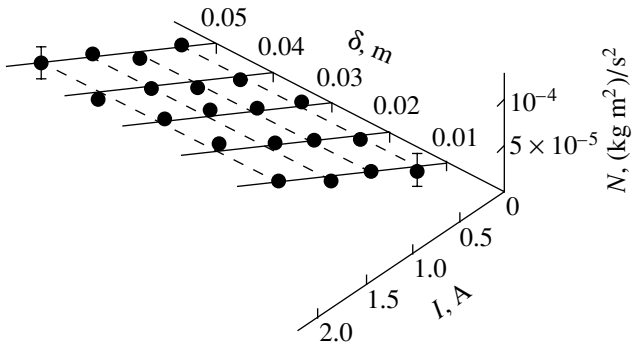

Fig. 2. Experimental dependence of the moment of forces N acting on the mobile electrode on the current I for various values of the distance δ between the magnetic field source and the disk electrode. Solid lines show the approximation $N = \alpha I$, where $\alpha = 5 \times 10^{-5}$ (kg m^2)/(s^2 A).

of torsional vibrations were used to determine the torsion modulus relating the torque to the angle of rotation of the mobile electrode. In application to the problem under consideration, use of the method of torsional pendulum was discussed in [6]. This method has proved quite adequate in its results.

Now we have all grounds to doubt the previous results, with respect to both their character and the numerical results. First, the dependence of the torque on the current is linear, at least for small values of the current flowing in the circuit. Second (but most important), the torque is independent of the position of disk electrode D or, in other words, of the distance δ between the magnetic field source and the disk electrode. From this we infer a more general result: the torque is independent of the form and dimensions of the mobile electrode. Small deviations from this rule are probably related to the errors of measurements and secondary factors (e.g., variation of the properties of $CuSO_4 \cdot 5H_2O$ solution in the course of measurements). The fact that the torque N is independent of δ is illustrated in Fig. 2 by the dashed lines parallel to the axis of distances.

Physically, the external circuit has no substantial distinctions from the mobile circuit. Therefore, the moment of forces acting upon the external circuit has to be also independent of the form of this circuit. This, in turn, implies that the torque is not influenced by the character of current distribution in the electrically conducting liquid (including those induced by the magnetic field).

The only system dimensions on which the torque depends are the distance from the magnetic field source to the regions of cylindrical and central electrodes occurring in the electrically conducting liquid, that is, to the points of current supply to the mobile electrode. This conclusion, along with large values of the torque observed in our experiments, may be extremely important for the design and development of such devices. On the other hand, the main result of this study is that the notions about the so-called self-action [7, 8] have not lost their meaning.

REFERENCES

1. P. Lorrain, Eur. J. Phys. **11**, 94 (1990).
2. S. Bednarek, Am. J. Phys. **70**, 455 (2002).
3. S. A. Gerasimov and S. L. Gorokhovikov, Vopr. Prikl. Fiz. **10**, 14 (2004).
4. A. K. Das Gupta, Am. J. Phys. **31**, 428 (1963).
5. D. A. But, Élektrichestvo, No. 1, 2 (1995).
6. S. A. Gerasimov and A. V. Volos, Uchebn. Fiz., No. 5, 22 (2002).
7. S. A. Gerasimov, Phys. Scr. **56**, 462 (1997).
8. G. Cavalleri, G. Bettoni, E. Tonni, and G. Spavieri, Phys. Rev. E **58**, 2505 (1998).

Translated by P. Pozdeev

Technical Physics Letters, Vol. 31, No. 1, 2005, pp. 81–83. Translated from Pis'ma v Zhurnal Tekhnicheskoĭ Fiziki, Vol. 31, No. 2, 2005, pp. 77–83.

Nonlinear Suppression of Microwave Signals in a Resonant Magnetostatic Wave Transmission Line

S. V. Grishin and Yu. P. Sharaevskiĭ*

Saratov State University, Saratov, Russia

** e-mail: sharaevskyyp@info.sgu.ru*

Received July 15, 2004

Abstract—We have studied the phenomenon of suppression of a microwave signal in a magnetostatic wave (MSW) resonant transmission line comprising a microstrip resonator with a tangentially magnetized ferromagnetic film. Distinctions are revealed between the observed effects and those reported for a matched MSW line transmitting one microwave signal or two signals with different power levels. © *2005 Pleiades Publishing, Inc.*

It has been reported (see, e.g., [1–3]) that a microstrip transmission line with a ferromagnetic film exciting surface magnetostatic waves (MSWs) exhibits the unique ability to produce nonlinear suppression for microwave signals of different power levels. In particular, signals with a power level above a certain threshold (large signals) are attenuated to a lower extent than signals with a power below the threshold (small signals). This nonlinear effect, related to the parametric excitation of short spin waves in a ferromagnetic film, underlies the operation of nonlinear microwave MSW devices, called signal-to-noise enhancers or noise limiters [1, 2, 4].

This Letter presents the results of experimental investigation of the phenomenon of microwave signal suppression in a nonlinear MSW transmission line, in which a matched microstrip line is replaced by a microstrip resonator exciting a backward volume MSW (BVMSW) in the ferromagnetic film.

The experimental prototype (see the inset to Fig. 1) comprises a microstrip half-wave transmission type resonator, with an yttrium iron garnet (YIG) film arranged along the symmetry axis. The resonator was fabricated by means of thin-film photolithography on an 0.5-mm-thick alumina ceramics substrate and had a microstrip width of w = 0.5 mm. The fundamental mode of the microstrip resonator had a resonance frequency of f_0 = 2117 MHz, a loaded Q value of Q_L = 141, and an attenuation factor at the resonance frequency A_0 = 12.3 dB. A YIG film with dimensions 6 × 10 × 0.04 mm was characterized by a saturation magnetization of $4\pi M_0$ = 1680 G and a loss factor of $2\Delta H$ = 0.69 Oe. At a constant magnetic field of $H_0 \cong$ 300 Oe applied tangentially to the system surface and perpendicularly to the microstrip, the film excited BVMSWs at frequencies of the fundamental mode of the resonator. The experimental amplitude–frequency and phase–frequency characteristics of such a resonant transmission line measured in a linear regime were reported in [5], where the system behavior was described using a model comprising two coupled oscillatory circuits, one representing the microstrip resonator and the other, the YIG film with excited BVMSWs.

Figure 1 shows the plots of the quantity $G = A_s - A_l$, characterizing the difference between the transmission factors for the small (A_s) and large (A_l) signals, versus the frequency f for the resonant transmission line under consideration (Fig. 1a) and for a matched microstrip line (Fig. 1b). The power level of the small signal (P_s = 1 μW) corresponded to a linear regime of both transmission lines, while the large signal power (P_l = 128 mW) corresponded to a saturation regime in which no significant changes in the amplitude–frequency characteristics of the lines take place. The transmission factor was determined using an R4-23 vector network analyzer (Russia). The microwave signal power was amplified using a solid-state amplifier with a gain of ~30 dB and an output saturation power of 200–250 mW. The input signal power level was monitored by an M3-51 power meter. The complex transmission coefficient values for each signal power level were measured in a manual frequency set regime with a frequency step of 10 MHz.

As can be seen from results presented in Fig. 1a, the G versus f plot for the resonant BVMSW transmission line (curve *1*) can be divided into two significantly different regions. One region corresponds to the frequency range where $G < 0$, which implies that small signals are attenuated to a greater extent than large signals. Another region corresponds to $G > 0$, so that large signals are attenuated more strongly than small signals. Therefore, the first frequency region makes possible the effective suppression of small signals relative to the large ones ($G \sim -15$ dB), while the second frequency region features effective limitation of large signals relative to small ones ($G \sim +9$ dB) even at a relatively small YIG film–microstrip overlap (l = 6 mm). It should be noted that the region of effective suppression of

1063-7850/05/3101-0081$26.00 © 2005 Pleiades Publishing, Inc.

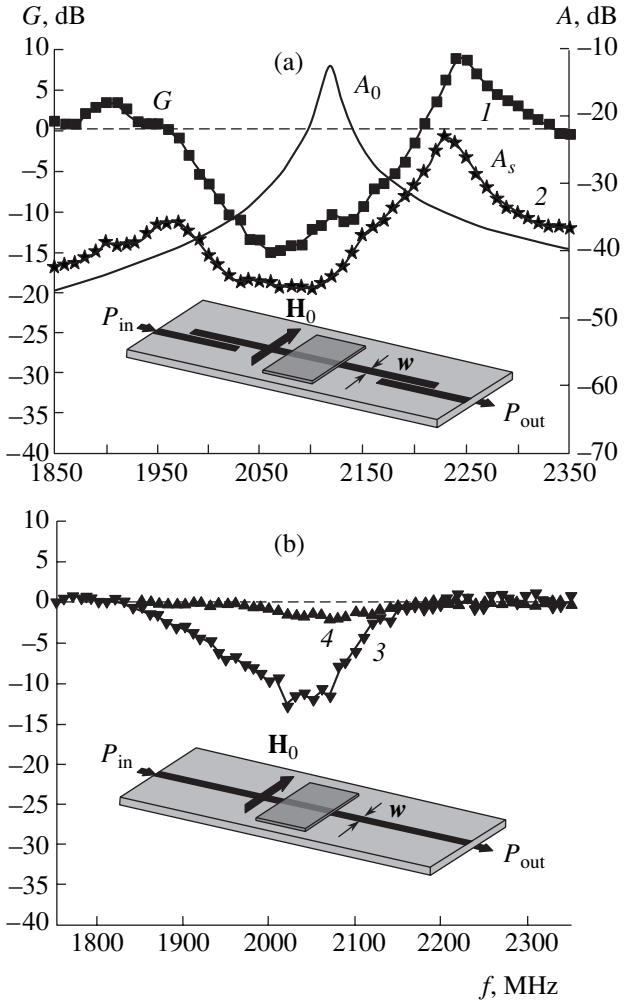

Fig. 1. Plots of the microwave signal suppression factor G versus frequency for (a) a resonant BVMSW transmission line with a YIG film–microstrip overlap of l = 6 mm (curve *1*) and (b) a matched BVMSW line with l = 6 mm (curve *4*) and 54 mm (curve *3*). Dashed lines show a zero suppression level. Solid curve A_0 shows the amplitude–frequency characteristic of a microstrip resonator without YIG film; curve *2* (A_s) is the characteristic of the microstrip resonator with BVMSWs excitation.

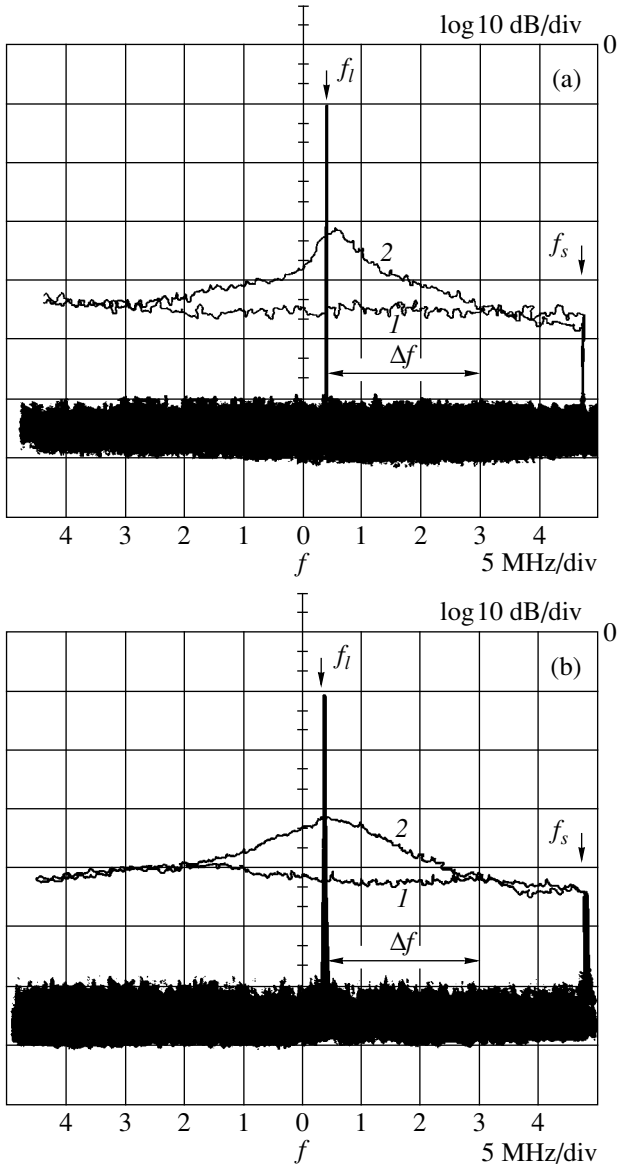

Fig. 2. Spectrograms of large and small signals transmitted via (a) the resonant BVMSW line with l = 6 mm and (b) the matched BVMSW line with l = 54 mm: (*1*) small-signal envelope in the absence of a large signal; (*2*) small-signal envelope in the presence of a large signal.

small signals relative to large ones falls within the frequency band of the fundamental mode of the microstrip resonator (see solid curve in Fig. 1a), while the regions of large signal limitation mostly fall within the regions of resonance frequencies of a two-circuit system (curve *2* in Fig. 1a).

For comparison, Fig. 1b shows the plots of G versus f obtained upon replacing the microstrip resonator by a matched microstrip line with an analogous microstrip size (w = 0.5 mm). As can be seen, the resonant line provides for a much more effective suppression of small signals as compared to that in the matched line with the same film parameters (for l = 6 mm, the maximum level of suppression in the latter case is $G \sim -2$ dB). In the system with a matched microstrip line, the level of suppression of small signals comparable to that in a resonant BVMSW line could be achieved at a significantly greater YIG film–microstrip overlap (see curve *3*). Note also that the matched BVMSW line at these frequencies does not limit large signals. It was shown [2] that such a region may exist near the frequency boundary of the first-order parametric processes.

Figure 2 shows spectrograms illustrating the simultaneous transmission of two signals (large, P_l = 128 mW; small, P_s = 0.5 mW) via the resonant and

matched BVMSW lines. These spectrograms in the two-signal regime were obtained using a C4-60 spectrum analyzer, which made it possible to evaluate changes in the small signal amplitude in the course of variation of the small signal frequency near a fixed frequency of the large signal (f_l = 2060 MHz). In the course of f_s variation, the spectrum analyzer was operating in the storage regime and the P_s value was maintained constant. The signals were generated by two G4-79 microwave oscillators, with a solid-state amplifier connected to the output of one oscillator.

The results presented in Fig. 2 show that a region of frequencies where the large signal significantly influences the small signal amplitude in both cases is about $\Delta f \cong 26$ MHz. However, for the line with a resonator, the envelope of the small signal amplitude has a width (on a 3 dB level) of $\Delta f_{3\,\mathrm{dB}} \cong 3$ MHz (Fig. 2a), while the matched line has a significantly greater width of $\Delta f_{3\,\mathrm{dB}} \cong 8.5$ MHz (Fig. 2b).

Thus, the results of our investigation demonstrated the possibility of effective suppression of small signals relative to large ones using resonant BVMSW transmission limes with relatively small ferromagnetic films.

Acknowledgments. This study was supported within the framework of the Federal Program "Universities of Russia: Basic Research" (project no. UR.01.01.052), by a joint grant from the Ministry of Education of the Russian Federation and the US Civilian Research and Development Foundation for Independent States of the Former Soviet Union (BRHE, REC-006), and by the Russian Foundation for Basic Research (project no. 04-02-16296).

REFERENCES

1. A. V. Vashkovskiĭ, V. S. Stal'makhov, and Yu. P. Sharaevskiĭ, *Magnetostatic Waves in Microwave Electronics* (Saratov State University, Saratov, 1993) [in Russian].
2. J. D. Adam and S. N. Stitzer, Appl. Phys. Lett. **36**, 485 (1980).
3. S. N. Stitzer, IEEE Trans. Magn. **19**, 1874 (1983).
4. T. Kuki and T. Nomoto, IEICE Trans. Electron. **E82-C**, 1654 (1999).
5. S. V. Grishin, V. S. Grishin, V. V. Gurzo, and Yu. P. Sharaevskiĭ, Radiotekh. Élektron. (Moscow) **48**, 724 (2003).

Translated by P. Pozdeev

Technical Physics Letters, Vol. 31, No. 1, 2005, pp. 84–85. Translated from Pis'ma v Zhurnal Tekhnicheskoĭ Fiziki, Vol. 31, No. 2, 2005, pp. 84–88.

Molecular-Dynamics Study of the Features of Dynamic Vortex Structure Formation in a Material with Micropores under High-Rate Deformation Conditions

A. I. Dmitriev* and S. G. Psakhie

Institute of Strength Physics and Materials Science, Siberian Division, Russian Academy of Sciences, Tomsk, 634055 Russia

** e-mail: dmitr@usgroups.com*

Received August 16, 2004

Abstract—The response of a material containing a system of micropores subjected to high-rate shear deformation has been computer-simulated by methods of molecular dynamics. Deformation of such materials is accompanied by the formation of vortexlike dynamic defects. This process can be divided into three stages. The first stage is characterized by a predominating laminar character of atomic displacements in the regions adjacent to the loaded layers. A special feature of the second stage is the development of a correlated vortexlike motion of atoms in the regions between micropores, with periodic formation and breakage of vortices in a period on the order of several picoseconds. The third stage is related to the loss stability of the atomic structure and the formation of deformation localization bands. This is accompanied by the loss of correlation of the vortexlike motion of atoms in the regions between micropores. The results can be used in analyzing the behavior of materials under conditions involving irradiation. © *2005 Pleiades Publishing, Inc.*

Using computer simulation techniques in investigations of the behavior of materials on a nanoscale is of importance in both basic and applied aspects, since direct experimental study of the mechanisms of deformation on the atomic level encounters considerable difficulties not only because of insufficient spatial resolution of the available methods, but also because of the very small duration (comparable with the characteristic Debye times) of processes on this level. As is known, the presence of structural inhomogeneities in a material may switch on the mechanisms of deformation involving the formation of so-called dynamic defects [1–4]. These defects, representing correlated motion of a rather large number of atoms, exist only at certain stages of the process of dynamic loading and provide for a consistent pattern of atomic displacement. The appearance of dynamic defects is usually related to special features of the material structure and the regime of loading.

The aim of this study was to assess the possibility of formation of dynamic defects in materials with micropores. For this purpose, we simulated the behavior of a three-dimensional copper crystal with pores under dynamic loading conditions using the method of molecular dynamics.

The model crystal had the shape of a parallelepiped with edges parallel to the crystallographic directions [100], [010], and [001] and equal to 150, 120, and 80 atomic units of length (1 a.u. ~ 0.53×10^{-10} m). The total number of atoms in the crystal exceeded 20000. The external loading was simulated by setting constant velocities to atoms in the three edge atomic planes on each side along the [010] direction; in the [100] direction, the velocity projections were set at 25 m/s for the uppermost atomic layer and –25 m/s for the bottom layer; in the other directions, the velocity components were set to zero. In this way, we modeled a high-rate shear deformation in the [100] direction with a relative velocity of 50 m/s. We used periodic boundary conditions in the [100] direction and simulated free boundaries in the [001] direction. These boundary conditions corresponded to the shear deformation of a crystal with a system of micropores, elongated in the [100] direction. The interatomic interactions were described within the framework of the method of embedded atoms [5]. In order to avoid the induced effects related to the symmetry of the ideal crystal lattice, the model copper crystal was initially heated to 100 K. The load was applied when the atomic structure relaxed so as to reach an equilibrium state corresponding to this temperature.

Behavior of the atomic subsystem upon loading was analyzed, in particular, by constructing the atomic configurations of the crystal at various times and the patterns of atomic displacements in the crystal over various time intervals.

Analysis of the simulation results showed that deformation of the model crystal with a system of micropores is accompanied by the correlated vortexlike motion of atoms, which can be interpreted as the dynamic defect formation. In the case under consider-

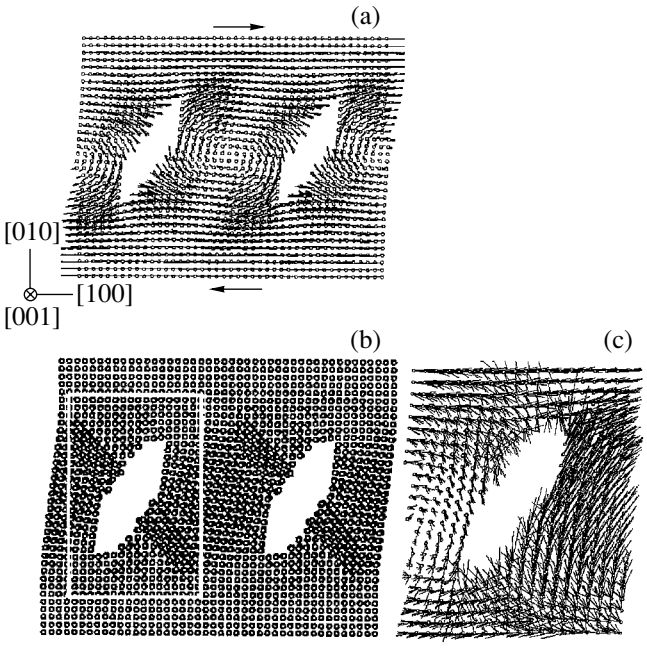

Fig. 1. (a) The pattern of atomic displacements in the model crystal over the period of time $(6.05–9.68) \times 10^{-12}$ s (arrows indicate the direction of deformation); (b) the structure of the model crystal at $t = 12.09 \times 10^{-12}$ s; (c) atomic displacements in a fragment of the crystal (framed in Fig. 1b) over the period of time $(10.89–14.51) \times 10^{-12}$ s. The scales of displacements in Figs. 1a and 1c are increased by a factor of five.

ation, the process of deformation developing in the crystal can be divided into three stages. At the first stage, the presence of micropores in the crystal does not significantly influence the behavior of atoms, which has on the whole a "laminar" character.

The second stage is characterized by the development of a correlated vortexlike motion of atoms in the central region between micropores. Figure 1a shows the pattern of projections of atomic displacements onto the [001] plane at a moment of time corresponding to this stage. It should be noted that the presence of micropores (i.e., internal surfaces) facilitates the formation of a "vortex" mode in the atomic motion. The region involved in such motions has a characteristic size on the order of 50 Å. In this simulation, specific features of the model crystal account for the vortex shape being noticeably elongated in the [100] direction (Fig. 1a). Detailed analysis of the pattern of atomic displacements at the second stage showed that the vortexlike motion of atoms appears and disappears in a periodic manner. The lifetime of such correlated motions is on the order of several picoseconds, and the intervals between these periods are also on the order of 10^{-12} s. The magnitudes of atomic displacements in the course of vortexlike motion are in the elastic domain. This is evidenced by the absence of structural defects and the retained continuity of the material. The periodic formation of vortices can be interpreted as a means of providing dynamic relaxation of stresses in a complex medium in the elastic domain. This factor also accounts for a periodic character of processes in the second stage.

When the resource of elastic behavior is exhausted, the process enters the third stage characterized by the by the loss of correlation of the vortexlike motion of atoms in the regions between micropores. A thorough analysis of the crystal structure at the moments of time corresponding to various stages of deformation showed that the onset of the third stage coincides with the formation of the deformation localization bands (Fig. 1b). It should be noted that these bands are nucleated on the free surfaces of micropores. The moment of nucleation of the deformation localization bands is preceded by the loss of correlation of the motion of atoms on the inner surfaces of micropores (i.e., loss of stability), which is shown in Fig. 1c and is analogous to the events on the outer surface pointed out in [6]. Thus, the third stage involves rearrangement of the atomic structure in the region between micropores.

Acknowledgments. This study was supported in part by the Presidential Program of Support for Leading Scientific Schools in Russia (project no. NSh-2324.2003.1), the Ministry of Education of the Russian Federation (project no. PD02-1.5-425), the Russian Science Support Foundation, and the US Civilian Research and Development Foundation for the Independent States of the Former Soviet Union (CRDF grant no. TO-016-02).

REFERENCES

1. V. A. Likhachev, A. E. Volkov, and V. E. Shudegov, *The Continuum Theory of Defects* (Leningrad State University, Leningrad, 1986) [in Russian].
2. S. G. Psakhie, S. Yu. Korostelev, S. I. Negreskul, *et al.*, Phys. Status Solidi B **176**, K41 (1993).
3. S. G. Psakhie and K. P. Zol'nikov, Pis'ma Zh. Tekh. Fiz. **23** (14), 43 (1997) [Tech. Phys. Lett. **23**, 555 (1997)].
4. L. D. Landau and E. M. Lifshitz, *Course of Theoretical Physics*, Vol. 3: *Quantum Mechanics: Non-Relativistic Theory* (Nauka, Moscow, 1989; Pergamon, Oxford, New York, 1977).
5. M. S. Daw and M. I. Baskes, Phys. Rev. B **29**, 6443 (1984).
6. *Physical Mesomechanics and Computer Designing of Materials*, Ed. by V. E. Panin (Nauka, Novosibirsk, 1995) [in Russian].

Translated by P. Pozdeev

Technical Physics Letters, Vol. 31, No. 1, 2005, pp. 86–88. Translated from Pis'ma v Zhurnal Tekhnicheskoĭ Fiziki, Vol. 31, No. 2, 2005, pp. 89–94.

Thin-Film Photosensitive Structures Based on a Homoconjugated Organosilicon Polymer–Copper Phthalocyanine Heterojunction

S. E. Nikitin, Yu. A. Nikolaev, V. Yu. Rud', Yu. V. Rud',
E. I. Terukov, and V. V. Shamanin

Ioffe Physicotechnical Institute, Russian Academy of Sciences, St. Petersburg, 194021 Russia
St. Petersburg State Technical University, St. Petersburg, 195251 Russia
Institute of Macromolecular Compounds, Russian Academy of Sciences, St. Petersburg, 199004 Russia
e-mail: yuryrud@mail.ioffe.ru
Received August 24, 2004

Abstract—Rectifying photosensitive structures of the ITO/P(Si)/CuPc type have been synthesized based on a heterojunction between a homoconjugated organosilicon polymer P(Si) and copper phthalocyanine CuPc. The maximum voltage responsivity of the samples (~1 V/W at T = 300 K) was observed when the structure was illuminated from the P(Si) side. In this illumination mode, thin-film photovoltaic converters based on the proposed heterojunction exhibit a fine structure in the photosensitivity spectrum. It is suggested that the new structures can be used as selective photosensors. © *2005 Pleiades Publishing, Inc.*

Investigations of the photovoltaic effect in heterojunctions between diamondlike crystalline semiconductors and organic compounds of both natural and synthetic origin led to the development of new trends in molecular photoelectronics [1–3]. Recently [4, 5], we demonstrated the possibility of creating photosensitive structures based on the direct contacts of homoconjugated organoelemental polymers (P) or metal phthalocyanines (MePc) with crystalline silicon.

This Letter presents the results of investigation of the photovoltaic properties of the first heterojunctions between a homoconjugated organosilicon polymer P(Si) and copper phthalocyanine CuPc.

Synthesis. The samples of new photosensitive structures were prepared by depositing organic layers of P(Si) and CuPc onto glass substrates (20 × 20 × 0.3 mm) preliminarily coated with a thin (d = 0.3 μm) transparent conducting film of indium tin oxide (ITO). Thin films of P(Si) with a thickness of ~0.05 mm were obtained under normal conditions by casting a polymer solution onto the ITO surface [4] and then homogeneously colored light-yellow by exposure to integral light of an incandescent lamp. The P(Si) film had a mirror smooth surface and exhibited sufficiently good adhesion to the ITO underlayer. After termination of the drying process, a layer of CuPc with a thickness of d ~ 1 μm was deposited onto the P(Si) film surface by sublimation in vacuum (~10^{-4} Torr) at a temperature of about 50°C. This film had a mirror smooth surface and exhibited homogeneous dark-blue color. The regime of sublimation was selected so as ensure a sufficiently high, stable adhesion of CuPc to the surface of the P(Si) layer.

Thus, using the above technology, we have synthesized the first structures of the type glass/ITO/P(Si)/CuPc/Al, which could be illuminated both from the side of P(Si) layer and from the side of the CuPc film. The area of P(Si)/CuPc heterojunctions was about 1 cm^2. The ohmic contact on the P(Si) side was provided by the ITO film, and on the CuPc side, by a vacuum-deposited Al film with a thickness of ~0.1 μm.

Experimental results and discussion. The results of measurements of the stationary current–voltage (I–U) characteristics of thin-film ITO/P(Si)/CuPc/Al structures showed that the samples exhibit characteristic rectification properties. The forward current direction in all cases corresponded to the negative polarity of applied bias voltage on the ITO electrode. Figure 1 shows the typical I–V curve for one of the synthesized structures. The rectification coefficient K estimated as a ratio of the forward and reverse currents at a fixed bias voltage in the range studied was rather low (K = 2–2.5). The residual resistance of sample structures was on the order of $R \sim 10^{11}$ Ω (T = 300 K). These results are indicative of the need for solving a problem of dehydration of thin organic films and optimization both of the film synthesis technology and of the thin-film structure design.

Illumination of the synthesized thin-film structure both from the CuPc side and from the P(Si) side gave rise to a photoresponse more pronounced in the case when the light was incident via the ITO layer. The sign of the photoresponse was independent of the site of illu-

1063-7850/05/3101-0086$26.00 © 2005 Pleiades Publishing, Inc.

mination, the photon energy, and the intensity of light: the response voltage always had a positive polarity on the CuPc side. The maximum voltage responsivity (~1 V/W at $T = 300$ K) was observed when the structure was illuminated from the P(Si) side.

Figure 2 shows the typical spectral dependences $\eta(\hbar\omega)$ of the relative quantum efficiency of photoconversion for one of the ITO/P(Si)/CuPc/Al structures measured in the two possible modes of illumination. The fact that the sign of the photovoltaic effect was independent of the photon energy and the illumination mode (Fig. 2, curves *1* and *2*) suggests that the photogenerated charge carriers are separated by the electric field only at the heterojunction between P(Si) and CuPc.

The $\eta(\hbar\omega)$ curves reveal a clearly pronounced dependence of the photosensitivity on the mode of illumination of the structure. In the case of illumination from the P(Si) side, the $\eta(\hbar\omega)$ spectrum exhibits a fine structure with seven maxima in the range from 1 to 3 eV (Fig. 2, curve *1*). On illumination from the opposite side (CuPc), the maximum photosensitivity decreases, the fine structure disappears, and the $\eta(\hbar\omega)$ spectrum acquires the shape of a single band with a maximum near $\hbar\omega = 2.1$ eV and a much lower width at half height ($\delta = 0.6$ eV). As can be seen, the energy position of the long-wavelength edge of photosensitivity of the synthesized structures ($\hbar\omega > 1.3$ eV) is almost independent of the illumination mode. This result suggests that the process of photoinduced absorption in the spectral interval $\hbar\omega \leq 1.8$ eV has a volume character.

The fact that the fine structure in the $\eta(\hbar\omega)$ spectra at $\hbar\omega_1 = 1.63$ eV and $\hbar\omega_2 = 1.85$ eV is observed only in the case of illumination from the P(Si) side (Fig. 2, curves *1* and *2*) indicates that this fine structure is related to features of the energy spectrum of P(Si). The presence of maximum photosensitivity at $\hbar\omega = 2.1$ eV on exposure of the CuPc side allows this maximum to be attributed to the photoinduced absorption in the CuPc film. Then, a decrease in photosensitivity of the structure at the photon energies $\hbar\omega > 2.1$ can be related to increasing absorption in the CuPc layer, which accounts for the observed drop in η (Fig. 2, curve *2*). Exposure of the P(Si) side leads to an increase in photosensitivity in the short-wavelength range, whereby the η value reaches the absolute maximum at $\hbar\omega^m = 2.34$ eV. This behavior suggests that the short-wavelength photosensitivity at $\hbar\omega \cong 2.1$ eV observed on illumination from the P(Si) side is related to features of the electron spectrum of this polymer. Thus, there are grounds to believe that the film of the homoconjugated polymer in the ITO/P(Si)/CuPc structures studied plays the role of a wide-bandgap component. The long-wavelength maxima observed in the photosensitivity spectrum at 1.13 and 1.33 eV and resolved only upon illumination from the P(Si) side (Fig. 2, curve *1*) are probably related to the photoinduced absorption in this polymer film.

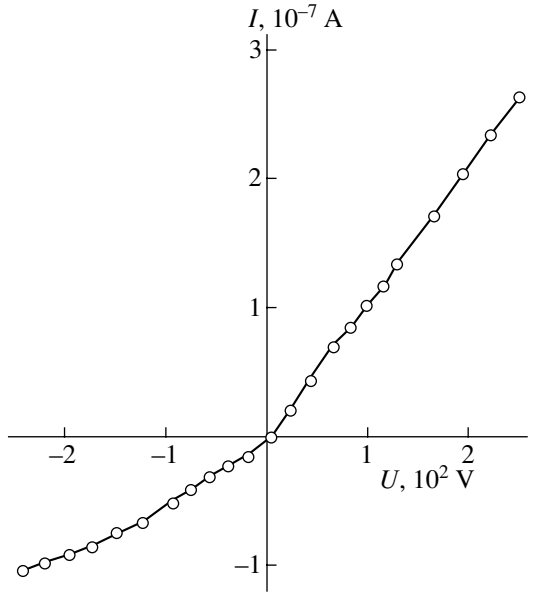

Fig. 1. Typical stationary current–voltage characteristic of an ITO/P(Si)/CuPc structure at $T = 300$ K. Forward direction corresponds to a bias voltage applied with plus on the ITO film electrode.

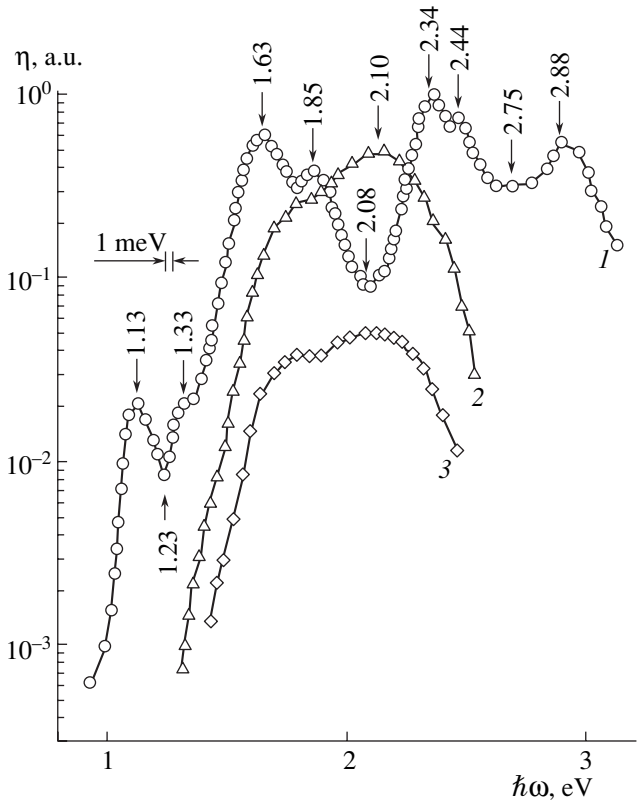

Fig. 2. The typical spectral dependences of the relative quantum efficiency of photoconversion at $T = 300$ K in the (*1*, *2*) ITO/P(Si)/CuPc and (*3*) ZnO/CuPc/Si structures. The samples were illuminated (*1*) from the P(Si) side, (*2*) from the CuPc side, and (*3*) via ZnO. Arrows indicate the energy positions of spectral features. Spectra *1* and *2* are normalized to the absolute maximum (curve *1*, $\hbar\omega_1 = 2.34$ eV); spectrum *3* is shifted along the ordinate axis for the convenience of comparison.

It should be emphasized that the photosensitivity spectrum of the thin-film ITO/P(Si)/CuPc structure illuminated from the side of the narrow-bandgap component (CuPc) (Fig. 2, curve *2*) has proved to be much like that observed previously for a ZnO/CoPc/Si structure illuminated from the ZnO side (Fig. 2, curve *3*). This similarity confirms the above assumption that photosensitivity of the ITO/P(Si)/CuPc structure illuminated from the CuPc side is determined predominantly by the photoinduced absorption in the CuPc film.

In conclusion, the main feature of the photosensitivity spectrum of a thin-film structure based on the heterojunction between two organic semiconductors (in this case, P(Si) and CuPc) is the presence of several peaks in $\eta(\hbar\omega)$, which agrees with the notions on the discrete character of the absorption spectra of these compounds [6, 7]. This suggests that organic semiconductors can be used for the creation of selective photosensors insensitive to background radiation.

REFERENCES

1. V. Yu. Rud', Yu. V. Rud', and V. Kh. Shpunt, Fiz. Tekh. Poluprovodn. (St. Petersburg) **29**, 1178 (1995) [Semiconductors **29**, 608 (1995)].
2. R. Rinaldi, E. Brauca, R. Cingolani, *et al.*, Appl. Phys. Lett. **78**, 3541 (2001).
3. P. Penmans, S. Ushida, and S. R. Forrest, Nature **425**, 158 (2003).
4. N. V. Blinova, E. L. Krasnopeeva, Yu. A. Nikolaev, *et al.*, Fiz. Tekh. Poluprovodn. (St. Petersburg) **37**, 53 (2003) [Semiconductors **37**, 53 (2003)].
5. G. A. Il'chuk, N. V. Klimova, O. I. Kon'kov, *et al.*, Fiz. Tekh. Poluprovodn. (St. Petersburg) **38**, 1056 (2004) [Semiconductors **38**, 1018 (2004)].
6. E. K. Putseiko, Dokl. Akad. Nauk SSSR **39**, 471 (1948).
7. J. Simon and J.-J. Andre, *Molecular Semiconductors: Photoelectrical Properties and Solar Cells* (Springer-Verlag, Berlin, 1985; Mir, Moscow, 1988).

Translated by P. Pozdeev

Technical Physics Letters, Vol. 31, No. 1, 2005, pp. 9–12. Translated from Pis'ma v Zhurnal Tekhnicheskoĭ Fiziki, Vol. 31, No. 1, 2005, pp. 17–23.

Numerical Solution of the Problem of Gas Efflux from a Closed Volume into Atmosphere

N. I. Sidnyaev

Moscow State Technical University, Moscow, 107005 Russia

e-mail: Sidn_ni@mail.ru

Received May 25, 2004

Abstract—The problem of modeling failures in systems of gas transportation, which are accompanied by the efflux of large volumes of natural gas from a broken pipeline into the atmosphere, has been considered. Using numerical methods, the maximum size of a dangerous zone is determined in order to evaluate the scale of catastrophes involving vertical gas outburst (perpendicular to the wind direction). © *2005 Pleiades Publishing, Inc.*

Exhaustive mathematical description of a turbulent flow resulting from the interaction between a gas flowing out of a pipeline and the atmospheric air requires a consideration of the complete system of Navier–Stokes equations for a viscous compressible gas in the gravitational field [1, 2]:

$$\begin{aligned}
&\frac{\partial \rho}{\partial t} + \frac{\partial(\rho u)}{\partial x} + \frac{\partial(\rho w)}{\partial z} = 0,\\
&\frac{\partial(\rho u)}{\partial t} + \frac{\partial(\rho u)^2}{\partial x} + \frac{\partial(\rho u w)}{\partial z} + \frac{\partial p}{\partial x} = \frac{\partial}{\partial z}\left(\rho K_z \frac{\partial u}{\partial z}\right),\\
&\frac{\partial(\rho w)}{\partial t} + \frac{\partial(\rho u w)}{\partial x} + \frac{\partial(\rho w)^2}{\partial z} + \frac{\partial p}{\partial z}\\
&\quad = \frac{\partial}{\partial z}\left(\rho K_z \frac{\partial w}{\partial z}\right) - \rho g,\\
&\frac{\partial(\rho H)}{\partial t} + \frac{\partial(\rho u H)}{\partial x} + \frac{\partial(\rho w H)}{\partial z}\\
&\quad + \frac{\partial p u}{\partial x} + \frac{\partial p w}{\partial z} = \frac{\partial}{\partial z}\left(\rho K_z \frac{\partial H}{\partial z}\right),
\end{aligned} \tag{1}$$

where ρ is the density of the gas mixture; u and w are the horizontal and vertical components of the velocity vector, respectively; H is the enthalpy; p is the pressure; K_z is the turbulent transfer coefficient [3, 4]; and g is the gravitational acceleration.

Let us consider a solution of Eqs. (1) in a boundary region of the atmosphere. The initial conditions (H_a, ρ_a, U_a) characterize the state of the atmosphere at the moment of the outburst [4]. In the vicinity of the source (Fig. 1a), the boundary and initial conditions on the boundary AD can be written as follows:

$$\begin{aligned}
&\rho(x, 0, t) = f_1(t), \quad u(x, 0, t) = f_2(t),\\
&w(x, 0, t) = f_3(t), \quad H(x, 0, t) = f_4(t).
\end{aligned} \tag{2}$$

The system of equations (1) is closed by the equation of state of the ideal gas,

$$p = \frac{\rho}{M} RT, \tag{3}$$

where M is the molar mass, R is the universal gas constant, and T is the absolute temperature.

The mathematical model has been numerically simulated using a modified PIC code [5]. Let us separately

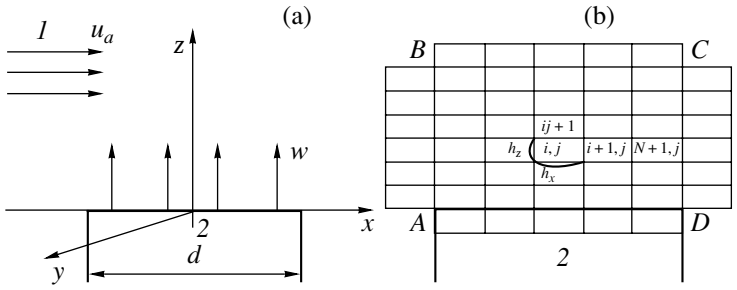

Fig. 1. Modeling gas efflux from a broken pipeline: (a) schematic diagram; (b) computational grid; (*1*) wind; (*2*) source.

1063-7850/05/3101-0009$26.00 © 2005 Pleiades Publishing, Inc.

consider all stages of the calculation procedure. The domain of integration is covered with a rectangular (Euler) computational grid with the cell mesh sizes h_x and h_z in the planar Cartesian coordinate system (Fig. 1b). The integers i (for the x axis) and j (for the z axis) indicate the cell center. In the first stage, we vary only the quantities referring to the entire cell and assume the gas to be retarded. For this reason, we reject convective terms of the div($\varphi\rho V$) type, where $\varphi = (1, u, w, H)$, describing the transfer effects in Eqs. (1).

According to the continuity equation, the density field is retarded and, hence, we can take ρ out of the sign of differentiation with respect to time and resolve Eq. (1) relative to the time derivatives of u, w, and H. After certain transformations, the Euler-stage differential equations can be written as

$$\frac{\partial \rho}{\partial t} = 0,$$

$$\begin{aligned} \rho\frac{\partial u}{\partial t} &= -\frac{\partial p}{\partial x} + \frac{\partial}{\partial z}\left(\rho K_z \frac{\partial u}{\partial z}\right), \\ \rho\frac{\partial w}{\partial t} &= -\frac{\partial p}{\partial z} + \frac{\partial}{\partial z}\left(\rho K_z \frac{\partial w}{\partial z}\right) - \rho g, \\ \rho\frac{\partial H}{\partial t} &= -\frac{\partial pu}{\partial x} - \frac{\partial pw}{\partial z} + \frac{\partial}{\partial z}\left(\rho K_z \frac{\partial H}{\partial z}\right). \end{aligned} \tag{4}$$

In the Lagrange stage, we include the transfer effects (taking into account the exchange between cells rearranged on the old Euler grid) and calculate the mass fluxes ΔM^n across boundaries of the grid over the time τ. It is assumed that the entire mass is transferred by the velocity component normal to the boundary. For example, the continuity equation in the differential form can be written as

$$\begin{aligned} \rho_{i,j}^{n+1} h_x h_z &= \rho_{i,j}^n h_x h_z - \Delta M_{i+1/2,j}^n \\ &+ \Delta M_{i-1/2,j}^n - \Delta M_{i,j+1/2}^n + \Delta M_{i,j-1/2}^n, \end{aligned}$$

where the mass flux is expressed as

$$\Delta M_{i+1/2,j}^n = \rho_{i+1/2,j}^n \tilde{u}_{i+1/2,j}^n h_z \tau.$$

In the final stage, we consider the spatial redistribution of the mass, momentum, and energy, and determine the final fields of the Euler flux parameters on the fixed grid at the time $t^{n+1} = t^n + \tau$. In this stage, the equations represent the laws of conservation for the mass, momentum, and total energy written in the differential form for a given cell:

$$\begin{aligned} M^{n+1} &= M^n + \sum \Delta M^n, \\ P^{n+1} &= P^n + \sum \Delta P^n, \quad H^{n+1} = H^n + \sum \Delta H^n. \end{aligned} \tag{5}$$

Here, ΔM^n is the mass of the gas transferred during the time τ across one of the cell boundaries, and the sum is taken for all sides of the cell. The terms ΔP^n and ΔH^n have an analogous meaning. Equations (5) imply, in particular, that there are no sources and sinks for M, P, and H inside the flow field and their variation during the time τ is related only to interactions at the outer boundary of the flow region. It is assumed that the mass fluxes ΔM^n across the cell boundaries (determined in the second stage) have intermediate velocities and specific energies (calculated in the first stage). The ΔM^n values play the role of weight functions.

The very character of the construction of the above scheme implies that each computational cycle involves a complete set of calculations for the given time interval, in which all the initial and boundary conditions are satisfied and a real pattern of gas flow at the corresponding moment of time is determined. The numerical solution of the formulated problem of interaction between the gas outburst and the wind is continued until reaching a section in which the axial region of the gas flow will be comparable with the air flow velocity (to within a preset accuracy) and the time variation of the gasdynamic parameters in this section will decrease to a predetermined level.

Below, we will consider a particular example of the gas outburst from a broken pipeline (acting as the source). The initial conditions correspond to the atmospheric conditions at the moment of the gas outburst. Conditions at the AD boundary correspond to the oncoming gas flow. At the open boundaries AB, BC, and CD, the flow parameters are extrapolated beyond the region under consideration.

The transition from subsonic velocities inside the pipeline to a critical gas efflux in the broken pipeline section proceeds over a distance ranging from one to several dozens of characteristic lengths. Determination of the turbulent transfer coefficients for the flow under consideration is an independent problem, which can be solved using the relationship between the turbulent viscosity in a jet and the kinetic turbulent energy E and its scale L (this concept was proposed by Kolmogorov [3] and Prandtl [6]): $K_z \sim E^{1/2}L$. In this study, we will use the relation [4]

$$K_z = \beta b Q\left(\left|\frac{U_R^2 - uU_a}{U_R}\right| + 4.5\left|\frac{wU_a}{U_R}\right|\right),$$

where β is an empirical coefficient dependent on the shape of the gas jet ($\beta \approx 2$ [7]), b is the jet radius,

$$Q = 0.08 + \left|\frac{0.5gwb\left(\frac{\rho_a}{\rho} - 1\right)}{U_R^3}\right|,$$

and U_R is the absolute value of velocity of the resulting flow.

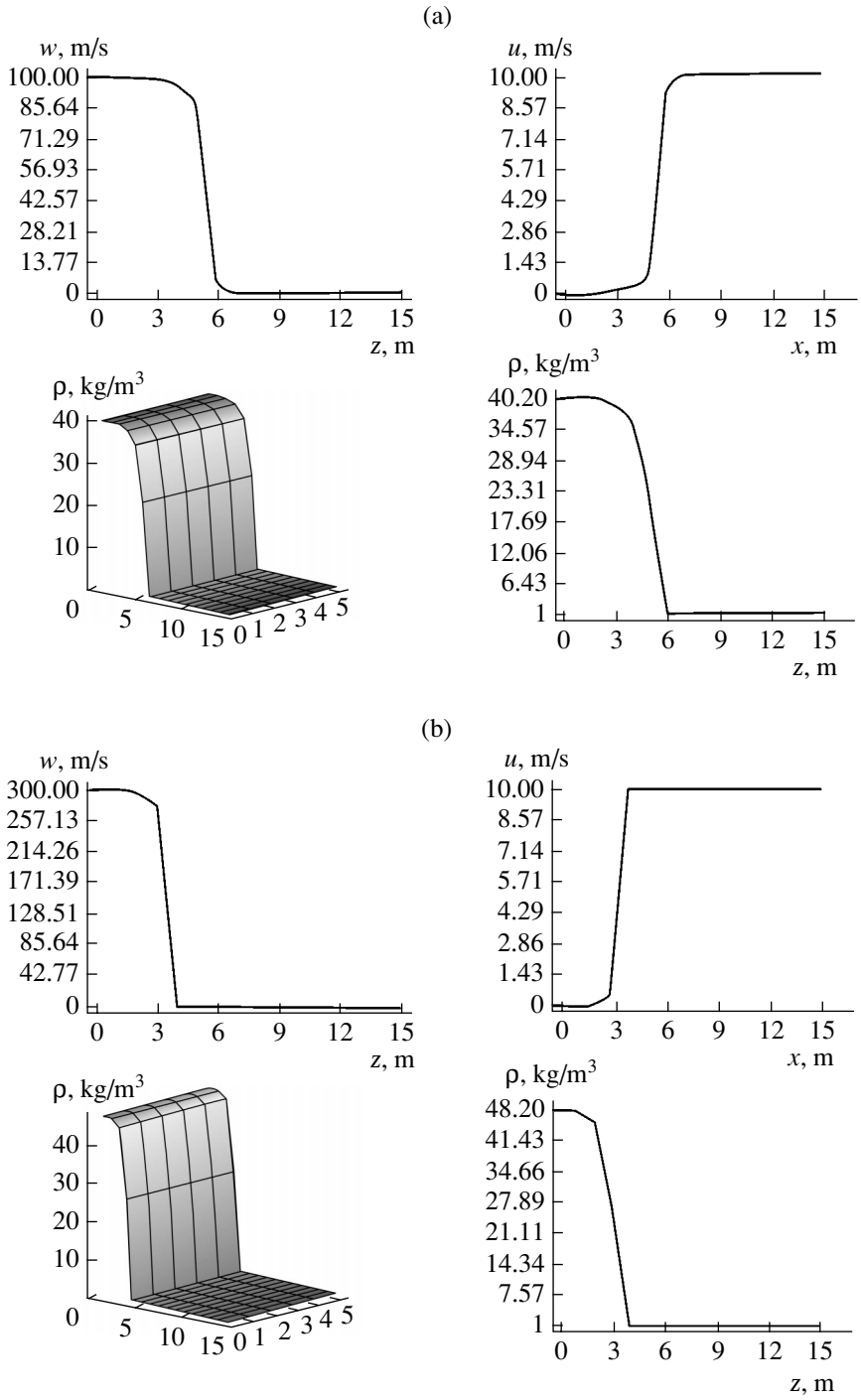

Fig. 2. Calculated profiles of the longitudinal (z axis) and transverse (x axis) gas velocity components and the corresponding gas density profiles at the time $t = 0.05$ (a) and 0.01 s (b). Calculations were performed for the constant values of gas pressure (P = 6078 kPa) and velocity (w = 300 m/s) in the broken pipeline section.

Numerical calculations were performed for a rectangular region with dimensions $AB = CD = 15$ m and $AD = BC = 0.5$ m. The atmospheric pressure was P_a = 101300 Pa and the wind velocity was $U_a = 10$ m/s. The pressure and velocity of the gas in the broken pipeline section were assumed to be constant: $P = 5065000$ Pa and $w = 100$ m/s. The molar mass of the gas (methane) is $M = 0.016$ kg/mol, the universal gas constant is R = 8.31 J/(mol K), and the temperature (assumed to remain unchanged) is $T = 273$ K.

Figure 2a shows the calculated profiles of the longitudinal (z axis) and transverse (x axis) gas velocity components and the corresponding density profiles at the time $t = 0.05$ s. Figure 2b presents the analogous

data for $t = 0.01$ s. As was noted above, the transition from subsonic velocities inside the pipeline to a critical gas efflux in the broken pipeline section proceeds over a distance ranging from one to several dozens of characteristic lengths. This value can be taken equal to the pipe diameter. The transition region is characterized by the complicated character of the turbulized gas flow with a substantially inhomogeneous cross-sectional profile.

It is very difficult to obtain a numerical solution of the problem in the entire region under consideration (including both the jet zone and the diffusion trace), since it is necessary (i) to use a small-scale mesh grid in the jet zone, which leads to the appearance of large spatial arrays of the flow parameters (the characteristic source size is ~1 m, while the regions under consideration can reach up to 10 km) and (ii) to consider small concentrations, which can be an order of magnitude below the accuracy of the obtained numerical solution. In order to illustrate the reliability of the proposed model, Fig. 2 shows the distribution of some parameters along the jet axis.

REFERENCES

1. L. I. Sedov, *A Course in Continuum Mechanics* (Nauka, Moscow, 1983; Wolters-Noordhoff, Groningen, 1971), Vols. 1, 2.
2. *Gasdynamics. Mechanics of Liquids and Gases: High-School Textbook*, Ed. by A. I. Leont'ev (MGTU im. Baumana, Moscow, 1997) [in Russian].
3. A. N. Kolmogorov, Dokl. Akad. Nauk SSSR **30** (4) (1941).
4. A. S. Edigarov and V. A. Suleĭmanov, Mat. Model. **7** (1995).
5. O. M. Belotserkovskiĭ and Yu. M. Davydov, *Particle-in-Cell Methods in Gasdynamics* (Nauka, Moscow, 1982) [in Russian].
6. L. Prandtl and K. Weighardt, *Uber ein Neues Formelsistem dur die Ausgebildete Turbulenz* (Nachr. Akad. Wiss., Math.-Phys. Kl., Göttingen, 1945).
7. *Prediction Methods for Turbulent Flows*, Ed. by W. Kollmann (Hemisphere, Washington, 1980).

Translated by P. Pozdeev